An Investigation into the Morphologies of Polystyrene-b-Polyisoprene Micelles

Isaac LaRue

A dissertation submitted to the faculty of the University of North Carolina at Chapel Hill in partial fulfillment of the requirements for the degree of Doctor of Philosophy in the Department of Chemistry.

Chapel Hill
2006

Approved by:

Advisor: Professor Sergei Sheiko

Reader: Professor Michael Rubinstein

Reader: Professor Jan Genzer

Professor: Valerie Sheares Ashby

Professor: Thomas Baer

ABSTRACT

ISAAC LARUE: An Investigation into the Morphologies of Polystyrene-b-Polyisoprene Micelles

(Under the direction of Sergei Sheiko)

Spherical, cylindrical and vesicle micelles were formed from polystyrene-block-polyisoprene copolymer in heptane. The micelle morphology, critical micelle concentration, aggregation number, hydrodynamic radius, core radius, shell thickness, core density, and cylindrical micelle length were studied by a combination of scattering techniques and atomic force microscopy. The experimental results were compared with recently developed theoretical models. The crew-cut asymptotic model was found to inaccurate for all measured parameters even in the range of small polyisoprene blocks where it should be most applicable. The start-like asymptotic model correctly captured most of the data in the range of large polyisoprene block size, i.e. when the micelles were the most star-like. The numerical solution was seen to accurately predict most of the physical properties in the full range of polyisoprene block size studied.

In addition it was found that reversible morphological transitions from cylindrical to spherical micelles as well as vesicle to cylindrical micelles can be induced solely through temperature changes. However, the reverse process, upon cooling, is much slower than the transition while heating.

TABLE OF CONTENTS

LIST OF TABLES

LIST OF FIGURES

LIST OF ABBREVIATIONS AND SYMBOLS

AFM	Atomic Force Microscopy
CMC	Critical Micelle Concentration
DLS	Dynamic Light Scattering
DSC	Differential Scanning Calorimetry
GPC	Gel Permeation Chromatography
LS	Light Scattering
PFPE	Perfluoropolyether
PI	Polyisoprene
PS	Polystyrene
SANS	Small Angle Neutron Scattering
SAXS	Small Angle X-ray Scattering
SLS	Static Light Scattering
a_A	Size of the soluble monomer
a_B	Size of the insoluble monomer
A	Notation for soluble block
B	Notation for insoluble block
C_F	Numerical coefficient
C_H	Numerical coefficient
F_{3star}	Free energy per chain of star-like spherical micelle
F_{Aj}	Free energy of the micellar corona with morphology j
F_{Bj}	Free energy of the micellar core with morphology j

F_j	Total free energy of micelle with morphology j
F_{sj}	Free energy of the micelle surface with morphology j
g_A	Number of A monomers inside a blob
H_3	Spherical corona thickness
H_{3star}	Corona thickness in star-like spherical micelle
j	Morphology index label (1=lamella, 2=cylinder, 3=sphere, 0=unimer)
K	Logarithmic term
k_j	Numerical coefficients: $k_1 = \pi^2/8$, $k_2 = \pi^2/16$, $k_3 = 3\pi^2/80$
kT	Thermal energy
l_A	Kuhn segment size of soluble block
l_B	Kuhn segment size of insoluble block
N_A	Degree of polymerization of the soluble block
N_B	Degree of polymerization of the insoluble block
p_A	Stiffness parameter of the insoluble block: $p_A = l_A / a_A$
p_B	Stiffness parameter of the insoluble block: $p_B = l_B / a_B$
Q	Aggregation number (total number of chains per micelle)
Q_{3star}	Aggregation number of star-like spherical micelle
r_j	Dimensionless core radius with morphology j: $r_j = R_j / a_B$
r_{3star0}	Dimensionless core radius if K is treated as a constant on the order of unity
R_{3star}	Core radius of star-like spherical micelle
R_3^{tot}	Total size of a spherical micelle

R_{B0}	Radius of the core for a single collapsed block B
R_G	Gaussian end-to-end distance: $R_G = \sqrt{a_B N_B l_B} = a_B \sqrt{p_B N_B}$
R_j	Radius of core with morphology j
s	Surface area per chain
γ	Surface free energy per area a_B^2 : $\gamma = \tilde{\gamma}\, a_B^2$
$\tilde{\gamma}$	Surface free energy per unit area (surface tension)
θ	Theta Temperature
v	Excluded volume parameter
ξ_A	Concentration blob size of block A
ξ_T	Thermal blob size: $\xi_T \cong p_A^2 v^{-1} a_A$
τ	Relative deviation from theta-temperature: $\tau = (T - \theta)/T$
ϕ	Volume fraction of B monomers in the micelle core

1. Introduction

Solution based aggregates such as micelles and vesicles are all around us; they are in soap to help remove grease and oil,[1] they solubilize fat particles in the milk[2] you pour over your breakfast cereal, and they form the cell membranes of all living creatures.[3] The vast majority of micelles that are encountered in daily life are made up of small molecular weight surfactants, which are composed of an aliphatic tail and a polar or charged head group. However more and more diblock micelles are finding use in everyday applications. Polymer micelles are used as templates, drug delivery systems, viscosity modifiers, and in oil field technologies. In all these applications, the dimensions of micellar particles are of paramount importance. Many applications are shape specific to a particular morphology, such as using cylindrical polymer micelles as nanowires[4] or as a possible alternative to electrospinning,[5,6] or vesicles as scavengers[7] and drug delivery systems.[8] For these applications, the ability of micelles to either maintain the equilibrium shape or switch shapes under given conditions are highly desirable. As such we have set out to investigate how the morphology of polymer micelles can be controlled.

1.1 Small Molecular Weight Surfactant Micelles

Before looking at the more complicated system of polymer micelles, it is good to start with the simpler case of micelles formed by small molecular weight surfactants (SMWS). When SMWS are dissolved in water the aliphatic tails do not want to be in contact with

the water, as such they reduce the system's free energy by undergoing association with other SMWS to form a micelle (**Figure 1**). Theoretical models for SMWS micelles are based on geometric packing of the amphiphiles and assume the free energy of the core forming tails is constant and independent on the core size. In the models, there is a competition between the head groups and the tail groups: The charged heads repel each other causing the amphiphiles to spread out from one another—leading to higher surface area per molecule (*s*). The tails, on the other hand, want the amphiphiles to be as close together as possible to reduce their contact with the surrounding solvent and thus minimize the interfacial energy—leading to a smaller *s*. The balance of these two forces leads to an equilibrium value of *s*.

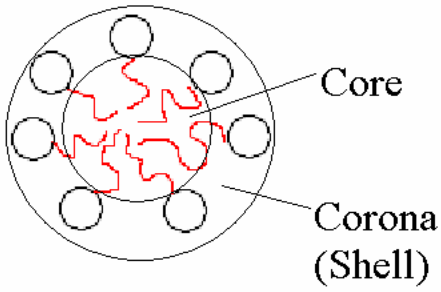

Figure 1. Small molecular weight surfactants associate together to form micelles. The aliphatic tails form the core of the micelle, while the charged head groups are in the corona.

If the size of the tail is fixed (i.e. the volume per molecule (*v*) is constant), the aggregation number (number of molecules in the micelle) can then be calculated from both as *S/s* (the total micelle surface area divided by the surface area per molecule) and as *V/v* (the total micelle volume divided by the volume of a single molecule). By setting *S/s*=*V/v* and substituting for *S* and *V*, for the case of spherical micelles $S = 4\pi R^2$ and $V = \frac{4}{3}\pi R^3$, the micelle radius *R* is found to be $R = \frac{3v}{s}$. If the same is done for cylinders and lamella, it is found that $R = \frac{jv}{s}$ where j=1, 2, and 3 respectively for lamella, cylindrical and spherical micelles. In such a way the ideal value of R can be found for each morphology if *s* and *v* are known.

If s is small, R will become large, i.e. the tails within the core should stretch to adopt the larger radius. Since the tails of the micelles have a finite length, they not able to stretch beyond a critical length l_c, therefore R cannot be larger than l_c. The SMWS head groups always prefer a spherical geometry meaning that if the contour length of the tail is longer than R_{sp} (l_c>R), than the micelles will adopt a spherical geometry. However, values of l_c<R would lead to an empty space inside the micelles, i.e. additional surface energy. In order to avoid this, micelles have the ability to change their shape. If micelles switch from spheres to cylinders, the radius reduces from R_{sh}=3v/s to R_{cyl}=2v/s. The smaller radius can accommodate shorter tails without making a hole inside the core. This means that the ratio of v to s along with l_c determines the ideal morphology of the micelles. When $\frac{v}{s l_c} < \frac{1}{3}$ spherical micelles will form, when $\frac{1}{3} < \frac{v}{s l_c} < \frac{1}{2}$ cylindrical micelles will form, and when $\frac{1}{2} < \frac{v}{s l_c} < 1$ lamella will form.

Even though the spherical morphology is preferred by the corona, those SWMS with tails that occupy a larger volume and/or smaller head groups must adopt cylindrical and lamella structures, while those with smaller tails and/or larger head groups will take on spherical structures. Spherical micelles formed from SMWS have been heavily studied as shown in the review article by Chevalier and Zemb.[9] Theoretical and experimental results for cylindrical micelles formed from SMWS

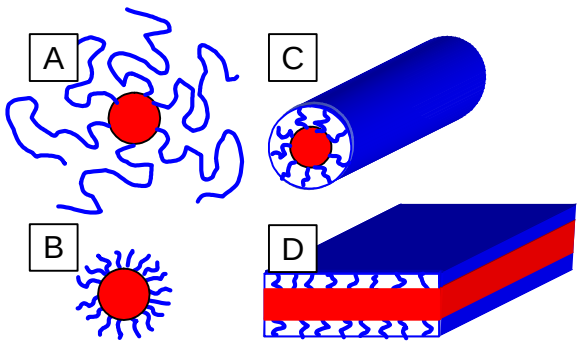

Figure 2. Different morphologies of diblock copolymer micelles: spherical star-like (A) and crew-cut (B) micelles, cylindrical micelles (C), and bilayer vesicles (D).

have been reviewed by Cates and Candau.[10] Vesicle micelles have also received much attention and have been reviewed by Texter.[11]

1.2 Block-copolymer Micelles

In a similar way to SWMS, when diblock copolymers are dissolved in a selective solvent (good solvent for one block and poor solvent for the other) above a certain concentration, called the critical micelle concentration (CMC), the diblocks will associate to form micelles with a core of the insoluble block and a corona of the soluble block.[12-16] As depicted in **Figure 2**, polymer micelles have been observed to exist in a vast array of sizes and shapes: everything from small spheres(A&B)[12,17-20] to long cylinders(C)[21,22] and giant polymer vesicles(D).[8,23,24] While the morphologies observed for polymer and SMWS micelles are similar, the competition of forces is more complicated when diblock polymers are used instead of SMWS. For SMWS, it is assumed that the tails can stretch to almost their fully extended length with little or no entropic penalty. When polymers are used instead, there is a significant entropic penalty for stretching the longer core block. This causes additional competition as to what the ideal micelle size and shape is, and thus the free energy of the tails can no longer be assumed as constant. There is also an entropic penalty due to extension of the corona block (that results in an uneven distribution of monomeric units along the radius of spherical and cylindrical micelles). In addition, the volume *v* of the core block depends on the solvent fraction within the core. This means that unlike SMWS micelles where simple geometric constraints can be used to determine the ideal morphology of the micelles, a more complex analysis is needed for polymer micelles.

As a first level approximation, one can still gain some insight into polymer micelles by looking at the packing constraints of SMWS micelles. Just like in SMWS micelles, the balance of the surface energy and the repulsion of the corona blocks determine an equilibrium area per molecule. However for polymer micelles, it is not just a simple matter of looking at the ratio of volume and surface are, it now becomes necessary to also look at how stretched the blocks are. Just like the SMWS head groups, corona blocks always prefer a spherical morphology. If the surface area per molecule is kept constant, the higher surface curvature of the spherical micelles provide more space (lower entropic penalty due to stretching) for the corona blocks, but result in less space (higher extension leading to a higher entropic penalty) for the core blocks. This means that morphological changes are expected if the entropic gain for the core blocks upon this transition is more than the corresponding entropic loss for the corona blocks.

Theory predicts that as the length of the shell (corona) block is reduced that the shape goes from spherical micelles to cylindrical micelles and eventually to bilayers as pictured in **Figure 2**. Further morphologies can be obtained through the addition of a third block,[25,26] changing architecture,[27] or both.[28] As discussed in the introduction, all morphologies can be used for certain applications. Furthermore, since there is several orders of magnitude difference in the viscosity of spherical and cylindrical micelle solutions of the same concentration, if the transition between morphologies is understood, controlled and reversible changes in solution viscosity might be obtained by changing the size, shape, and flexibility of the micelles. In addition, micelles also play an important role in several biological processes;[3,29] as such, a better understanding of micelles could lead to new insights and applications in life sciences.

1.3 Background

While much work has been done on polymer micelles, the vast majority of this work on micelle morphologies has been accomplished by trial and error through the synthesis of a large variety of new diblocks and by using mixtures of co-solvents. The systematic work that has been done for polymer micelles was directed at specific issues such as the critical micelle concentration (CMC) and aggregation number (Q) leaving many of the questions still unanswered, such as phase diagram, core density, and morphology control. In recent years, much of the work has been done on specific systems (new diblocks) targeted for specific application resulting in diblocks that are charged,[30,31] crystallizable,[32] that can form hydrogen bonds with the solvent,[21] or in cross-linked systems.[33-35] These additional stabilizing forces result in more complicated systems. While these systems hold great potential for the applications they were developed for, the transfer of these results for other systems is not readily obvious. While the random synthesis of new block-copolymers followed by the addition of mixed solvents has lead to a vast array of micelle morphologies, it provides no guidance on how to control the morphology for other micellar systems.

1.3.1 Morphological Map

When designing a new diblock for micelle applications, it is important to know what morphology one should expect the micelles to adopt. While much work has been done in this area for melts and blends of diblocks and homopolymers,[13] only a limited amount of work has been done for dilute solutions. Bates has constructed a phase diagram for the poly(1,2-butadiene-b-ethlene oxide) in water system for two different degrees of

polymerization of PB and several different PEO molecular weights.[36] While this study provides important insight, it is complicated by the fact that PEO can hydrogen bond with water. Hydrogen bonding can act to stabilize the micelles in such a fashion as is not possible in other systems. It also complicates the question as to whether the micelles are equilibrium structures.

1.3.2 Core Density

Tuzar *et al*. compared theoretical R_g based on models with swollen and non swollen cores of several Polystyrene-Poly(methacrylic acid) block copolymer micelles with the experimentally measured R_g for the same samples. They found that for some samples the non swollen core model was closer to the experimental value and for other samples the swollen core model was closer.[37] This possibly indicates that the density of the core was changing between samples; however without direct measurements of the core size no concrete conclusion could be drawn. In addition the use of charged diblocks further complicates the system.

1.3.3 Morphology Control

Eisenberg *et al.* showed that the morphology could be controlled for micelles formed from polystyrene-b-poly (acrylic acid) in DMF by adding water.[16] This study clearly shows that it is possible to control the morphology; however it is not known whether this control can be transferred to other systems that are not ionizable (neutral).

In addition to knowing what morphology the micelles will adopt, it is also important to know the size of micelles along with the critical micelle concentration (CMC) and

critical micelle temperature (CMT) at which one can expect micelles to form. Price *et al.* showed that changing the molecular weights of the each block had an effect on the standard states and hence on the CMT and CMC.[38,39] Eisenberg *et al*. have also looked at the effect the block length has on the CMC for block polyelectrolyte systems.[40] In addition they also looked at the effect of added salt to the CMC and radius of the micelles.[41,42] Tuzar *et al*. have shown the effect of MW and block ratio has on the aggregation number and micelle size for Polystyrene-b-Poly(methacrylic acid) in dioxane/water mixtures.[37]

1.4 Experimental Challenges

While polymer micelles hold great potential, they are often difficult to study. This is caused by several factors, the first of which is that the synthesis of well-defined diblocks can be challenging. In order to obtain relevant and reproducible results it is crucial to have diblocks with a low polydispersity and also to make sure that there is no residual homopolymer or triblocks.

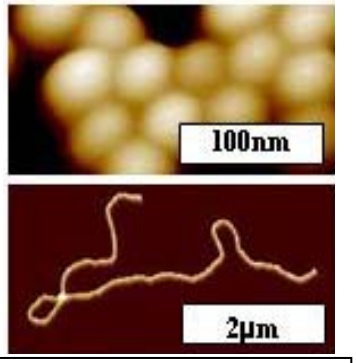

Figure 3. Top: dense layer of spherical micelles having a radius of 20nm. Bottom: cylindrical micelles several µm long.

A second factor is the size of the micelles, which varies from 10 nm spheres to cylinders and vesicles over 10µm (**Figure 3**). This large variation in sizes requires the use of multiple techniques to be able to fully study all micellar morphologies. A third issue that makes polymer micelles difficult to study is that they are dynamic systems which can change their molecular weight, size and shape in response to minute variations in the surrounding environment (temperature, solvent, additives, and

concentration) This dynamic nature of micelles means that they must be studied under carefully controlled conditions. Finally, block-copolymer micelles are nano-heterogeneous systems that consist of chemically different cores and shells.

1.5 Experimental Rationalization

To gain a fundamental understating of diblock polymer micelle morphologies, a systematic study has been preformed using one of the simplest block-copolymer systems, i.e. polystyrene-b-polyisoprene in heptane. This system is fully amorphous and neutral, though it retains all the characteristic features of micelle aggregation. By starting with the simplest case, a foundational understand can be achieved which can then be extended to more complex systems such as triblocks and systems with extra stabilizing forces. The combination of sound experimental studies with newly developed theory has lead to a profound understanding of what controls the morphology of polymer micelles. A combination of atomic force microscopy (AFM) and scattering techniques including static and dynamic light scattering (SLS, DLS), small angle neutron scattering (SANS), and small angle X-ray scattering (SAXS) was used. The combination of these techniques makes it possible to study the full range of polymer micelle sizes and morphologies both ex-situ and in real time.

In addition, it was shown that AFM and light scattering compliment each other nicely for studying polymer micelles. AFM allows for quick characterization of the size and shape of dry and quenched micelles, while light scattering can be used to confirm the morphologies while in solution, as well as following morphological changes in-situ.

2. Highlighted Accomplishments

The experimental research was conducted in close collaboration with theoretical predictions and polymer synthesis. Experimental findings were tested against theoretical predictions made by Zhulina and Rubinstein.[43] Experiment and theory guided the synthesis of new block-copolymers with a rigorously defined composition to match domains in the morphological map (Hadjichrstidis). The theoretical predictions of the phase diagram and dimensions of block-copolymer micelles are described in section 3. As will be described in more detail in sections 7.1.2 and 7.1.3.1 the experimental data was found to be in good agreement with the theoretical predictions for the aggregation number and hydrodynamic radius. Additionally, the experimental and theoretical location of the phase boundaries were found to be in good agreement for series 1 and 2 samples (40kDa PS) but theory was found to overestimate the stability ranges of lamella and cylindrical micelles for series 3 and 4 samples (20kDa PS) as will be further discussed in section 7.

Through these experimental studies, it was shown that AFM and light scattering compliment each other well for studying polymer micelles.[44] The largest accomplishment of this research was that for the first time reversible micellar morphological transitions induced solely by temperature changes were observed as will be shown in section 8.1.[45] The new found control of the micellar morphology opens a range of new applications through the use of dynamic morphologies.

3. Theory

In order for the experimental results to be useful for practical applications, it becomes necessary to use a theoretical model in order to apply the learned results to other systems or conditions. As such a theoretical model that describes the equilibrium behavior of amorphous, neutral diblocks in a selective solvent under dilute conditions (i.e. micelles do not overlap) has been developed through collaboration with E. Zhulina.[43] The model is described in the rest of section 3. The theory quantitatively describes the size of the micelles giving the aggregation number as wells the micelle radius. It also predicts the CMC as well as the location of the boundaries between different morphologies (spheres, cylinders, lamellae). In addition to exact (analytical) solution, which is more complicated to compute, the theory provides asymptotic solutions for star-like (when the corona radius is larger than the radius of the core) and crew-cut (when the corona radius is smaller than the radius of the core). The theoretical predictions were verified (tested) for PS-b-PI diblocks of different compositions in heptane (selective solvent for polyisoprene). In sections 7 and 8, the theoretical model is compared with experimental data.

3.1 Model

We consider flexible diblock copolymers that contain $N_A >> 1$ and $N_B >> 1$ monomers with respective sizes a_A and a_B. The selective solvent is assumed to be good or θ for block *A* and poor for block *B*. When the concentration of polymer in solution is above the so-called

critical micelle concentration (CMC), micelles of various morphologies form (see Figure 2). Blocks *B* associate to form the core of the micelle, whereas blocks *A* form the corona which ensures solubility of aggregates in solution. We consider the aggregates of three different morphologies labeled by index *j*: lamellar (*j* = 1), cylindrical (*j* = 2), and spherical (*j* = 3). We also consider unimers (i.e., isolated diblocks) identified by *j* = 0.

To examine the equilibrium structure and thermodynamic stability of micelles, we focus on their free energy, F_j. Below we separately consider three main components of this free energy

$$F_j = F_{Bj} + F_{sj} + F_{Aj} \qquad (1)$$

where F_{Bj}, F_{sj}, and F_{Aj} are the free energies per chain of the micellar core, of its surface, and of the corona.

3.2 Free Energy of the Core

As was pointed in the introduction, the micellar core plays an important role in changing morphologies and prefers the less curved morphologies of cylinders and lamellae, while the corona always wants to adopt a spherical morphology. In contrast to SMWS micelles, the free energy of the core of block-copolymer micelles strongly depends on the conformation of the insoluble block (i.e. the morphology is determined by more than just if the core block is longer than the ideal radius). In addition, the micellar core can be partially swollen by poor solvent. We assume that the volume fraction $\varphi = QN_B a_B^3/V_{core}$ of monomers *B* in the micellar core is solely controlled by monomer-solvent interactions and therefore independent of the shape of the micelle and distance *r* from its center. For a core with low polymer density,

$\varphi << 1$, the equilibrium volume fraction is determined by the balance of the attractive pair and repulsive ternary contacts between monomers, $\varphi \sim \tau$, where τ is the relative deviation from the θ-temperature, $\tau = (T - \theta)/T$, for polymer B. For larger values of the volume fraction φ, the higher-order monomer-monomer interactions are relevant. The free energy of the monomer-monomer interaction per block *B* is independent of the total number of chains in the micelle and coincides with the free energy F_{B0} in the collapsed core of a unimer (isolated diblock in solution). We can therefore omit it from further consideration because it does not contribute to the free energy difference between unimer and micelles of different morphology and aggregation number. If R_j is the radius of the core and *s* is surface area per chain, then the volume fraction of polymer in the core φ can be derived from the dense packing condition, i.e. the physical volume the chain occupies ($N_B a_B^3$) divided by the volume per chain inside the micelle which for spherical micelles can be calculated as $\frac{4\pi R^3}{3Q} = \frac{4\pi R^2 \cdot R}{3Q} = \frac{S \cdot R}{3Q} = \frac{s \cdot R}{3}$ this results in

$$\varphi = \frac{jN_B a_B^3}{sR_j} \qquad (2)$$

where *j* = 1, 2, and 3 corresponds to lamellar, cylindrical, and spherical core. From eq. 2 we find the radius of the core (in lamella, R_1 is half of core thickness)

$$R_j = \frac{jN_B a_B^3}{\varphi s} \qquad (3)$$

and the surface area per chain

$$s = \frac{jN_B a_B^3}{\varphi R_j} \qquad (4)$$

Here and below we denote generalized (unrestricted) values of the surface area per chain by a subscript *s* while the equilibrium surface area per chain in a micelle with morphology *j* is denoted with a subscript *sj*. For micelles with large aggregation number, blocks *B* are stretched in the core[46] with respect to their Gaussian end-to-end distance

$$R_G = \sqrt{a_B N_B l_B} = a_B \sqrt{p_B N_B} \qquad (5)$$

where $p_B = l_B/a_B$ is the ratio of the Kuhn segment l_B and monomer size a_B. The elastic free energy F_{Bj} of blocks *B* in the core of morphology *j* is described as

$$\frac{F_{Bj}}{kT} = k_j \frac{R_j^2}{R_G^2} = k_j \frac{R_j^2}{a_B^2 N_B p_B} = k_j j^2 \frac{a_B^4 N_B}{p_B s^2 \varphi^2} \qquad (6)$$

We approximate the elastic free energy of blocks *B* by eq 6 in the whole range of chain stretching $R_j/R_G \geq 1$ (ignoring nonlinear elongation). The numerical coefficients k_j were calculated by Semenov[47] and are given by

$$k_1 = \pi^2/8,\ k_2 = \pi^2/16,\ k_3 = 3\pi^2/80 \qquad (7)$$

Note that the values of k_j given by eq 7 were obtained for the specific case of a dense core (φ=1). They, however, remain valid for an arbitrary volume fraction φ of monomers *B* provided that the polymer density profile in the core is uniform. As discussed in the Introduction and derived below, the elastic contribution F_{Bj} remains small compared to the surface and corona free energies in stable micelles. However, it becomes important in

determining the transitions between different morphologies.

3.3 Surface Free Energy

Similar to SMWS, the surface free energy per chain F_{sj} for morphology j is associated with the interface between the core and the corona. This energy is proportional to the surface area per chain s (eq 4)

$$\frac{F_{sj}}{kT} = \tilde{\gamma}s = \gamma\left(s / a_B^2\right) = \gamma\frac{jN_B a_B}{\varphi R_j} \qquad (8)$$

where $\tilde{\gamma}$ is the surface free energy per unit area (surface tension) and $\gamma = \tilde{\gamma}a_B^2$ is the surface free energy per area a_B^2, both divided by kT. At low polymer volume fractions in the core (φ<<1) there is a scaling relation between the surface tension $\tilde{\gamma}$ and the volume fraction[48,49] φ ($\tilde{\gamma} \sim \varphi^2$). However, we focus below on relatively high values of the polymer volume fraction in the core, $\varphi \le 1$, which is relevant to most experiments. In this range of polymer concentrations the conventional scaling model[48,49] may not work, and in the following we use ψ as an additional independent parameter of the model.

The expression for the surface free energy per chain F_{sj} (eq 8) is valid for any morphology j. For example, for an isolated spherical globule (j = 0) of a single collapsed block B, the radius of the core is

$$R_{B0} = a_B\left(\frac{3N_B}{4\pi\varphi}\right)^{1/3} \qquad (9)$$

and the surface free energy of a unimer yields

$$\frac{F_{s0}}{kT} = 4\pi\tilde{\gamma}R_{B0}^2 = 4\pi\gamma\left(\frac{R_{B0}}{a_B}\right)^2 = 4\pi\gamma\left(\frac{3N_B}{4\pi\varphi}\right)^{2/3} = (36\pi)^{1/3}\gamma\left(\frac{N_B}{\varphi}\right)^{2/3} \qquad (10)$$

In section 3.7 we will use eq 10 to estimate γ from reported scattering data.[50]

3.4 Free Energy of the Corona

Because of the narrow interface between blocks *A* and *B*, the corona blocks *A* can be envisioned as tethered to the surface of the micellar core. In contrast to SMWS with charged head groups, the equilibrium structure of the corona is determined by the balance of the elastic stretching of blocks *A* and the repulsive interaction between monomers (two-body in a good solvent and three-body in a θ-solvent). We apply scaling analysis[48,49] to calculate the free energy of the corona chains, assuming that the free ends of the corona chains are localized at the outer boundary of the micelle. Within the framework of the scaling theory of polymer brushes, the corona of the micelle in a good solvent is envisioned as a melt of correlation blobs of size ξ_A (sections of chains interacting with each other with energy *kT*). A similar picture can be also applied to flexible chains in a θ-solvent. However, for stiffer chains in a θ-solvent with Kuhn segments larger than monomer size, correlation blobs overlap in the lateral direction. These correlation blobs have the same size in lamellar aggregates, while they increase in size from the core to the periphery in the corona for spherical and cylindrical micelles.[15,51-54]

The thermodynamic quality of the solvent for corona block *A* is governed by the magnitude of the monomeric excluded volume $vaA^3 > 0$. We assume that the values of the dimensionless excluded-volume parameter *v* and of the stiffness parameter

$$p_A = l_A/a_A > 1 \qquad (11)$$

are insufficient to ensure swelling of the blobs in the corona of micelle. If the size of the largest blob ξ_A is smaller than size of the thermal blob,[48,49] $\xi_t \cong p_A^2 v^{-1} a_A$ (*i.e.* $\xi_A < \xi_t$) a blob consisting of g_A monomers obeys the Gaussian statistics

$$\xi_A \cong a_A p_A^{1/2} g_A^{1/2} \qquad (12)$$

which is valid in coronas of all morphologies.[46] When the smallest blob size $\xi_A > \xi_t$, all the blobs in the corona are swollen, and the brush is found under good solvent conditions. We will model the corona of respective micelles as a planar (j = 1), cylindrical (j = 2), or spherical (j = 3) brush in a θ-solvent with blob size ξ_A given by eq 12.

3.5 Properties of Micelles

Equilibrium properties of micelles are obtained by minimization of the total free energy per chain F_j (eq 1) with respect to the core radius, including specific contributions defined in sections 3.2 and 3.3. Here we introduce the dimensionless radius of the core $r_j = R_j / a_B$ as an independent parameter. Minimization of micelle free energy per chain F_j with respect to the dimensionless core radius r_j is equivalent to minimization of free energy F_j with respect to the micelle aggregation number (that is, the number of chains in a spherical micelle, the number of chains per unit length in a cylindrical micelle or per unit area in a lamella).

3.5.1 Spherical Micelle

We focus on micelles in a θ-solvent. Taking into account eqs 1, 4, 6, and 8 we represent the free energy of a block copolymer chain in a spherical micelle as

$$\frac{F_3}{kT} = \frac{3\pi^2 r_3^2}{80 p_B N_B} + \gamma \frac{3N_B}{\varphi r_3} + \frac{1}{2\sqrt{3}} C_F p_A^{-3/4} \frac{r_3^{3/2}\varphi^{1/2}}{N_B^{1/2}} \ln\left[1 + \frac{2C_H p_A^{1/4} N_A \varphi^{1/2} a_A^2}{\sqrt{3} r_3^{1/2} N_B^{1/2} a_B^2}\right] \qquad (13)$$

Where C_F and C_H are numerical coefficients on the order of unity. By minimizing the free energy per chain F_3 with respect to the dimensionless radius of the core $r_3 = R_3 / a_B$ $(\delta F_3 / \delta r_3 = 0)$, we arrive at a nonlinear equation that determines the equilibrium value of r_3

$$\frac{3\pi^2 r_3}{40 p_B N_B} - \gamma \frac{3N_B}{\varphi r_3^2} + \frac{\sqrt{3}}{4} C_F p_A^{-3/4} \frac{r_3^{1/2}\varphi^{1/2}}{N_B^{1/2}} \ln\left[1 + \frac{2C_H p_A^{1/4} N_A \varphi^{1/2} a_A^2}{\sqrt{3} r_3^{1/2} N_B^{1/2} a_B^2}\right] - \\ - \frac{1}{6}\left(\frac{a_A}{a_B}\right)^2 \frac{C_F C_H N_A p_A^{-1/2} \varphi}{N_B\left[1 + \frac{2C_H p_A^{1/4} N_A \varphi^{1/2} a_A^2}{\sqrt{3} r_3^{1/2} N_B^{1/2} a_B^2}\right]} = 0 \qquad (14)$$

This nonlinear equation for dimensionless core radius r_3 can be solved numerically. By substituting the numerical solution r_3 of eq 14 into eq 13, we find the free energy F_3 per molecule in an equilibrium spherical micelle.

From the dimensionless core radius r_3 (solution of eq 14), one also finds the corona thickness

$$H_3 = R_3\left[\left(1 + \frac{2C_H p_A^{1/4} N_A \varphi^{1/2} a_A^2}{\sqrt{3} r_3^{1/2} N_B^{1/2} a_B^2}\right)^{1/2} - 1\right] \qquad (15)$$

and the total size of a spherical micelle

$$R_3^{tot} = R_3 + H_3 \qquad (16)$$

Aggregation number (total number of chains per micelle) Q is given by

$$Q = \frac{4\pi r_3^3 \varphi}{3N_B} \qquad (17)$$

Lines 3 in **Figures 4a & b** demonstrate the dimensionless core radius R_3/a_B and corona thickness H_3/a_A in a spherical micelle as a function of N_A (degree of polymerization of corona block) calculated from eqs 14 and 15. **Figures 4a & b** also includes the corresponding curves for cylindrical and lamellar aggregates. The set of model parameters used in **Figure 3** will be justified in section 3.7. The values used are specified in the figure legend and are the same for subsequent figures unless otherwise noted. The thick solid lines correspond to equilibrium regimes of different morphologies. The thin vertical lines at N_A^{sc} and N_A^{cl} are the locations of the sphere-to-cylinder and the cylinder-to-lamella transitions, respectively. The details of these transitions will be explained in section 3.6. **Figures 4a & b** also includes asymptotic lines that can be calculated analytically as demonstrated in subsequent sections.

3.5.1.1 Asymptotic Dependencies of Spherical Micelles

Equations 13-17 determine the equilibrium characteristics for spherical micelles at different values of N_A and N_B. However, these equations are rather complicated and can be solved only numerically. Therefore, frequently one uses asymptotic expressions obtained for either very long or very short corona blocks. In this section, we summarize the asymptotic

expressions for aggregation number and size of star-like ($H_3 << R_3$) and crew-cut ($H_3 >> R_3$) micelles by delineating the leading terms in the free energy per chain F_3.

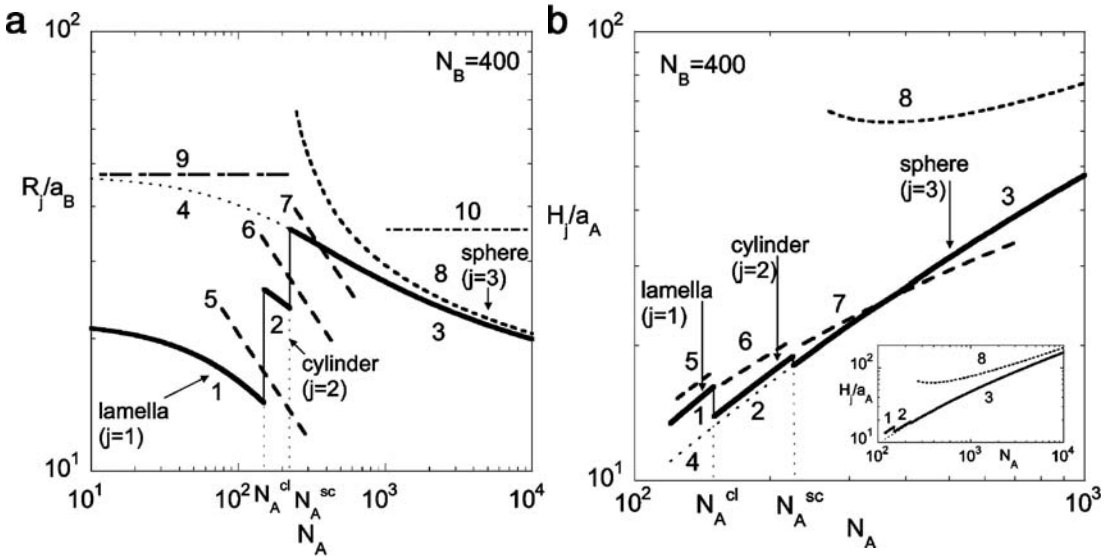

Figure 4. (a) Plot of the dimensionless radius of the micelle core Rj/a_B as a function of the degree of polymerization of the soluble block N_A. The plot shows both exact solutions and asymptotic values. Thick solid curves are exact solutions (eq 3) for lamella (1), cylinders (2), and spheres (3). The thin solid lines denote the transition from one morphology to another. The dotted line (4) denotes the size spherical micelles would adopt if they did not change morphology. The dashed lines are crew-cut asymptotes for lamella (5), cylinders (6), and spheres (7) from eqs 42, 36, and 25, respectively. The short-dashed line (8) is the star-like spherical asymptote (eq 18). The long dashed-short dashed line (9) denotes the asymptotic dependence for crew-cut spherical micelles for small values of N_A. While curve (4) approaches the asymptotic line (9) for small N_A, at this point the micelles have changed morphology, and therefore the asymptote (9) is not particularly relevant. The dotted-dashed line (10) denotes the variation in the core radius of star-like spherical micelles when the logarithmic term is ignored; i.e., K is set equal to unity. **(b)** Plot of the dimensionless thickness of the micelle corona Hj/a_A as a function of the degree of polymerization of the soluble block N_A. The plot shows both exact solutions and asymptote values. Thick solid curves are exact solutions of eqs 40, 32, and 15 for lamella (1), cylinders (2), and spheres (3), respectively. The thin solid lines denote the transition from one morphology to another. The dotted line (4) denotes the size spherical micelles would adopt if they did not change morphology. The dashed lines are crew cut asymptotes for lamella (5), cylinders (6), and spheres (7). The short-dashed line (8) is the asymptotic dependence for star-like spherical micelles (eq 21). The inset demonstrates that the star-like asymptote (8) for N_B=400 approaches the numerical solution only as N_A becomes on the order of 10^4. Here and in subsequent figures unless otherwise given, the model parameters are a_B = 5.6 Å, a_A = 5.0 Å, p_B= 1.5, p_A = 1.6, φ= 0.7, $\gamma/\varphi^{2/3}$ = 0.097, C_F= 1.38, and C_H= 0.68.

3.5.1.2 Star-like Spherical Micelle ($H_3 >> R_3$)

In section 3.6 we demonstrate that for a star-like micelle the stretching free energy F_{B3} of

core block *B* can be neglected. This then means that the structure of the micelle is determined by the balance of the corona and surface free energies. We calculate the scaling expression[46] for the core radius of a star-like micelle

$$R_{3star} \approx a_B \left(\frac{N_B}{\varphi} \right)^{3/5} \left(\frac{4\sqrt{3} p_A^{3/4}}{C_F K} \gamma \right)^{2/5} \sim a_B \left(\frac{N_B}{\varphi} \right)^{3/5} \left(\frac{\gamma}{K} \right)^{2/5} \qquad (18)$$

where the logarithmic term is denoted by

$$K = \ln \left(\frac{2 C_H p_A^{1/4} N_A \varphi^{1/2} a_A^2}{\sqrt{3} N_B^{1/2} a_B^2 r_{3star0}^{1/2}} \right) \qquad (19)$$

where

$$r_{3star0} = \left(\frac{N_B}{\varphi} \right)^{3/5} \left(\frac{4\sqrt{3} p_A^{3/4}}{C_F} \gamma \right)^{2/5} \qquad (20)$$

Here, r_{3star0} is the dimensionless core radius if the logarithmic dependence of the corona free energy is totally neglected, and K is treated as a constant equal to unity. This leads to the incorrect conclusion that the core radius does not depend on the length of the corona block N_A (see dotted-dashed line 10 in **Figure 4a**). In contrast to ref 46, we retain here the numerical coefficients in order to proceed below with the analysis of experimental data. The short-dashed line 8 in **Figure 4a** shows the asymptotic behavior of the core radius R_{3star} for star-like spherical micelles (eq 18). For N_B = 400 this curve is within 10% of the exact numerical solution of eq 14 for the values of the degree of polymerization of the corona block, N_A, larger than 3000.

The thickness of the corona H_{3star} in a star-like micelle is calculated as

$$H_{3star} \approx a_A N_A^{1/2} \left(\frac{4\sqrt{3}}{C_F K} \gamma \right)^{3/10} \left(\frac{N_B}{\varphi} \right)^{1/5} p_A^{7/20} \left(\frac{2C_H}{\sqrt{3}} \right)^{1/2} \qquad (21)$$

The short-dashed line 8 in **Figure 4b** shows the asymptotic behavior of the corona thickness H_{3star} for star-like spherical micelles (eq 21). For N_B = 400 this curve is within 10% of the exact numerical solution of eq 15 for the values of N_A on the order of 10^4 (see inset).

From the core radius (eq 18) one can also determine the aggregation number Q_{3star} (eq 17) of a star-like micelle as

$$Q_{3star} = \frac{4\pi\varphi}{3N_B} r_{3star}^3 \approx \frac{4\pi}{3} \left(\frac{4\sqrt{3} p_A^{3/4}}{C_F} \frac{\lambda}{K} \right)^{6/5} \left(\frac{N_B}{\varphi} \right)^{4/5} \qquad (22)$$

Figure 5 summarizes the predictions of the aggregation number Q as a function of the degree of polymerization of the corona block N_A, including the different asymptotes and the numerical solution. The solid line in **Figure 5** is the aggregation number Q of the spherical micelle calculated according to eqs 14 and 17. The short dashed line indicates the star-like asymptote Q_{3star} determined by eq 22. The dash-dotted line obtained from eqs 20 and 17 corresponds to the asymptote that does not account for the logarithmic dependence on N_A (by setting K= 1). **Figure**

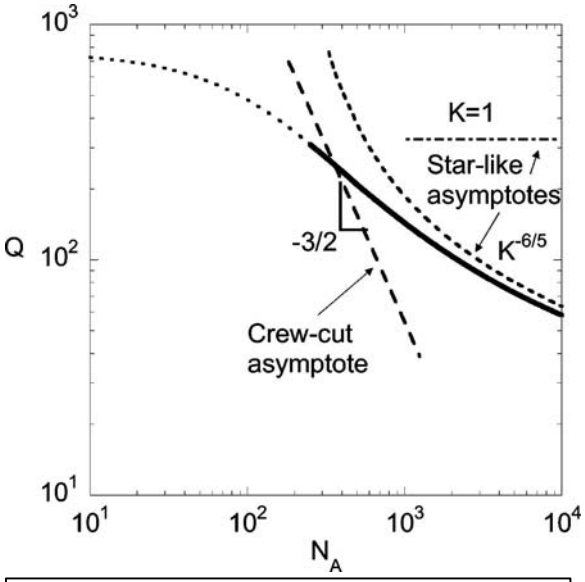

Figure 5. Aggregation number Q (eq 17) of a spherical micelle as a function of the degree of polymerization of the corona block N_A. The solid line is the analytical solution (eq 17). The dotted line is the aggregation number the micelles would have if they did not change morphology. Asymptotic dependences for crew-cut (eq 27) and star-like (eq 22) micelles are shown by long and short dashed lines, respectively. The dashed-dotted line is an asymptote for star-like micelles when eq 20 is used instead of eq 18, i.e., when the logarithmic term is equal to unity, K= 1, for all values of N_A.

5 demonstrates that in the range of $N_A \geq 10^3$ and $N_B = 400$ the star-like asymptote without the logarithmic correction (dash-dotted line) overestimates the aggregation number Q by almost an order of magnitude. The star-like asymptote with logarithmic term (short dashed line) approaches the numerical solution for $N_A > 10^3$. The asymptotic expression for the free energy per chain of star-like micelle yields

$$\frac{F_{3star}}{kT} \approx 5\gamma^{3/5}\left(\frac{C_F p_A^{-3/4} K N_B}{4\sqrt{3}\varphi}\right)^{2/5} \qquad (23)$$

Expressions 18-23 indicate that all equilibrium parameters of star-like micelles (except for the corona thickness H_3) depend only logarithmically on the molecular weight of the corona block N_A (see short dashed line in **Figure 5**). Scaling analysis often ignores logarithmic terms and treats them as constants by setting $K = 1$ (see for example dashed-dotted lines in **Figures 4a & 5**). However, as will be shown below, this weak logarithmic dependence turns out to be essential to rationalize the experimental data.

3.5.1.3 Crew-Cut Spherical Micelle ($H_3 << R_3$)

Micelles with the thickness of the corona smaller than the radius of the core are called crew-cut micelles. We emphasize that the definition of the crew-cut morphology is based on the geometric dimensions rather than on the ratio of the molecular weights of the blocks or on their contributions to the free energy of the micelle. Thus, by equating H_{3star}=R_{3star} (eqs 18 and 21), we find the scaling boundary between the two morphologies.[46]

$$N_B^*(N_A) \approx \left(\frac{2}{3}\right)^{3/4} C_H^{5/4} N_A^{5/4} \varphi \left(\frac{C_F K}{\gamma}\right)^{1/4} p_A^{1/8} \left(\frac{a_A}{a_B}\right)^{5/2} \qquad (24)$$

Here $N_B^*(N_A)$ is the degree of polymerization of the *B* block at which the size of the core is equal to the size of the corona for a given value of N_A. For a crew-cut micelle (i.e., when $N_B >> N_B^*$)

$$R_{3cc} \approx \frac{3N_B}{\varphi}\frac{a_B^2}{a_A}\left(\frac{\gamma p_A^{1/2}}{C_F C_H N_A}\right)^{1/2} \qquad (25)$$

This asymptotic dependence is depicted by line 7 in **Figure 4a**. While the absolute values are close to the numerical solution of eq 14, their functional dependence is quite different. The area per chain (eq 4) in a crew-cut micelle

$$s_{cc} = a_A a_B\left(\frac{C_F C_H N_A}{\gamma p_A^{1/2}}\right)^{1/2} \qquad (26)$$

increases as $s_{cc} \sim N_A^{-3/2}$ whereas the aggregation number defined in eq 17

$$Q_{cc} = \frac{4\pi r^3 \varphi}{3N_B} \approx \frac{36\pi N_B^2}{\varphi^2}\left(\frac{\gamma a_B^2 p_A^{1/2}}{C_F C_H a_A^2 N_A}\right)^{3/2} \qquad (27)$$

decreases as $Q_{cc} \sim N_A^{-3/2}$. The dashed line in **Figure 5** corresponds to the crew-cut asymptote Q_{3cc}, eq 27, with the slope $-3/2$ as indicated. For the chosen set of parameters these asymptotes do not look like a good approximation of full expressions (solid lines in **Figure 4 & 5**). The range of applicability of this regime is very narrow because the contribution of the core to the free energy of the micelle was ignored in both star-like and crew-cut regimes. However, with decrease of the mass of the corona block this contribution of the core to the

free energy of the micelle becomes significant. In addition, the range of the crew-cut spherical regime is narrowed by the transition to the cylindrical morphology.

For the crew-cut morphology, the free energy per chain yields

$$\frac{F_{3cc}}{kT} = 2\gamma^{1/2}\left(\frac{C_F C_H p_A^{-1/2} a_A^2 N_A}{a_B^2}\right)^{1/2} \qquad (28)$$

The corona of a crew-cut micelle can be envisioned as a quasi-planar brush. Similarly to a star-like micelle, a crew-cut micelle is stabilized by the balance of the surface and the corona free energies. Although the corona thickness is less than the core radius, the chains in the corona remain noticeably stretched, and the corona free energy still dominates over the elastic stretching of the core blocks. Asymptotic scaling dependences (eq 25-28) are therefore valid when the free energy of elastic stretching of core block *B* is negligible with respect to the free energy of corona block *A*. The lower boundary for this regime is expected when all three contributions to free energy, F_{A3}, F_{B3}, and F_{s3}, become on the same order of magnitude. This happens[46] when the molecular weight of block *B* reaches the value of N_B**

$$N_B = N_B^{**}(N_A) \cong \varphi^2 p_B p_A^{-3/4} \gamma^{-1/2} N_A^{3/2}\left(\frac{a_A}{a_B}\right)^3 \qquad (29)$$

However, as we show in section 3.6, prior to the onset of the core-stabilized regime (expected at $N_B >> N_B$**), the spherical micelles rearrange into cylindrical aggregates.

3.5.2 Cylindrical Micelle

Cylindrical micelles can be modeled by a long cylindrically shaped body with two

spherically shaped end-caps. These caps are less favorable than the cylindrical part of the micelle. The difference in the free energies per chain in spherical caps and in cylindrical parts governs the average length of the micelle.[55] In the present paper we consider cylindrical aggregates ($j = 2$) long enough that the contribution of spherical caps decorating both ends of the micelle can be neglected.

Taking into account eqs 1, 6, and 8 we represent the free energy of a block copolymer chain in a very long cylindrical micelle as

$$\frac{F_2}{kT} = \frac{\pi^2 r_2^2}{16 p_B N_B} + \gamma \frac{2N_B}{\varphi r_2} + \sqrt{2} C_F p_A^{-3/4} \frac{r_2^{3/2} \varphi^{1/2}}{N_B^{1/2}} \left[\left(1 + \frac{3}{2\sqrt{2}} \frac{C_H p_A^{1/4} a_A^2 N_A \varphi^{1/2}}{a_B^2 r_2^{1/2} N_B^{1/2}} \right)^{1/3} - 1 \right] \qquad (30)$$

By minimizing F_2 with respect to r_2 ($\partial F_2 / \partial r_2 = 0$), we arrive at the nonlinear equation that determines the equilibrium value of the dimensionless core radius $r_2 = R_2/a_B$

$$\frac{\pi^2 r_2^2}{8 p_B N_B} - \gamma \frac{2N_B}{\varphi r_2} + \frac{3}{\sqrt{2}} C_F p_A^{-3/4} \frac{r_2^{1/2} \varphi^{1/2}}{N_B^{1/2}} \left[\left(1 + \frac{3}{2\sqrt{2}} \frac{C_H p_A^{1/4} a_A^2 N_A \varphi^{1/2}}{a_B^2 r_2^{1/2} N_B^{1/2}} \right)^{1/3} - 1 \right] -$$
$$- \frac{C_H C_F}{4} \left(\frac{a_A}{a_B} \right)^2 \left(\frac{\varphi}{N_B} \right) p_A^{-1/2} \frac{N_A}{\left(1 + \frac{3}{2\sqrt{2}} \frac{C_H p_A^{1/4} a_A^2 N_A \varphi^{1/2}}{a_B^2 r_2^{1/2} N_B^{1/2}} \right)^{4/3}} = 0 \qquad (31)$$

The numerical solution of this equation is plotted as line 2 in **Figure 4a**. By substituting r_2 in eq 30, we find the equilibrium free energy per chain in a very long cylindrical micelle.

The thickness of the cylindrical corona is then

$$H_2 = R_2\left[\left(1+\frac{3}{2\sqrt{2}}\frac{C_H p_A^{1/4} a_A^2 N_A \varphi^{1/2}}{a_B^2 r_2^{1/2} N_B^{1/2}}\right)^{2/3} - 1\right] \qquad (32)$$

and the total radius of the cylindrical micelle can then be calculated as

$$R_2^{tot} = H_2 + R_2 \qquad (33)$$

The thickness of the cylindrical corona H_2 is plotted in **Figure 4b** (line 2). The aggregation number per unit length is the linear density ρ of block copolymer molecules along the cylindrical micelle

$$\rho = \frac{\pi r_2^2 \varphi}{a_B N_B} \qquad (34)$$

3.5.2.1 Asymptotic Dependencies of Cylindrical Micelles

Equations 30-34 determine the equilibrium characteristics of cylindrical micelle for arbitrary values of N_A and N_B. The asymptotic expressions for the core radius R_2 were derived by delineating and balancing the leading terms in the free energy F_2. We consider the two limiting cases of the bottle-brush ($H_2 >> R_2$) and the crew-cut ($H_2 << R_2$) micelles.

3.5.2.2 Bottle-Brush Cylindrical Micelle

Similar to star-like spherical micelles, the elastic free energy F_{B2} of core block B can be neglected for a bottle-brush micelle resulting in

$$\frac{F_{2bb}}{kT} \cong \gamma^{4/7}\left(\frac{a_A N_B}{a_B \varphi}\right)^{2/7} N_A^{1/7} p_A^{-2/7} \qquad (35)$$

By comparing F_{2bb} (eq 35) with F_{3star} (eq 23), we find that for $N_B < N_B^*$ (eq 24) corresponding to the regime with coronas larger than cores (star-like spherical and bottle-brush cylindrical micelles), $F_{3star} < F_{2bb}$. Therefore, bottle-brush cylindrical aggregates are thermodynamically unstable with respect to star-like micelles.

3.5.2.3 Crew-Cut Cylindrical Micelle

For crew-cut cylindrical micelles with $H_2 < R_2$, the situation is different. Here, the free energy per chain in the corona F_{A2} is only slightly different from the free energy per chain F_{A1} in a planar brush. Therefore, the leading terms in the free energy of crew-cut spherical and crew-cut cylindrical micelles coincide and are given by eq 28. By balancing the dominant contribution in F_{A2} (that is, free energy of the planar brush F_{A1}) with the surface energy F_s, we arrive at the equilibrium value of the surface area per chain (eq 26). The respective stability of the aggregates is determined by the corrections to this free energy due to different geometries of the micelles. The decrease of the corona free energy due to the bending of a planar corona into a cylindrical one is less than for a spherically bent corona. Therefore, the crew-cut corona prefers a spherical geometry. However, at the same area per chain the core prefers the cylindrical geometry and the equilibrium morphology depends on the balance of the core and corona free energy differences. The details of the sphere-to-cylinder transition will be discussed in section 3.6.

For a crew-cut cylindrical micelle, the asymptotic scaling laws for the core radius R_2 and the linear density of block copolymer molecules ρ are given respectively

$$R_{2cc} = \frac{2N_B}{\varphi}\frac{a_B^2}{a_A}\left(\frac{\gamma p_A^{1/2}}{C_F C_H N_A}\right)^{1/2} \qquad (36)$$

and

$$\rho_{cc} = 4\pi\gamma\frac{p_A^{1/2}}{C_F C_H}\frac{a_B}{a_A^2}\frac{N_B}{N_A\varphi} \qquad (37)$$

As shown in **Figure 4a,** the crew-cut asymptotic value of the core radius R_{2cc} (line 6) is 15-35% larger than the numerical solution of eq 31.

The free energies of spherical and cylindrical crew-cut aggregates obey the same scaling laws, and therefore the lower boundary for the crew-cut regime of cylindrical micelles is determined by the same expression as for the spherical micelles (eq 29) up to numerical prefactor. However, prior to the onset of the core-stabilized regime ($N_B = N_B^{**}$), cylindrical micelles rearrange into lamellar aggregates, and subsequent precipitation of block copolymer takes place.

3.5.3 Lamellar Morphology

We consider now a single lamellar bilayer with a condensed core of thickness $2R_1 = 2a_B r_1$ and two planar coronas with area s per chain and thickness H_1 each (**Figure 2**). Similarly to the case of cylindrical micelles, we ignore the free energy losses associated with the edges of the bilayer and limit our analysis to a very large planar aggregate.

The free energy per chain in a very large lamellar

$$\frac{F_1}{kT} = \frac{\pi^2 r_1^2}{8p_B N_B} + \gamma\frac{N_B}{\varphi r_1} + \frac{C_F C_H a_A^2 N_A \varphi r_1}{p_A^{1/2} a_B^2 N_B} \qquad (38)$$

By minimizing F_1 with respect to r_1 ($\partial F_1 / \partial r_1 = 0$), we obtain the equation that determines the

equilibrium radius (half-width) of the lamella core

$$\frac{\pi^2 r_1}{4 p_B N_B} - \gamma \frac{N_B}{\varphi r_1^2} + \frac{C_F C_H a_A^2 N_A \varphi}{p_A^{1/2} a_B^2 N_B} = 0 \qquad (39)$$

The equilibrium thickness of the corona can then be calculated as

$$H_1 = \frac{a_A^2}{a_B} C_H N_A p_A^{1/2} \left(\frac{\varphi r_1}{N_B} \right)^{1/2} \qquad (40)$$

and the surface density of the chains as

$$\sigma_1 = \frac{1}{s_1} = \frac{\varphi r_1}{a_B^2 N_B} \qquad (41)$$

The core radius $R_1 = r_1 a_B$ and the corona thickness H_1 are plotted in **Figure 4a & b** (line 1 in both figures).

By substituting the numerical solution r_1 into eq 38, we find the equilibrium free energy per chain in the lamellar aggregate. Let us consider the asymptotic scaling laws for the aggregate dimensions. If block *A* is long, lamellar aggregates would be thermodynamically unstable with respect to both spherical and cylindrical micelles. The possible stability range of the lamellae is associated with the crew-cut shape of the aggregate ($H_1 < R_1$). We therefore consider only this case.

For crew-cut micelles close to the cylinder-to-lamella transition, the dominant contribution to the free energy, $F_{1cc} \approx F_{A1cc} + F_{s1}$, is given by eq 28. Here the stretching of block *B* is neglected in comparison with the leading terms. Therefore, the area per chain s_1 is equal to s_{cc} (eq 26), and we arrive at the corresponding scaling law for lamella radius

$$R_{1cc} = \frac{N_B}{\varphi}\frac{a_B^2}{a_A}\left(\frac{\gamma p_A^{1/2}}{C_F C_H N_A}\right)^{1/2} \qquad (42)$$

As shown in **Figure 4a**, the crew-cut asymptotic value of the core radius R_{1cc} (line 5) is 20-40% larger than the numerical solution of eq 39 (line 1).

As noted above, surface area s_j is almost the same in crew-cut micelles of all considered morphologies (s_j=s_{cc}) and is given by eq 26. Therefore, micelles of different morphologies have almost the same corona thickness ($H_1 \approx H_2 \approx H_3$), whereas the core radius varies with micelle morphology as $R_j \approx jR_1$, which is the direct consequence of eq 3. **Figures 4a & b** indicates that in the range of crew-cut micelles (for short corona block N_A) the relations $H_j \approx H_1$ and $R_j \approx jR_1$ are indeed valid (see lines 1, 2 and 3).

3.5.3.1 Solubility of Lamellae in Solution

We note that the free energy per chain, $F_{1(m)}$, in the lamellar mesophase in the sediment is slightly lower than the free energy per chain, F_1, for a single bilayer in solution (eq 38) due to the van der Waals attraction energy. The dominant contribution to the van der Waals energy of lamella stack is due to the nearest-neighbor interactions. For the parallel flat stack of crew-cut lamellae (R_1>>H_1), the free energy difference $\Delta F_1 = F_1 - F_{1(m)}$ can be estimated as twice the van de Waals energy, F_W, of the two infinitely thick planar slabs (cores of the lamellae) separated by distance $2H_1$ (two corona thicknesses) to give

$$\Delta F_1 = -F_W \approx 2\frac{As_1}{12\pi(2H_1)^2} \approx \frac{As_1}{24\pi H_1^2} \qquad (43)$$

where s_1 is the area per chain in the lamella and A is the Hamaker constant.[55] We thus find

that for a lamellar mesophase with planar brush-like coronas ($H_1/\sqrt{s_1} > 1$), and a typical value of $A \cong kT$, the shift in the free energy ΔF_1 per chain is quite small, $\Delta F_1 = 10^{-2} kT$. Thus, the van der Waals attraction is negligible with respect to the free energy of a block copolymer in the aggregate, $\Delta F_1 << F_1$, and cannot affect the polymer conformation. Therefore, the instability and phase separation of block copolymer solution can be delineated from the condition $F_1=F_2$.

The structure of the sediment is determined by a hierarchy of different interactions. The dominant interaction is the attraction between *B* monomers, leading to the aggregation of block copolymer and formation of dense *B* domains. The next energy scale (still much larger than *kT* per chain) is the surface and deformation free energies. The free energy per chain, F_j, in a micelle remains much larger than *kT*. The van der Waals attraction between different aggregates keeps them together in a precipitated microsegregated phase although the van der Waals energy per chain F_W is much smaller than *kT*. The morphology of the mesophase is determined by the chemical composition of block copolymer.

Recent studies on the conformations of bilayers indicate, however, that the planar-like conformation of the coronas in lamella can be distorted due to flip-flop (redistribution) of block copolymer molecules.[56-58] Relaxation of the elastic stretching of the corona blocks *A* due to redistribution of the chains from the inner to the outer part of a curved lamella can lead to a decrease in the total free energy (with respect to the planar conformation) and cause a spontaneous curvature of the bilayer.[59,60] In this case, the sediment could comprise the distorted lamellar mesophase (locally curved lamellar sheets with the characteristic radius of curvature determined by the block copolymer composition). Our preliminary analysis indicates that in the experimentally relevant range of parameters the free energy per chain in

the curved crew-cut lamella, $F_{1(curv)}$, is only slightly (on the order of a few percent) lower than in a planar bilayer, F_1. That is, $F_1 - F_{1(curv)} = 10^{-2} F_1$, and the free energies in a planar and curved lamellae are almost the same, $F_1 \approx F_{1\,(curv)}$. Note that the van der Waals attraction for curved lamellae is weaker than for planar ones due to the larger average distance between the sheets and therefore cannot distort the polymer conformation.

Below, we delineate the cylinder-to-lamella transition and the associated instability of the solution by merely equating the free energies per chain in lamellar and cylindrical aggregates, $F_1 = F_2$.

3.6 Transitions: Sphere-Cylinder-Lamella

By comparing the equilibrium free energies (eqs 13, 30, and 38) of all three different morphologies, we can locate the sphere-to-cylinder and cylinder-to-lamella transitions and determine the ranges of stability of the spherical, cylindrical, and lamellar aggregates. **Figure 6** demonstrates typical dependences for the free energies for micelles of the three different morphologies. We choose a typical value of $N_B = 400$ and experimentally relevant set of other model parameters (specified in the legend of **Figure 4**). For this set of parameters, the free energy of a spherical micelle F_3 is the smallest ($F_3 < F_2 < F_1$) when $N_A < N_A^{sc} \approx 225$, where N_A^{sc} is the

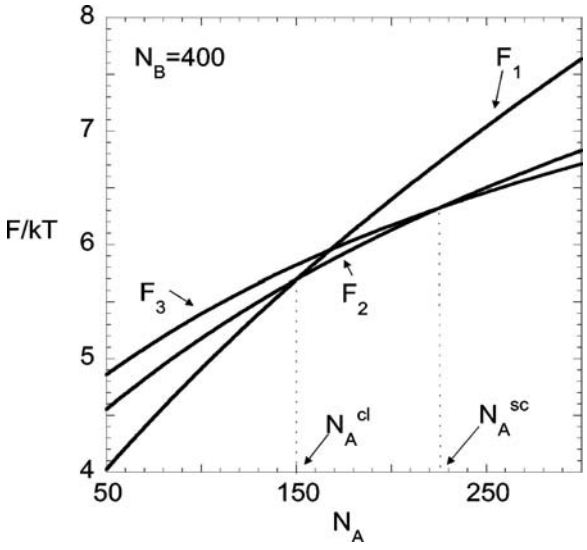

Figure 6. Free energies per chain in lamellar (F_1, eq 38), cylindrical (F_2, eq 30), and spherical (F_3, eq 13) aggregates as functions of the degree of polymerization of the corona block N_A. The vertical dotted lines indicate the cross over from spherical to cylindrical and cylindrical to lamellar micelles.

intersection point of the free energies of sphere F_3 and cylinder F_2. When $N_A < N_A^{cl} \approx 150$, where N_A^{cl} is the intersection point of the free energies of cylinder F_2 and lamella F_1, the lamellar aggregate is most stable ($F_1 < F_2 < F_3$). In the intermediate range of molecular weights, $N_A^{cl} < N_A < N_A^{sc}$, a cylindrical micelle is the optimal one. **Figure 7** demonstrates the ratio of corona thickness H and core radius R as a function of the degree of polymerization of the corona block N_A for micelles of three different morphologies for the same values of model parameters as in **Figure 4**. While this ratio is much larger than unity in the spherical region for large N_A, it becomes on the order of unity in the transition region. **Figure 7** indicates that the change in micelle morphology takes place when spheres and cylinders have a crew-cut structure, that is, when the size H of the corona is less than the core radius R. Here, for the sphere-cylinder transition at $N_A = N_A^{sc} \approx 225$ one finds the size ratio $H_3/R_3 \approx 0.45$. A slightly larger value of $H_2/R_2 \approx 0.48$ is found for the lamella-to-cylinder transition at $N_A = N_A^{cl} \approx 150$. Note that the corona-to-core size ratio H_j/R_j significantly increases during the sphere-to-cylinder and cylinder-to-lamella transitions. This increase is mostly due to the decrease of the core size R_j (**Figure 4a**) while the thickness of the crew-cut corona H_j increases only slightly (**Figure 4b**).

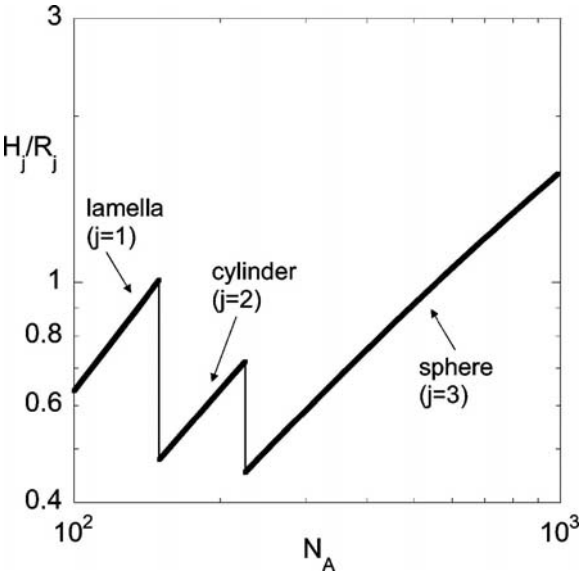

Figure 7. Plot of the ratio of the corona thickness (*Hj*) and core radius (*Rj*) in the stability range for the three different morphologies: lamella (1), cylinders (2), and spheres (3). The transition from spherical to cylindrical and cylindrical to lamellar micelles happens in the crew-cut regime when $Hj/Rj < 1$.

Approximations for the boundaries between the different morphologies can be derived

using the asymptotic scaling laws obtained in the previous section. For crew-cut aggregates in a θ-solvent ($v = 1/2$), the asymptotic free energy per chain in a micelle of morphology j = 1, 2, and 3 can be represented as

$$\frac{F_{1cc}}{kT} \approx 2\gamma^{1/2}\left(\frac{C_F C_H p_A^{-1/2} a_A^2 N_A}{a_B^2}\right)^{1/2} + \frac{\pi^2}{8}\frac{r_1^2}{p_B N_B} \qquad (44)$$

$$\frac{F_{2cc}}{kT} \approx 2\gamma^{1/2}\left(\frac{C_F C_H p_A^{-1/2} a_A^2 N_A}{a_B^2}\right)^{1/2} - \frac{1}{2}C_F p_A^{-3/4}\frac{a_A^2 h_1^2}{a_B\sqrt{s_2}\,r_2} + \frac{\pi^2}{16}\frac{r_2^2}{p_B N_B} \qquad (45)$$

$$\frac{F_{3cc}}{kT} \approx 2\gamma^{1/2}\left(\frac{C_F C_H p_A^{-1/2} a_A^2 N_A}{a_B^2}\right)^{1/2} - C_F p_A^{-3/4}\frac{a_A^2 h_1^2}{a_B\sqrt{s_3}\,r_3} + \frac{3\pi^2}{80}\frac{r_3^2}{p_B N_B} \qquad (46)$$

where $s_j = s_{cc}$ is given by eq 26 for all three morphologies and $r_j = r_{jcc} = \left(jN_B a_B^2\right)/\left(\varphi s_{cc}\right)$. The first (dominant) term in eqs 44-46 results from the balance of the surface free energy and the free energy of the planar corona. It is given by eq 28 and is the same for spheres, cylinders, and lamellae because the surface area per chain is almost the same in all three morphologies. The second (negative) terms in eqs 45 and 46 are the corrections to the free energy of planar corona due to curvature in cylindrical and spherical geometries. Finally, the last terms in eqs 44-46 are the elastic free energies of the core block B (eqs 6 and 7).

The sphere-to-cylinder transition is specified by $F_{3cc} = F_{2cc}$ and taking into account eqs 26. The asymptotic boundary between micellar phases with spherical and cylindrical morphologies is given by

$$N_A^{sc} \approx \left(\frac{21\pi^2}{20}\right)^{4/11} C_F^{-7/11} C_H^{-1}\left(\frac{a_B}{a_A}\right)^2 p_A^{5/22} p_B^{-4/11} \gamma^{3/11} \varphi^{-12/11} N_B^{8/11} \qquad (47)$$

A similar scaling dependence was obtained for the boundary between cylindrical and lamellar morphologies by equating $F_{1cc} = F_{2cc}$ (eqs 44 and 45)

$$N_A^{cl} \approx \left(\frac{\pi^2}{2}\right)^{4/11} C_F^{-7/11} C_H^{-1} \left(\frac{a_B}{a_A}\right)^2 p_A^{5/22} p_B^{-4/11} \gamma^{3/11} \varphi^{-12/11} N_B^{8/11} \qquad (48)$$

The only difference between eqs 47 and 48 is the numerical coefficient, which is smaller for the cylinder-lamellar boundary. Additionally, from the equations it is seen that the calculated scaling boundaries eqs 47 and 48 are located in the regime of crew-cut micelles. What these equations mean is that just like form SMWS micelles, the free energy is still dominated by the corona and surface free energy; however, unlike for SMWS micelles the free energy of the core is not independent of the micelle morphology. This is a direct result of the entropic penalty for stretching the core and corona blocks. As the corona block becomes shorter (while the core block is kept constant) by changing to lower curvature morphologies thereby reducing the stretching of the core block results in an entropic gain greater than the entropic lost associated with the resulting crowding the corona block causing cylindrical and lamellae morphologies to be favored.

In sections 7 and 8, experimental results for the aggregation number, hydrodynamic radius, CMC, and the location of the morphological boundaries will be compared with these theoretical predictions. However, before comparing the theoretical and experimental work, it is first necessary to explain the experimental techniques used as well as described the polymer samples that were studied.

3.7 Values of Model Parameters.

To compare the above equation with subsequent experimental data, the values of the parameters used in the previous equations need to be determined. Where possible, experimental data is used for these determinations.

3.7.1 Monomer Size *a* and Stiffness Parameter *p* of the Blocks.

We estimate monomer size *a* and stiffness parameter *p* for soluble block *A* (polyisoprene) and insoluble block *B* (polystyrene) by the following procedure. We represent each monomer as a cube of size *a,* with volume $V_0 = a^3$. Using the relationship $V_0 = M_0 / (\rho_{bulk} N_{AV})$, where M_0 is the molar mass of a monomer (in g/mol), ρ_{bulk} is the polymer bulk density, and N_{Av} is Avogadro's number, we find

$$a = V_0^{1/3} = \left(\frac{M_0}{\rho_{bulk} N_{AV}} \right)^{1/3} \qquad (49)$$

We substitute the values M_0 = 68 g/mol, $\rho_{bulk} \approx 0.9$ g/mL for PI block and M_0 = 104 g/mol, $\rho_{bulk} \approx 1.0$ g/mL for PS block to get $a_A \approx 5.0$Å and $a_B \approx 5.6$ Å

To determine the value of stiffness parameter *p* for each block, we use the experimental value of the reduced mean-square end-to-end distance in a θ-solvent, $C_\infty = R_0^2/M$, where *M* is the molar mass of the polymer. From the definition of the stiffness parameter (dimensionless analogue of C_∞) $p \equiv R_0^2/(Na^2)$ where $N = M/M_0$ is the number of monomers, we obtain

$$p = \frac{C_\infty M_0}{a^2} \qquad (50)$$

We substitute the values from ref 36 of $C_\infty \approx 0.60$ Å^{2}mol/g for PI block and $C_\infty \approx 0.43$ Å^{2}mol/g for PS block and using the values of a_A and a_B and find $p_A \approx 1.6$ and $p_B \approx 1.5$

3.7.2 Excluded-Volume Parameter *v*.

The value of the excluded-volume parameter v determines the thermodynamic quality of the solvent (heptane) for the corona block (PI). It can be obtained from static light scattering (SLS). This technique provides the value of the second virial coefficient A_2 of polymer-polymer interaction in the dilute solution. Experiments were performed for a polyisoprene sample with molecular weight 3.4×10^5 g/mol, yielding the value of $A_2 = (4.1 \pm 0.3) \times 10^{-4}$ cm^3 mol/g^2. By using the relationship[2] $v = 2A_2M_0^2/(a_A^3N_{Av})$, we find $v \approx 0.05$. Substituting a_A = 5 Å, $p_A = 1.6$, and $v = 0.05$ into the expression for the thermal blob size $\xi_t \cong a_A p_A^2 v^{-1}$, we estimate $\xi_t \cong 260$ Å. The largest blob in the corona is the last blob in the spherical star-like micelle with the largest soluble block with degree of polymerization $N_A \cong 1443$ (sample 39-94 in Table 1). Its size ξ_{last} can be estimated as

$$\xi_{last} = \frac{R_3^{tot}}{\sqrt{Q}} p_A^{3/4} \qquad (51)$$

By calculating the size R_3^{tot} (eq 16) and aggregation number Q (eq 17) for sample 39-94, we find $\xi_{last} \cong 70$ Å. Because $\xi_t > \xi_{last}$, the excluded-volume interactions do not significantly modify the chain conformation. Therefore, chain conformations in all other (smaller) blobs in spherical, cylindrical, and lamellar micelles are also Gaussian. Thus, despite the positive value of second virial coefficient A_2, heptane is apparently a θ-solvent for

PI block in the micellar corona wherein all correlation blobs are smaller than the thermal blob.

3.7.3. Dimensionless Surface Tension γ and Volume Fraction φ of Polymer in Micellar Core.

As noted earlier, the dimensionless surface tension γ and volume fraction φ are not independent variables. Both parameters depend on the solvent quality. For weakly poor solvent for *B* block, the relatively small value of polymer volume fraction φ in the core of the micelle is determined by the ratio of the attractive second and the repulsive third virial coefficients of monomer-monomer interactions. The dimensionless surface free energy γ can be approximated[48,49] in the range of small $\varphi << 1$ as $\gamma = \gamma_1 \varphi^2$. (Here, γ_1 is a numerical coefficient on the order of unity.) However, at relatively high polymer concentrations higher-order interactions become significant, and simple scaling models fail. Therefore, to facilitate comparison between theory and experiment, we do not make a priori assumptions about the relationship between γ and φ at high values of $\varphi \leq 1$ but try to estimate them independently of each other from different experiments.

A convenient method to evaluate γ was proposed in ref 50. The static light scattering (SLS) technique was used to examine solutions of PS in heptane and to determine the solubility of PS as a function of temperature and molecular weight. Heptane is a poor solvent for PS, and the solution separates into a denser phase (sediment) with polymer concentration φ and a dilute phase that contained individual globules of collapsed PS. The equilibrium concentration φ' of polymer in the dilute phase was determined from the light scattering data

for PS samples with three different molecular weights. The chemical potential of a globule in the dilute phase, μ_g, was approximated as

$$\mu_g \approx kT \ln(\varphi' / N_B) + F_{s0} + F_0 \qquad (52)$$

where $F_{s0} \sim kT\gamma N_B^{2/3}$ is the surface free energy of the globule, eq 10, and F_0 is the free energy per chain of monomer-monomer interactions in the condensed state. The chemical potential of polymer in the sediment is dominated by the bulk while the surface contribution is negligible. This gives

$$\mu_p \approx kT \ln(\varphi / N_B) + F_0 \qquad (53)$$

Equilibrium between dilute phase and sediment implies equality of chemical potentials, $\mu_g = \mu_p$. Therefore, the concentrations in the two phases, φ and φ', are related through the equation

$$\ln(\varphi') - \ln(\varphi) + (36\pi)^{1/3} \gamma (N_B / \varphi)^{2/3} = 0 \qquad (54)$$

Assuming that polymer volume fraction in the sediment $\varphi \leq 1$ and $\varphi >> \varphi'$, we omit $\ln(\varphi)$ in eq 54. Then the ratio $\ln(\varphi')/N_B^{2/3}$ is expected to be independent of the molecular weight of polymer N_B and to depend only on temperature T. The data in ref 48 indicated that, for all three molecular weights investigated, the dependence of $\ln(\varphi')/N_B^{2/3}$ on temperature

can be approximated by a single straight line, (0.68 ± 0.01) - (5.2 ± 0.2) × 10^{-3}(T - 273), where T is the absolute temperature. We can therefore calculate the ratio $\gamma/\varphi^{2/3}$ from eq 54 as

$$\frac{\gamma}{\varphi^{2/3}} = \frac{(0.68 \pm 0.01) - (5.2 \pm 0.2) \times 10^{-3}(T - 273)}{(36\pi)^{1/3}} = \\ = (0.14 \pm 0.002) - (1.07 \pm 0.04) \times 10^{-3}(T - 273) \qquad (55)$$

We anticipate that freezing of micelles (lack of micelle equilibration in response to the temperature variation) occurs somewhere between 20 and 60°C. In our comparison of the theory with experimental data at room temperature, we choose the value of $\gamma/\varphi^{2/3} \approx 0.097$ corresponding to the freezing temperature T - 273 ≈ 42 °C.

This provides the ratio of two unknown parameters γ and $\varphi^{2/3}$. The values of polymer volume fraction φ in the micellar core of series 2 micelles were estimated from neutron scattering experiments that will be described in section 6.1.3.2 and 6.1.4. The measured values of polystyrene volume fraction φ in the core are in the range of φ = 0.5-0.7. To facilitate the comparison between theory and experiment, we choose φ = 0.7 as the representative value. Note that for polymer volume fraction φ = 0.7 the logarithmic correction ln(φ) omitted previously in eq 54 does not affect the ratio $\gamma/\varphi^{2/3}$ in eq 55 (the difference is within the experimental error).

We emphasize that the uncertainty in some of the experimental measurements (e.g., φ) gives us certain freedom in choosing the specific values of the corresponding model

parameters. Under these conditions, the choice is dictated by a better fit between theory and experiment. At this point, there are still two unspecified dimensionless parameters, C_H and C_F (numerical coefficients expected to be on the order of unity). From comparison with experiments we fix the values of $C_F = 1.38$ and $C_H = 0.68$.

4. Experimental Techniques

As mentioned in Section 1.4, due to the large size variation in micelles, from 10 nm spheres to μm sized vesicles, several different techniques are needed to study them. Scattering techniques have the advantage of being able to sample large numbers of micelles in their native environment over a range of sizes, depending on the scattering wavelength. However, they require fitting the data to various models—which might or might not be accurate for the micelles being studied. On the other hand, from visualization techniques one is able to directly observe the micelle shape and size. However, in order to observe the micelles, they usually need to be taken out of their native environment. Visualization techniques also look at a much smaller sampling meaning that the statistics are not as good as for scattering techniques.

4.1 Scattering

All scattering techniques are based on the interaction of electromagnetic waves with the sample. Depending on what source of scattering particles is used, the scattering is sensitive to different parts of the atom. In addition, the different scattering sources have

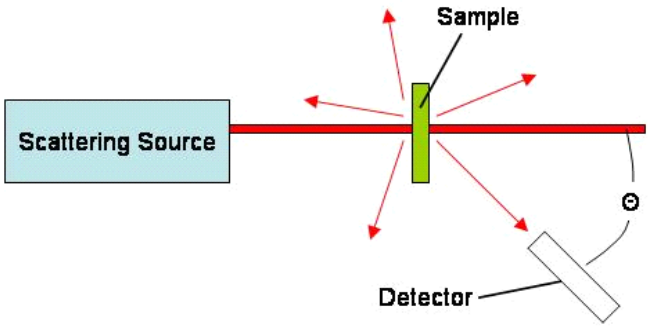

Figure 8. The electromagnetic radiation is directed from the source to the sample. The interaction of the radiation with the sample causes the radiation to be scattered in all directions. By monitoring the variation in the scattering intensity as a function of angle (θ) the size and shape of the sample can be determined.

different wavelengths, affecting the length scales on which they are able to extract information. This difference in wavelengths effects the scattering wave vector $q = \frac{4\pi n}{\lambda}\sin\left(\frac{\theta}{2}\right)$ where n is the refractive index of the solvent, λ is the wavelength of the electromagnetic waves, and θ is the scattering angle (**Figure 8**). The value of $2\pi / q$ gives the size of the scattering window, i.e. the length scale on which the scattering is taking place. This means that as the wavelength of the scattering media gets larger and the scattering angle gets smaller, the scattering window gets larger. Since geometric constraints set the maximum and minimum angle that can be measured, there is a limited q range for each of the scattering techniques that is easily accessible. Typical light scattering q values range from ~0.006 - 0.06nm^{-1} where as those for small angle X-ray and Neutron scattering range from ~0.2 - 20nm^{-1} and ~0.06 - 10nm^{-1} respectively.

When the product of q and the radius of gyration (R_g) are less than one, i.e. $qR_g < 1$ the mass of the scattering particles can be determined from the intensity when both q and the concentration (c) equal zero, since this value can not be directly measured, the intensity as a function of q and c is extrapolated to zero q and c to determine the mass of the sample. In addition to measuring the mass of the sample, when $qR_g < 1$, it is also possible to measure the radius of gyration from the variation in the scattering intensity with q and the second viral coefficient from the variation in scattering intensity with concentration.. As the value of q is further increased, the dimensionality of the objects with non-uniform shapes, such as discs and rods, can be determined when $2\pi/x < q < 2\pi/y$ where x is the large lateral dimension, i.e. the length of a rod or diameter of a disk, and y is the smaller lateral dimension, i.e. the diameter of a rod, or thickness of a disc. As the q value is increased even further, the

scattering takes place primarily at the surface of the particles creating characteristics minima and maxima the spacing of which depends on the shape and curvature of the surface.

4.1.1 Light Scattering ($q \sim 0.006\text{-}0.06 nm^{-1}$)

When light is used as the electromagnetic radiation, the light waves cause perturbations in the electron density of the sample, causing light to be scattered in all directions. Light scattering is typically performed on wavelengths from 400-800 allowing for the characterization of particles from ~100nm-1μm. Light scattering can be performed in two different modes—static and dynamic. In static light scattering, the average scattering intensity is measured, whereas in dynamic the temporal fluctuations in the scattering intensity are measured.

4.1.1.1 Static Light Scattering

In static light scattering the light source (typically a laser) is focused onto the sample. A photo multiplier is then used to measure the intensity of light scattered at various angles (**Figure 8**). The ratio of the scattered light to the incident light is called the Rayleigh ratio (R_θ). From the Rayleigh ratio the mass of the scattering particles can be measured at low angles as a function of concentration as

$$R_\theta = \frac{4\pi^2 n^2}{\lambda^4}\left(\frac{dn}{dc}\right)^2 \frac{cM_w}{N_{Av}} = KcM_w \qquad (49)$$

where n is the refractive index of the solvent, λ is the wavelength of light used $K = 4\pi n^2 (dn/dc)^2 / (\lambda^4 N_{AV})$ is the optical constant, N_{Av} is Avogadro's number, c is the concentration of polymer in solution, dn/dc is the specific change in refractive index for a

polymer solvent pair and M_w is the weight average molecular weight of the sample. If the sample is measured at several concentrations the weight average second virial coefficient can also be determined from the higher order moments as

$$\frac{Kc}{R_\theta} = \frac{1}{M_w} + 2A_{2,z}c + \ldots \qquad (50)$$

If instead of measuring the scattering intensity as a function of concentration at a fixed low angle, the radius of gyration (R_g) can be measured from the angular dependence of the R_θ at low concentration as

$$\left(\frac{Kc}{R_\theta}\right)_{c\to 0} = \frac{1}{M_w}\left[1 + \frac{16\pi^2 n^2}{3\lambda^2}\left\langle R_g^2\right\rangle_z \sin^2\left(\frac{\theta}{2}\right) + \ldots\right] = \frac{1}{M_w}\left[1 + \frac{1}{3}q^2\left\langle R_g^2\right\rangle_z + \ldots\right] \qquad (51)$$

By plotting both the angular and concentration dependences together, a Zimm plot is formed which allows for the determination of the mass of the sample, the radius of gyration, and the second virial coefficient.

4.1.1.2 Dynamic Light Scattering

In dynamic light scattering the variation in the scattering intensity with time, as particles move in and out of the scattering volume, is measured. These variations in scattering intensity are then correlated together providing the diffusion coefficient of the sample. From the diffusion coefficient, one can then determine the hydrodynamic radius

$$R_h = \frac{kT}{6\pi\eta D} \qquad (52)$$

where k is the Boltzmann constant, T is the temperature of the sample, η is the solvent viscosity, and D is the diffusion coefficient.

4.1.2 X-ray Scattering ($q \sim 0.05\text{-}10 nm^{-1}$)

X-ray scattering is based on the same principle as light scattering except that X-rays radiation is used instead of visible light. X-rays typically have wavelengths ranging from 0.3-3nm. X-rays are still sensitive to the electron density, however the higher energy of the x-rays means that greater electron density is needed. The shorter wavelength of X-rays allows the characterization of the sample on smaller length scales than is possible with light scattering. In addition, since X-rays are able to penetrate more, they can be used to characterize opaque samples.

4.1.3 Neutron Scattering ($q \sim 0.06\text{-}10 nm^{-1}$)

Neutron scattering is based on the same principles as light scattering, except that neutrons are used instead of photons. The wavelength of neutrons is directly related to their velocity, therefore by selecting neutrons of differencing velocity, the wavelength can be varied over a small range, typically 0.1-0.2nm. Since neutrons have a smaller wavelength than X-rays or visible light, neutron scattering should be able to probe the smallest sizes. However the need to contain the radio active neutrons makes wide angle neutron scattering impractical, thus SANS and WAXS have a similar q range and thus are able to probe similar sized particles. Unlike light and X-ray scattering, neutrons do not interact with the electrons, instead neutrons are scattered by the sample nuclei. In addition since the scattering intensity from hydrogen and deuterium are very different, deuterium can be used to mask parts of the sample that one does not want to scatter.

4.2 Atomic Force Microscopy

Atomic force microscopy (AFM) is a relatively new technique having only been invented in 1986. In AFM the sample is adsorbed onto a solid substrate. In the standard mode of operation, referred to as contact mode, a sharp tip on the end of a flexible cantilever is then brought into contact with the substrate. As the tip is moved across the substrate, the cantilever flexes as the tip goes over higher and lower areas. By measuring the deflection of the cantilever, one is able to map out the height profile of the sample. This allows for the direct determination of the size and shape of the sample. In a second mode of operation called taping mode, instead of bringing the tip into contact with the surface, the cantilever is oscillated above the surface. As the oscillating tip approaches higher and lower features, the interaction of the tip with the surface changes the resonance frequency of the tip and thus reduces the oscillation amplitude at the scanning frequency (which is kept constant). By monitoring the variations in the amplitude, one is able to determine the height profile of the sample. Since in tapping mode the AFM tip touches the surface only intermittently, tapping mode is able to characterize softer and weakly adhered samples that would be altered by the tip in contact mode.

4.3 Differential Scanning Calorimetry

In differential scanning calorimetry (DSC) the sample and a reference are heated. The amount of current it takes to keep both the sample and the reference at the same temperature is measured. By looking at the differences in the applied currents, thermal transitions in the sample can be detected. In such a way one is able to determine melting and glass transition temperatures (Tg) as well as heat capacities, heats of fusion, and enthalpies of reactions.

Since melting and glass transitions alter the rate of heat transfer, one is able to determine at what temperature the sample melts or undergoes a glass transition.[61] In this work, DSC will be used to measure the Tg depression of the PS core as it is swelled with heptane (Section 6).

5. Polymer Samples

Four different series of polystyrene-b-polyisoprene diblocks were used during these experiments. **Table 1** gives the molecular weights and degree of polymerization for each block of all the samples.

Series 1 and 2 were purchased from Polymer Standards Service (Germany) and had constant PS blocks of 35 and 40kD. An additional sample with a PS block of 40kD and a PI block of 10kD was purchased from Polymer Source Inc. (Canada). Marinos Pitsikalis and Nikos Hadjichristidis from the University of Athens synthesized series 3 and 4, which had constant PS blocks of 19 and 20kD and were synthesized by high vacuum anionic polymerization techniques.[62] Styrene was polymerized in benzene at room temperature using s-BuLi as initiator. A small quantity of the living PS-Li solution was sampled for characterization and the rest was divided to calibrated cylinders, which were removed from the polymerization apparatus by heat sealing. The PS-Li content of each cylinder was used to initiate the polymerization of a predetermined amount of isoprene in separate polymerization apparatuses in order to prepare PS-b-PI block copolymers with the desired molecular weight of the PI block. The copolymers were precipitated in methanol and fractionated in toluene/methanol as the solvent/non-solvent system in order to remove traces of deactivated PS block during the synthesis. The purified copolymers were precipitated in methanol and dried under vacuum.

Table 1:
Molecular Weights and Degree of polymerization of Studied Polymer Samples

Series 1

Sample	Total Mw	PS Mw	PI Mw	PDI	N_{PS}	N_{PI}
40-10	51000	40800	10200		392	151
40-12	48400	35600	12800	1.04	335	171
40-13	50700	35600	15100	1.06	335	191
40-17	54100	35600	18500	1.04	335	254

Series 2

Sample	Total Mw	PS Mw	PI Mw	PDI	N_{PS}	N_{PI}
39-8.9	50900	40900	10000	1.05	383	131
39-9.2	51200	40900	10300	1.04	383	135
39-10.5	53100	40900	12200	1.06	383	154
39-11.4	53400	40900	12500	1.04	383	168
39-11.7	53200	40900	12300	1.03	383	172
39-13	55200	40900	14300	1.04	383	194
39-15	57500	40900	16600	1.05	383	222
39-25.6	68900	40900	28000	1.05	383	376
39-52	95100	40900	54200	1.04	383	765
39-94	139000	40900	98100	1.04	383	1385

Series 3

Sample	Total Mw	PS Mw	PI Mw	PDI	N_{PS}	N_{PI}
20-9	28700	19400	9300	1.03	187	285
20-13	32000	19400	12600	1.02	187	285
20-14	33000	19400	13600	1.02	187	285
20-19	38600	19400	19200	1.02	187	285
20-26	45300	19400	25900	1.02	187	285
20-59	78100	19400	58700	1.02	187	285
20-99	118000	19400	98600	1.02	187	285
17-8	25000	17200	7800	1.03	165	253
17-72	89200	17200	72000	1.04	165	253

Series 4

Sample	Total Mw	PS Mw	PI Mw	PDI	N_{PS}	N_{PI}
21-4	24900	20600	4300	1.03	190	64
21-6	26600	20600	6000	1.04	190	85
21-7	27200	20600	6600	1.04	190	93
21-8	28400	20600	7800	1.04	190	110
21-11	31400	20600	10800	1.04	190	153
21-39	59600	20600	39000	1.04	190	551

The total molecular weight as well as the weights of each block are given for all polymer samples studied. In addition the polydispersity index (PDI) along with the degrees of polymerization for the PS block (N_{PS}) and the PI block (N_{PI}). The molecular weights given in the table are those reported by the institutes at which the polymers were synthesized

The 19 and 20kD PS samples were characterized by size exclusion chromatography (SEC) and low angle laser light scattering (LALLS) at The University of Athens. SEC experiments were conducted at 40°C using a modular instrument consisting of a Waters Model 510 pump, a Waters Model U6K sample injector, a Waters Model 401 differential refractometer, a Waters Model 486 UV spectrophotometer, and a set of 4 m-Styragel columns with a continuous porosity range from 10^6 to 10^3 Å. The columns were housed in an oven thermostated at 40°C. THF was the carrier solvent at a flow rate of 1ml/min.

The LALLS measurements were performed with a Chromatix KMX-6 low angle laser light scattering photometer at 25°C equipped with a 2mW He-Ne laser operating at λ=633 nm. Stock solutions were prepared, followed by dilution with solvent to obtain appropriate concentrations. All solutions and solvents were optically clarified by filtering through 0.22μm pore size nylon filters directly into the scattering cell. Refractive index increments, dn/dc, at 25°C were measured with a Chromatix KMX-16 refractometer operating at 633 nm and calibrated with aqueous NaCl solutions.

The molecular weights of most of the samples were confirmed by static light scattering at UNC. **Table 2**

Table 2.
MW Comparison

Series 1

sample	UNC Total MW	PSS Total MW
40-12	49	48.4
40-13	54	50.7
40-17	59	54.1

Series 2

sample	UNC Total MW	PSS Total MW
39-11.7	58	53.2
39-13	62	55.2
39-15	64	57.5
39-25.6	81	68.9
39-52	105	95.1
39-94	165	139

Series 3

sample	UNC Total MW	Athens Total MW
19-9A	26.4	28.7
19-13A	27.7	32
19-14A	24.7	33
19-19A	32.5	38.6
19-26A	36.7	45.3
19-59A	78.4	78.1
19-99A	120.0	118
17-7	22.0	25
17-72	96.8	89.2

Comparison between the total molecular weights of diblocks samples measured by static light scattering at UNC and as reported by the institute of origination. All molecular weights are reported in kDa.

compares the reported molecular weights and those measured at UNC by SLS. The purity of the samples (i.e. lack of homopolymers) was verified by dynamic light scattering using the procedure that follows.[44]

5.1 Detection of Residual Homopolymer

It is known that PS-PI diblocks prepared by anionic polymerization may contain small fraction of linear PS. Here we present a comparative analysis of two PS-b-PI samples of approximately the same composition (the numbers in brackets indicate molecular weights of the blocks) and outline a procedure for detecting small amounts of residual homopolymer. Sample 1: PS(39800)-b-PI(11400) Sample 2: PS(39800)-b-PI(11700)

Figure 9 shows the molecular weight distributions obtained by gel permeation chromatography (GPC) in THF of Samples 1 and 2, respectively. Both samples show relatively narrow and monomodal elution curves. This shows that the samples are quite pure. However, in our case, it is difficult to detect the small fraction of the PS homopolymer because of the small difference between the diblock molecular weight (51.2 kDa) and the molecular weight of the PS block (39.8 kDa). More precise analysis can be done by static and dynamic light scattering measurements in cyclohexane. This is possible because cyclohexane has a θ-temperature (temperature at which cyclohexane behaves as an ideal solvent) for PS at 26.5°C. Since the

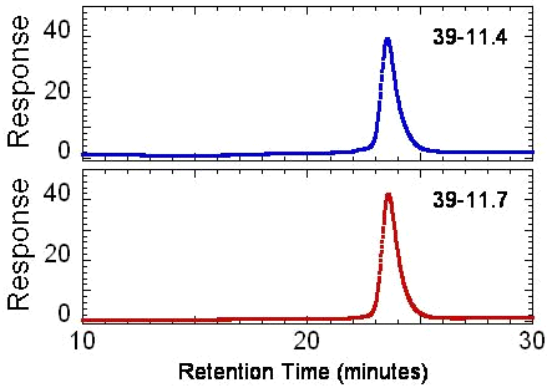

Figure 9. The top plot is a GPC trace of Sample 1 PS(39800)-b-PI(11400). The bottom plot is a GPC trace of Sample2 PS(39800)-b-PI(11700). Both samples were run in THF at a rate of 1ml/minute.

solubility behavior of the polymer is highly dependent on temperature near the θ-temperature, by heating and cooling the sample, residual PS homopolymer can be solubilize and then precipitated.

Figure 10A depicts intensity vs. particle diameter measured for Sample 1 at a higher temperature of 29°C obtained using Brookhaven's CONTIN fit from dynamic light scattering. The curve shows only one peak with a hydrodynamic diameter of approximately 10nm. If one decreases the temperature down to 20°C (i.e. below the theta temperature of polystyrene in cyclohexane), a second peak emerges with a diameter of about 644 nm (**Figure 10B**). We believe this peak corresponds to aggregates of precipitated PS homopolymer. While the peak of the larger radius species looks big, one must note that the Y-scale is in relative intensities and that the scattering of a few large particles will have a much higher intensity than the same number of particles of a small size. Since the intensity for the particles of larger diameter is not that much higher than the intensity for the diblock, the actually amount of homopolymer is small, yet significant. Thus we conclude that Sample 1 contains a small fraction of PS homopolymer. **Figures 11 A and**

(A) T(°C)=29

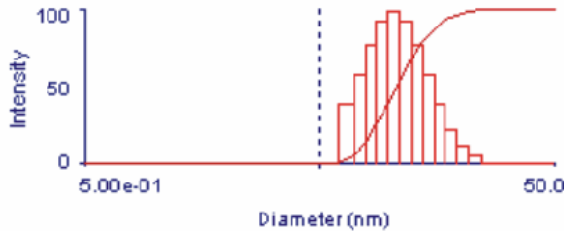

(B) T(°C)=20

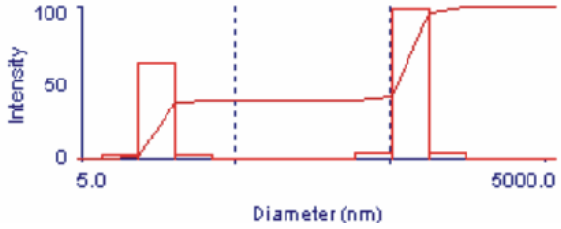

Figure 10. Contin fit of dynamic light scattering data for sample 39-11.4 with a concentration of 0.019g/ml. Plot A was measured at 29°C and plot B was measured at 20°C. When the sample is cooled to 20°C there is a large contribution of the larger species (aggregated polystyrene). While the intensity of the larger diameter species is much greater, it must be remembered that larger object have a much higher scattering intensity than small ones. Thus well the contribution of the larger species toward the total scattering intensity is significant, the actually amount of aggregated polystyrene is relatively small.

B depicts two intensity-vs.-particle diameter curves for Sample 2, which were also measured at 29°C and 20°C, respectively. In contrast to Sample 1, at low temperatures the second peak, which appears slightly at a diameter of 400nm, is so small that it is barely observable. Again since large particles scatter more intensely than small ones, the amount of homopolymer is found to be so minuscule that it is insignificant. For the experiments presented in this paper the same characterization was carried out on all samples and no significant amount of homopolymer was found in the main samples that were used.

(A) T(°C)=29

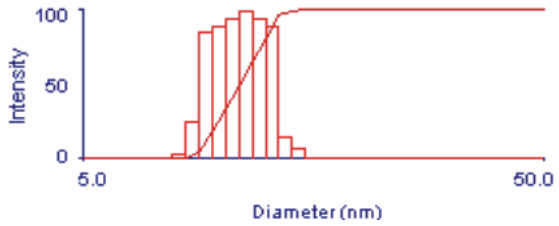

(B) T(°C)=20

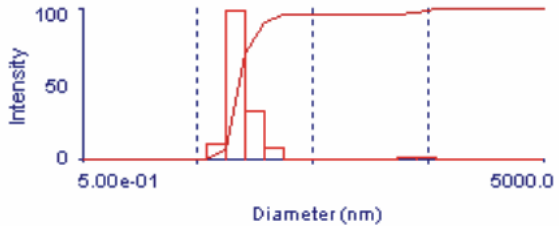

Figure 11. Contin fit of dynamic light scattering data for sample 39-11.7 with a concentration of 0.021g/ml. Plot A was measured at 29°C and plot B was measured at 20°C. Unlike for sample 39-11.4, at 20°C there is only a small contribution of the larger species (aggregated polystyrene). This means that there is very little homopolymer in the sample.

The molecular weights and degree of polymerization as reported from the respective companies and universities for all samples are given in **Table 1**. **Table 2** presents a comparison on the MW measured at UNC and the institutions from which the samples originated. All solvents used for the micelle characterization were purchased from Fisher Chemicals or Acros Organics, and were filtered through 0.2µm NALGENE PTFE filters to remove any dust particles, prior to use.

6. Micelle Equilibration

When studying polymer micelles, it is important to make sure that the micelles are in equilibrium. This is especially important for micelles formed with cores that could vitrify causing the micelles to become quenched in a non-equilibrium state. For example, micelles in which a cylindrical morphology is favored can remain spherical infinitely long. Or, micelles that should grow (either in diameter or in length) in response temperature changes will remain small, leading to fundamental misinterpretations. Quenching of the core can be caused by various factors, e.g. crystallization and vitrification below crystallization and glass transition temperatures, respectively. The temperatures, in turn depend on the fraction of polymer in the core, i.e. solvent quality.

In this work, we deal with vitrification of the PS core in the presence of n-heptane and d-heptane. As such it is of paramount importance to ensure that the micelles are in equilibrium. One possible way to do this is to look at the variation in the aggregation number with temperature jumps near the CMC. A second way is to look at the mixing of two different micelle morphologies. If the different morphologies combine to form an intermediate morphology, then unimer exchange is taking place. A final way is to directly measure the Tg of the core through DSC.

6.1 Aggregation Number Near the CMC

Since the solvent quality of heptane for polystyrene changes with temperature, the aggregation number also changes with temperature. By following the variation in the micellar aggregation number, one can verify that the micelles are in equilibrium by measuring the change in aggregation number with temperature. This change becomes more noticeable near the critical micelle concentration (CMC) where the micelles are more sensitive to temperature. The CMC will be discussed in a later section of this paper.

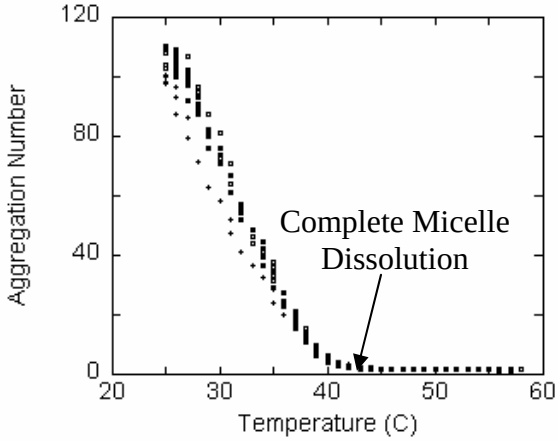

Figure 12. The variation in the aggregation number of sample 19-26 with temperature for two heating and cooling cycles as measured by SLS. A concentration of $6.2*10^{-5}$g/ml was used.

To study the change in aggregation number with temperature, we used a procedure similar to Honda *et.al.*[63] except that we used temperature ramps instead of temperature jumps, the details of this procedure are outlined in the appendix. When the procedure was done for the 20kD series, all of the samples were found to go from micelles to unimers reproducibly in the temperature range of 25-40ºC as seen in **Figure 12** This indicates that the 20kD series is in equilibrium at 25ºC.

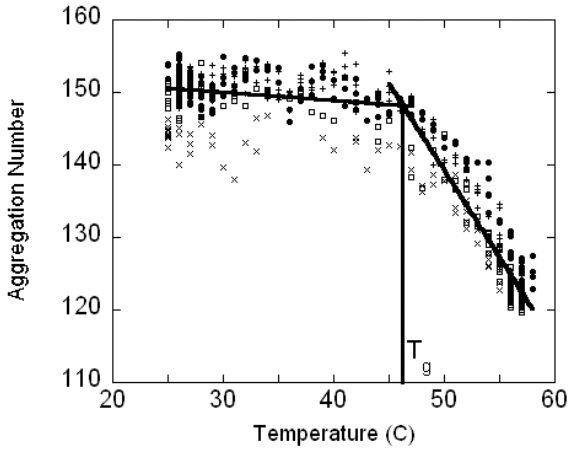

Figure 13. Plot of the variation in the aggregation number with temperature for two heating cycles and two cooling cycles for sample 39-26 as measured by SLS. A concentration of $3.7*10^{-6}$g/ml was used.

When the same procedure was done with the 40kD series, as seen in **Figure 13** the variation

in aggregation number with temperature for the 40kD series is reproducible for two heating and two cooling cycles. While the data is reproducible, it becomes apparent that at temperatures below ~45ºC the aggregation number no longer changes with temperature. We believe that this indicates a glass transition temperature (T_g) of the PS core, which freezes and the micelles are no longer able to change their aggregation number. A significant feature of this data is that for the 40kD series the apparent T_g changes with the size of the soluble block (**Figure 14**). There are several possible explanations for this. First it is possible that the density of the core is changing with the size of the soluble block as will be discussed in section 7.1.4. If this is the case, the amount of solvent plasticizing the core changes causing a change in the T_g. A second explanation is that the variation in core size is what is causing the change in T_g. Even though the presence of a T_g indicates that micelles formed from the 40kD series are out of equilibrium at temperatures bellow the T_g, the data on the aggregation number and hydrodynamic radius agree well with theory. This is explained by the aggregation number and size of the micelles (measured well above the CMC) not being very sensitive to temperature, compared to the strong dependence in the CMC region.

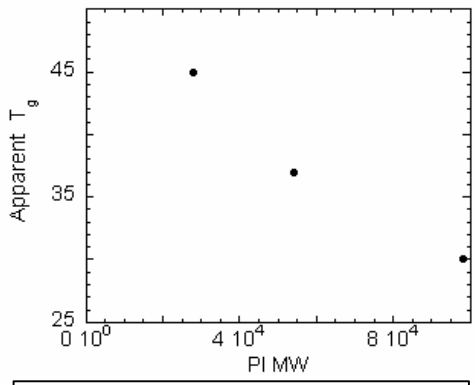

Figure 14. Plot of the apparent T_g variation with PI molecular weight as measured by SLS.

These results on the equilibration of micelles highlights an important issue—that micelle equilibration can vary with the size of the blocks, and even within a given block-copolymer system, e.g. PS-b-PI diblocks, some samples can be in equilibrium while others are not.

6.2 Mixed Micelles

A second way to study micelles equilibration is to look at the mixing to two different micelle species. If there is a change from two different species to one single uniform species, it means that there is exchange of unimer between the micelles. Due to the large difference in scattering between cylindrical and spherical micelles, the mixing of cylindrical and spherical micelles can be followed in-situ by light scattering. If two micelles composed of different sized diblocks are mixed, individual diblocks will be extracted from the micelles and inserted into other micelles. This exchange of diblocks between micelles will result in the original micelles being composed of both diblocks and adopting an intermediate morphology as illustrated in **Figure 15**.

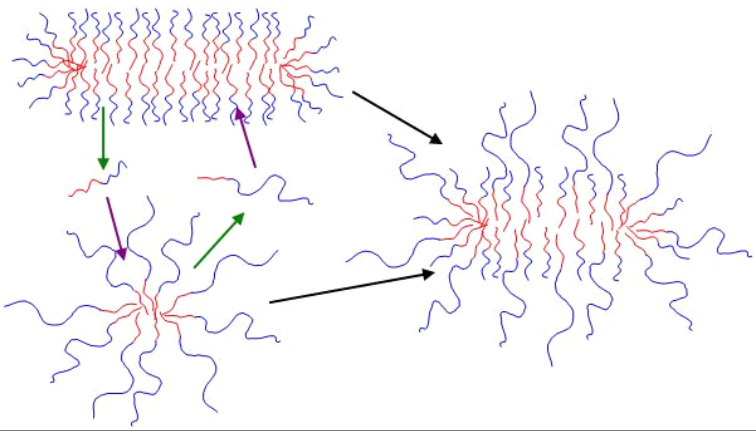

Figure 15. Cartoon illustration of unimer exchange during micelle mixing. If two micelles composed of different sized diblocks are mixed, individual diblocks will be extracted from the micelles (green arrows) and inserted into other micelles (purple arrows). This exchange of diblocks between micelles will result in the original micelles being composed of both diblocks and adopting an intermediate morphology (black arrows).

As such mixtures of 39-11.7 and 39-94 were mixed at different temperatures and the evolution of the scattering intensity was

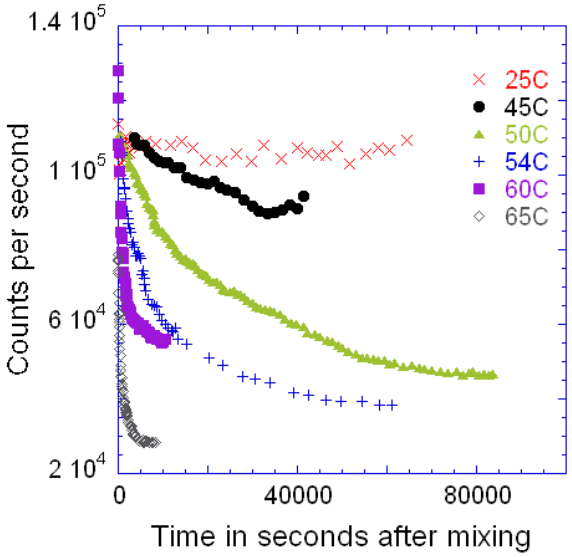

Figure 16. Variation in the scattering intensity when spherical (39-94) and cylindrical (39-11.7) micelles are mixed at different temperatures. At 25°C no exchange is seen. At temperatures above 45°C unimer exchange is observed, the rate of which increases with increasing temperature.

followed. As seen in **Figure 16** at 25°C no change in the aggregation number was observed. This means that there is little or no unimer exchange at 25°C. At 45°C there is a noticeable change in the scattering intensity indicating that morphology is changing, i.e. unimer exchange is taking place between the two different micelle morphologies. As the temperature is increased further, the rate of exchange also increases.

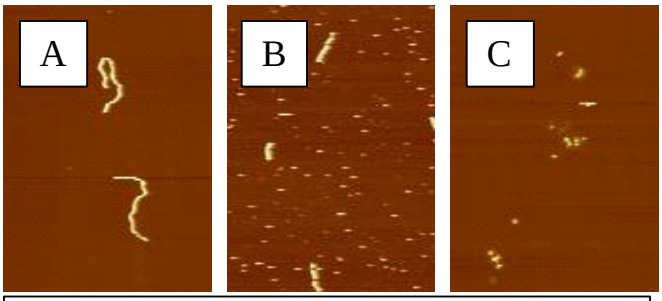

Figure 17. AFM images of mixtures of spherical (39-94) and cylindrical (39-11.7) micelles. The fraction of cylindrical micelles is 1.0, 0.8, and 0.6 respectively for images A, B, and C. The samples were heated to 60°C for 24 hours.

In addition to following micelles mixing with light scattering, AFM can be used to measure the average cylindrical micelle length ex-situ. **Figure 17** shows AFM images of 3 different mixtures of spherical and cylindrical micelles. After being heated to 60°C for 24 hours, the average length of the cylindrical species varied with the weight fraction of cylindrical micelles used in the mixture. The mixtures have a fraction of cylindrical micelles or 1.0, 0.8, and 0.6 had number average lengths of 5.5±0.8, 2.0±0.4, and 0.8±0.3μm respectively.

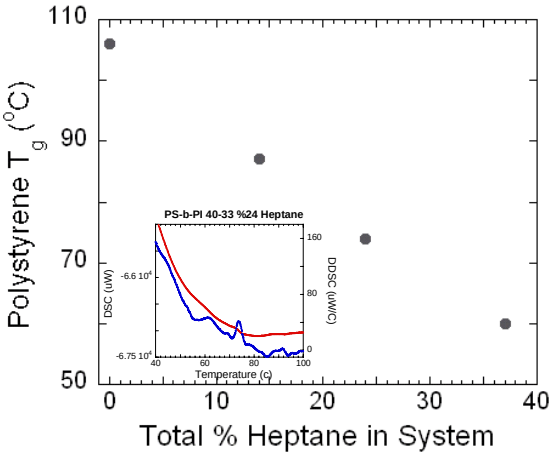

Figure 18. Variation in the T_g of the PS block of a PS-b-PI diblock as the total amount of heptane in the system is increased. The insert show one of the actual GPC traces for PS-b-PI 40-33 with 24% heptane.

6.3 DSC Measurements

It is well know that solvent can act as a plasticizer and depress the T_g of polymers.[64] This means that if heptane is present in the

micellar core, that the T_g of the core will be depressed below the bulk PS T_g of 106°C. As such, DSC measurements were performed to try to measure the T_g of the core. As seen in **Figure 18**, the T_g of the PS block of a PS-b-PI diblock does decrease as percent of heptane in the system is increased. Unfortunately, the DSC signal for the PS block becomes smaller and smaller as more and more heptane is added. This made it difficult to distinguish the PS T_g in systems with more than 40% heptane. While it is not possible to directly measure the T_g of the micellar core in dilute solutions, it is seen that the PS T_g is significantly depressed from its bulk value. In addition to not being able to directly measure the T_g, it is not known what percentage of heptane is in the PS domains versus the PI domains.

7. Micelle Morphologies

When designing a new diblock for micelle applications, it is important to know what molecular weight of each block is needed to get a specific morphology. In other words, it is important to understand the stability regions of spherical, cylindrical, and lamellar micelles. While much work has been done in this area for SWMS,[65,66] melts and blends of diblocks and homopolymers,[13,67] and triblocks,[68-70] only a limited amount of work has been done for dilute systems of diblocks. Studies on dilute solutions of diblocks include a phase diagram for the poly(1,2-butadiene-b-ethlene oxide) in water system for two different degrees of polymerization of PB and several different PEO molecular weights.[36] However, the complex interaction of PEO with water makes it difficult to transfer these results to other systems. This is because hydrogen bonding can act to stabilize the micelles in such a specific fashion which is not possible in other systems. As such the stability of polystyrene-b-polyisoprene micelles has

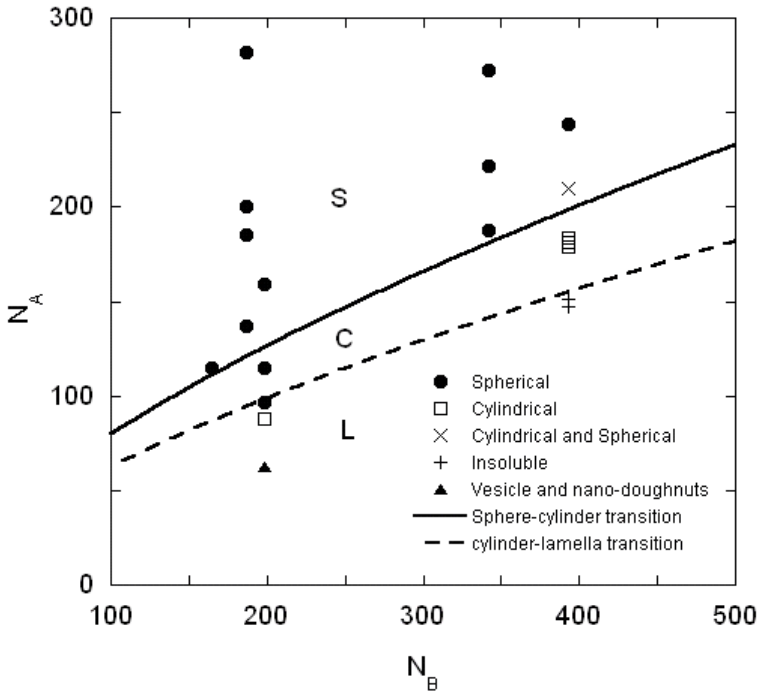

Figure 19. Observed morphologies of PS-b-PI micelles in dilute heptane solutions as a function of the degree of polymerization of both blocks. The solid and dashed curves are respectively the calculated spherical-cylindrical (eq 47) and cylindrical lamella (eq 48) boundaries.

been studied and compared with the theoretical model. **Figure 19** Shows the observed morphologies for all diblock samples studied, as well as the theoretically calculated morphological boundaries. As seen in the figure, when the soluble block size is reduced, the micelles change morphology from spherical to cylindrical micelles and eventually to vesicles.

In addition to just the major micelles morphologies, one can distinguish between two theoretical models of micelles: crew-cut[20] and star-like.[71] In crew cut micelles (Figure 2B) the corona thickness is smaller than the core diameter (H<R), while star-like micelles (Figure 2A) are the opposite case in which the corona thickness is larger than the core radius (H>R). It is widely believed that the transition to from spherical to cylindrical micelles occurs near the boundary of the crew-cut and star-like regimes,[72] however recently developed theory has predicted that the transition happens well within the crew-cut regime, i.e. when the corona is thinner than the core radius.[43] Therefore, whether the transition between the morphologies happens in the crew-cut or star-like regime needs to be experimentally determined.

7.1 Spherical Micelles

There has been a significant amount of work on the micelle structure for different types of block copolymer[37,73-75] and block polyelectrolytes.[40,41] While these studies have advanced the understanding of polymer micelles, they have mostly focused on the effect of the insoluble block. This is understandable since the size of the insoluble block has a much larger effect than that of the soluble block. The lack of experimental data on the effect of the soluble block makes it difficult to develop comprehensive theoretical models. Further more, the few studies that have looked at the effect of the soluble block were done in systems that

are complicated by charged blocks or solvent mixtures which require more complex theoretical models to explain.

As was discussed in Section 3, changing the size of the two blocks changes the balance of the free energy, which is the sum of three separate free energies, the free energy of the core, corona, and surface. This in turn changes the CMC, the average number of diblocks in a spherical micelle, i.e. the aggregation number (Q), and the micelle size, i.e. the hydrodynamic radius (R_h).

7.1.1 Critical Micelle Concentration

Spherical micelles appear in solution when the polymer concentration exceeds the so-called critical micelle concentration (CMC). The CMC is specified by the following conditions: (i) the chemical potential μ_0 of a free copolymer (unimer) in solution coincides with the chemical potential μ of copolymer molecule in the equilibrium micelle; (ii) when the translation entropy of micelles is neglected, the chemical potential μ is equal to the free energy per molecule, $\mu=F_3(Q)$ where $F_3(Q)$ is the free energy per molecule in a spherical micelle with aggregation number Q. Assuming that a unimer constitutes a spherical globule of collapsed block B and swollen block A, we find

$$\mu_0 = kT\ln(c) + F_3(Q=1) \qquad (54)$$

where ln(c) is the translational entropy of unimer in solution with concentration c. Then the CMC for spherical micelles is determined as

$$\ln(c_{CMC}) = \left[F_3(Q) - F_3(Q=1)\right]/kT \qquad (55)$$

Unlike in micelles where the insoluble block is stretched, in unimer the collapsed block is compressed with respect to its Gaussian size. The corresponding deformation free energy of the insoluble block in the core of a unimer can be written as

$$F_{B0} / kT \cong a_B^2 N_B p_B / R_{B0}^2 \cong p_B N_B^{1/3} \varphi^{2/3} \qquad (56)$$

The free energy of the swollen soluble block is composed of only a single blob and as such $F_{A0} / kT \cong 1$. Therefore the leading contribution to the free energy of a unimer in solution, $F_3(Q=1)$, is due to the surface free energy F_{s0} as long as $F_{B0} << F_{s0}$. This then means that the CMC can be written as

$$\ln(c_{CMC}) \approx \left[F_3(Q) - F_{s0}\right] / kT \qquad (57)$$

Using equation 10 for F_{s0}

$$\ln(c_{CMC}) \approx F_3(Q) / kT - (36\pi)^{1/3} \gamma \left(\frac{N_B}{\varphi}\right)^{2/3} \qquad (58)$$

As seen from equation 58, both polymer and SMWS micelles exhibit a CMC. However, since N_B for polymer micelles is much larger, the CMC for polymer micelles is going to be much lower than for SMWS micelles. In addition, unlike small molecular weight micelles which go from micelles to unimers over a narrow concentration range, polymer micelles often have a broad concentration range over which they go from micelles to unimers caused by the polydispersity of N_B.[74] The longer the insoluble block the larger the drive for the diblock to form micelles, and thus the lower the CMC.[49,50] Meaning that in the CMC region diblocks with longer insoluble blocks have started to form micelles while as those with shorter insoluble blocks still exist as unimers in solution. As seen in equations 57 and 58, the CMC is directly related to temperature. Further more, as will be discussed in more detail in section 8.1 changes in temperature can also affect γ. This means that as the temperature

changes, the CMC also changes. The temperature when micelles form (at a constant concentration) is called CMT.

Since the aggregation number changes with concentration as diblocks begin to form micelles, it is impossible to extrapolate the scattering intensity to zero concentration. Thus, only an apparent aggregation number can be measured in the CMC region.[73] The variation in the apparent aggregation number with concentration for two different polymer samples is shown in **Figure 20.** To determine the CMC from these plots, the classical definition of the CMC: the concentration at which micelles are first detected, i.e. when the aggregation number is higher than 1, is used to determine our CMC values. Since the intensity of light scattered is proportional to the concentration, very low CMCs are difficult to measure. For samples 39-15 and 39-26 it was only possible to measure the initial decrease in the aggregation number. This made it necessary to extrapolate the change in aggregation number with concentration in order to obtain the CMC. Since molecules with smaller soluble blocks

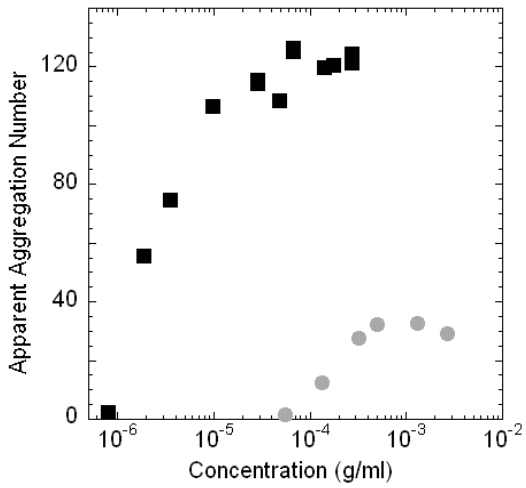

Figure 20. The change in the aggregation number with concentration for PS-b-PI 39-94 (black squares) and 19-99 (grey circles).

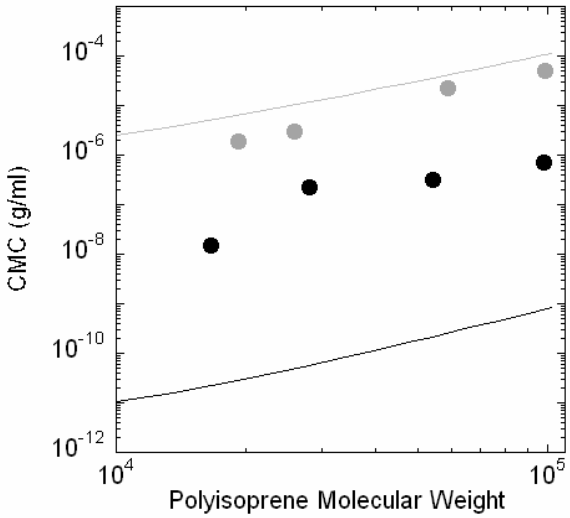

Figure 21. Plot in the variation of the CMC with the molecular weight of the PI blocks. Black and grey symbol's are for series 2 (40kDa PS) and series 3 (20kDa PS) respectively. Solid lines are results of the analytical solution (eq 58).

have a larger gain in free energy when they form micelles, the CMC should decrease as the PI block is reduced. **Figure 21** and **Table 3** show the variation in the CMC with the molecular weight of the PI block. In addition **Figure 21** shows the theoretical predictions on how the CMC (eq 58) changes with the molecular weight of the PI block. As seen in the figure, the theoretical and experimental points for series 3 (20kDa PS) are in close agreement, while theory predicts CMC's are about three orders of magnitude lower than those experimentally measured for series 2 (40kDa PS). We believe that this discrepancy is partially due to the 40kD series being out of equilibrium at 25°C as was discussed in section 6.1. Since the CMC is sensitive to temperature, being kinetically trapped at a higher temperature would elevate the CMC helping to explain some of the discrepancy between the theoretical and experimental data.

Table 3:
Experimentally Measured CMC Values

Series 1

sample	CMC	dCMC
40-12	3.07E-08	1.74E-08
40-13	2.95E-08	1.45E-08
40-17	1.26E-07	6.78E-08

Series 2

sample	CMC	dCMC
39-15	1.5E-08	6.2E-09
39-25.6	2.2E-07	1.5E-08
39-52	3.2E-07	2.2E-07
39-94	7.2E-07	1.3E-07

Series 3

sample	CMC	dCMC
20-13	1.75E-06	1.26E-07
20-14	3.27E-06	3.22E-07
20-19	1.89E-06	2.67E-07
20-26	3.08E-06	3.79E-07
20-59	2.20E-05	1.00E-06
20-99	5.07E-05	4.74E-06

Experimentally measured critical micelles concentrations (in g/ml) for micelles formed from series 1, 2, and 3 diblocks. The furthest right column (dCMC) gives the error range for each measured value.

7.1.2 Aggregation Number

As seen in **Figure 20**, well above the CMC the aggregation number levels off. In this plateau region, the apparent aggregation numbers can be extrapolated to zero concentration, thus yielding the true aggregation number. Theory predicts that the aggregation number

should increase as the size of the soluble block is decreased (eq 17). **Table 4** and **Figure 22** present the experimentally measured aggregation numbers for the polymer samples. As seen in **Figure 22**, there is excellent agreement between our data and the analytical solution. However due to the complicated nature of the analytical solution, simplified models are often used for calculating micelle parameters. The aggregation number as a function of PI molecular weight can be calculated using either the star-like or crew-cut model.[43] The star-like model is relevant when the corona thickness (H) is larger than the core radius (R). In this range the aggregation number (Q) should scale with the soluble block size as $Q \sim \left(\frac{1}{\ln(N_A)}\right)^{\frac{6}{5}}$ where N_A is the degree of polymerization of the soluble block (eq. 22). For crew cut micelles (R<H) the aggregation number depends more strongly on the soluble block size (eq. 27) and instead $Q \sim \left(\frac{1}{N_A}\right)^{\frac{18}{11}}$. As seen in **Figure 22** the star-like approximation overestimates all of the aggregation numbers but approaches the experimental data for series 2 (40kDa PS) at high PI molecular weight. This makes sense as when the soluble block length is increased the micelles should become more star-like. However, it is interesting that for high molecular weights of series 3 (20kDa PS) the star like asymptote does not appear to be as good of a fit, even though these samples are more star-

Table 4:
Aggregation Number

Series 1

sample	Agg #	dAgg #
40-12	330	7
40-13	274	9
40-17	219	10

Series 2

sample	Agg #	dAgg #
39-15	339	11
39-25.6	291	8
39-52	149	7
39-94	120	5

Series 3

sample	Agg #	dAgg #
20-13	339	41
20-14	161	2
20-19	128	4
20-26	107	3
20-59	51	2
20-99	31	1

Aggregation numbers for series 1, 2, and 3 micelles. The right most column (dAgg #) gives the error on the measured values.

like than series 2. This might be explained because data for the high molecular weights of series 3 is less reliable as the range of concentration on the plateau region is relatively narrow due to the small concentration range above the CMC and the overlap concentration (concentration when the micelles start to interact with each other). This makes the extrapolation to zero concentration less accurate. Since series 2 has CMC values several orders of magnitude lower than those for series 3, there is a larger plateau region in which to extrapolate the aggregation number. This results in more accurate aggregation values for series 2 than series 3. As seen **Figure 22,** the crew cut approximation underestimates the aggregation number for all but the smallest soluble blocks.

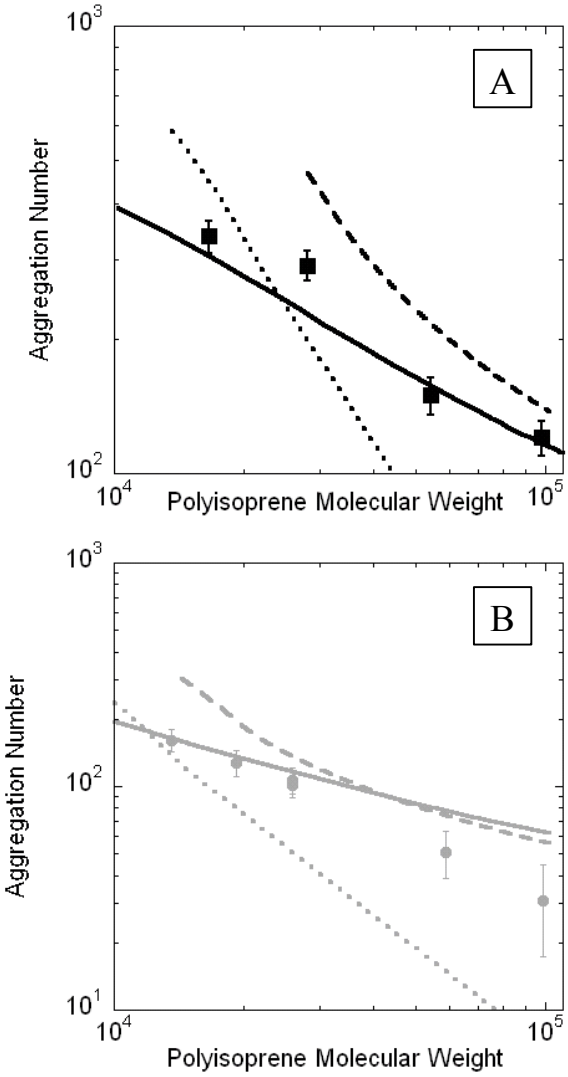

Figure 22. Plots A and B show the variation in the aggregation number with the molecular weight of the PI blocks for series 2 (40kDa PS) and series 3 (20kDa PS) respectively. The solid, dashed, and dotted lines are, respectively, the analytical solution (eq 20), theoretical star-like (eq 22), and crew cut dependence (eq 27).

7.1.3 Micelle Radius

Micelles, just like regular polymer chains and other geometric objects with variable density, can be characterized by several different radii. The most common measured size for

micelles is the hydrodynamic radius which is the apparent size of the solvated particle—i.e. the size of a hard sphere that has the same diffusion coefficient as the particle being studied. Thus the hydrodynamic radius provides information on the size of the whole micelles. In addition to knowing the total micelles size, it is important to know the size of the micelle core. Since the core is a dense object it can be measured by SANS and SAXS. **Table 5** gives the hydrodynamic and core radii measured for several polymer samples.

Table 5:
Spherical Micelle Sizes

Series 1 Sample	R_h	R_{core} SANS	R_{core} SAXS
40-12	27.0±0.5		
40-13	28.5±0.2		
40-17	29.1±0.4		
Series 2 Sample	**R_h**	**R_{core} SANS**	**R_{core} SAXS**
39-15	31.9±0.6		
39-25.6	36.3±0.3	18.6	16.9
39-52	44.7±0.2	15.4	
39-94	54.2±0.5	15.7	13.5
Series 3 Sample	**R_h**	**R_{core} SANS**	**R_{core} SAXS**
20-9		12.7	
20-14	19.9±0.7	10.8	
20-19	20.2±0.3	10.2	
20-26	23.4±0.3	9.5	9.1
20-59	31.6±0.2	8.4	
20-99	38.6±0.3	7.6	7.0

Hydrodynamic and core radius of series 1, 2, and 3 micelles. R_h and SAXS values were measured in n-heptane, while SANS data is for d-heptane. All sizes are in nm.

7.1.3.1 Hydrodynamic Radius

Through use of dynamic light scattering we are able to measure the hydrodynamic radius (R_h) of our micelles. Since polymer micelles are not completely dense objects, solvent drains through the polymer on the scale of the last blob of the corona, to take this into account a small correction to the total radius is needed to calculate R_h. It can be calculated as $R_h = R_{total} - C\xi_{last}$ where R_{total} is the sum of the core radius and corona thickness, C is a numerical coefficient on the order of unity, and $\xi_{last} = \frac{R_{total}}{\sqrt{Q}} =$ the size of the last corona blob

where Q is the aggregation number.[43] The total radius is the sum of two sizes: the radius of the core and the thickness of the corona both of which can change. As seen previously when the molecular weight of the soluble block is increased, the aggregation number decreases. This means that if the density inside the core remains constant, that the core radius will also decrease. While the core radius decreases with the molecular weight of the soluble block, the corona thickness will increase. As seen in **Figure 23** the analytical solution and experimental data are in excellent agreement. The star-like asymptotes for R_h overestimate the experimental data but become close to the experimental data as the soluble block size increases. The crew-cut model is found to be completely irrelevant—predicting the wrong magnitude of the values and also the direction of the trend i.e. it predicts a decrease in R_h as the soluble block size is increased, instead of the increase observed from the experimental data.

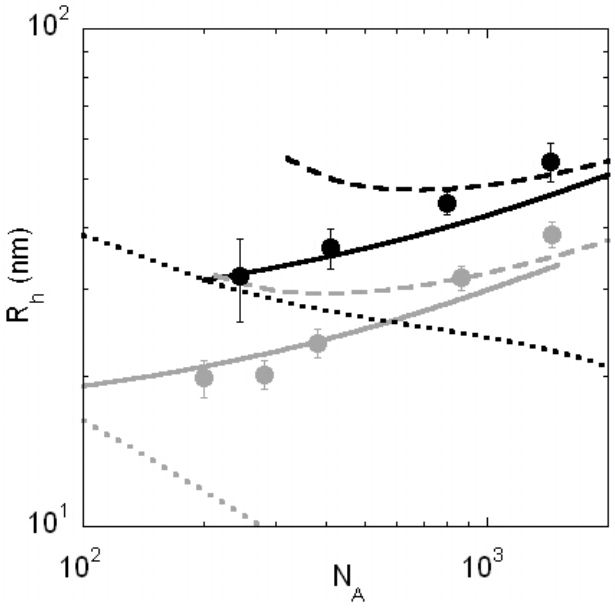

Figure 23. Plot of the hydrodynamic radius as a function of PI molecular weight. Black and grey symbol's are for 40kD and 20kD PS blocks respectively. The solid, dashed, and dotted lines are, respectively, the analytical solution (eqs 15 and 16), theoretical star-like (eqs 18 and 21), and crew cut dependence (eq 25).

7.1.3.2 Core Radius

The dimension of the micelle core and its density (next section) are important parameters to understand, especially if the micelles are to be loaded with drugs or other cargo. Tuzar *et*

al. compared theoretical R_g based on models with swollen and non swollen cores of several polystyrene-poly(methacrylic acid) block copolymer micelles with the experimentally measured R_g for the same samples. They found that for some samples the non-swollen core model was closer to the experimental value and for other samples the swollen core model was closer.[37] This possibly indicates that the size of the core was changing between samples; however without direct measurements of the core size no concrete conclusion could be drawn.

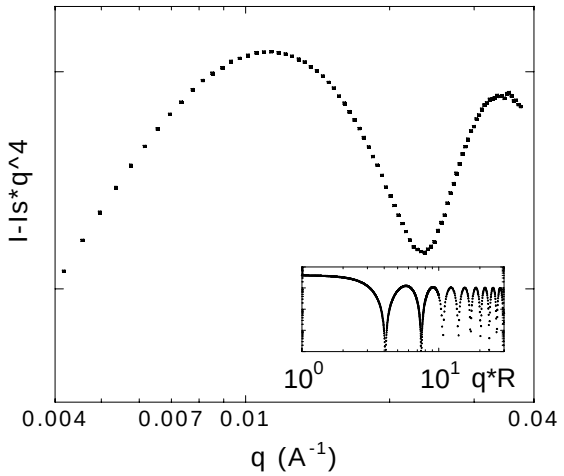

Figure 24. Porod Plot of SANS data for spherical PS-b-PI diblock polymer micelle sample 39-26. The First minimum and second maximum are located at 0.024 and 0.034 A^{-1} respectively, corresponding to a core radius of 18.6nm. The insert shows the form factor of a sphere multiplied by q^4 ($P(q)*q^4$) plotted as a function of qR.

The form factor of a sphere is

$$P(q) = \left[3 \frac{\sin(qR) - (qR)\cos(qR)}{(qR)^3} \right]^2$$

Which when plotted as a function of q, gives distinct minima and maxima, which decay as q^4. However if the form factor is multiplied by q^4 the decay no longer takes place, just the spacing between the minima and maxima decreases (see insert in Figure 24). Thus by looking at the location of the minima and maxima in q space, one can determine the

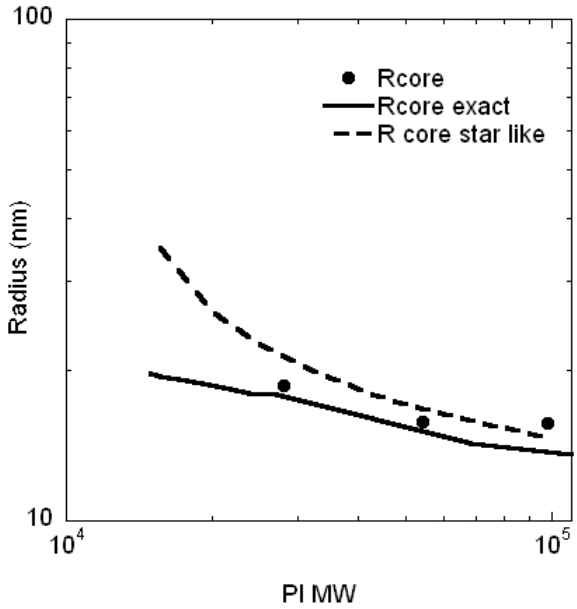

Figure 25. The variation in the core radius, as measured from SANS, with the molecular weight of the polyisoprene block. The solid curve is the predicted behavior based on the analytical solution (eq 15). The dashed curve is the star like model (eq 18).

radius of the core.

SANS experiments were performed to determine the size the micelle core for three samples with a 40K PS block and PI blocks of 26K, 52K and 94K. Due to the incoherent scattering of hydrogen, deuterated solvent must be used for SANS experiments. A Porod plot for a spherical PS-b-PI diblock polymer micelle in d-heptane is shown in **Figure 24.** From this plot it is seen that the maximums are not happening at a constant height as they should be based on the theoretical form factor. However, even with this deviation, the radius of the core can be determined from the location of the minimums and maximums. **Figure 25** shows the measured variation in the core radius with the molecular weight of the PI block. Good agreement is seen between the experimental data and both the star like and analytically predicted radii for series 2. Similar experiments were done for micelles formed from series 3 diblocks. As seen in **Figure 26**, the higher order minimums and maximums are much harder to locate for the series 3 micelles than for series 2. This is most likely due to their location being smeared out as a result of a polydispersity in the micelle size. It is also possible that the combination of the micelles being in a more dynamic equilibrium (i.e. unimer exchange happening more frequently) and the relatively low aggregation numbers seen for series 3 micelles is causing enough variation in micelle size that the locations of the minimums and maximums are

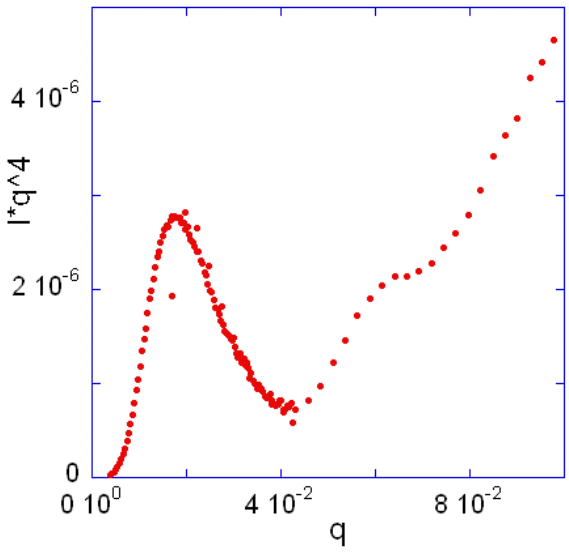

Figure 26. Porod Plot of SANS data for a spherical PS-b-PI diblock polymer micelle sample 19-19. The location of the second maximum is much harder to determine than that seen in **Figure 24**.

getting smeared out. When the core radius is plotted as a function of PI molecular weight, as is the case with the previous series, the core radius decreases as the PI molecular weight increases (**Figure 27).**

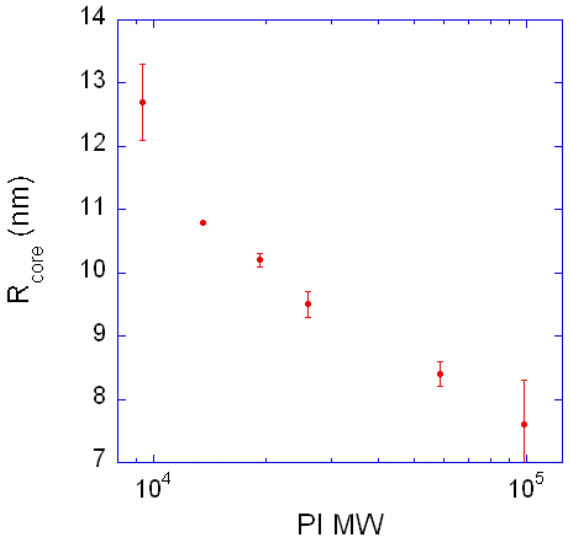

Figure 27. The variation in the core radius, as measured from SANS, with the molecular weight of the polyisoprene block form series 3 micelles having a PS block of 19kDa.

7.1.4 Core Density

Most of the work that has been done on micellization theory assumes that the polymer concentration in the core of the micelle is only controlled by the monomer-solvent interactions within the core and therefore depends only on the solvent quality for the core block and is independent of the micelle shape and the molecular weight of both blocks.[14,43] A change in the interactions affect not only the density of the core but also the size and shape the micelle will adopt. It can also be very important in determining if the observed micelles are equilibrium structures. This is because solvent in the core can act as a plasticizer and depress the T_g of the core block.

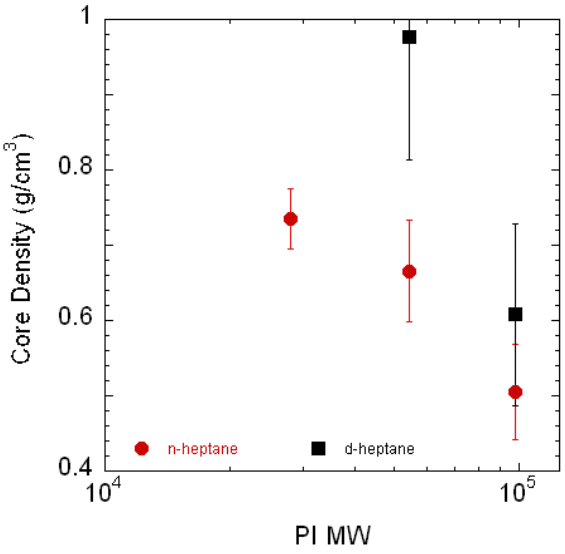

Figure 28. Plot of the variation in the micelle core density with molecular weight of the soluble block for series 2 micelles (PS block of 39kDa). The square and circle data points are calculated using the aggregation number measured in d-heptane and n-heptane respectively.

Since the aggregation number gives the number of diblocks forming a micelle and the mass of the polystyrene block is known, it is possible to calculate the mass of the micelles core. From the measurements of the core radius, the volume of the core can easily be calculated if a spherical geometry is assumed. Thus by combining measurements of the aggregation number and core radius, the density of the micelle core can be determined. **Figure 28** shows the variation in the core density with the molecular weight of the soluble block for the series 2 micelles. In contradiction with theory, the core density is changing with the size of the soluble block. In addition, it was thought that the change from n-heptane to d-heptane might be having an effect due to the small difference in solvent quality. When the aggregation number was measured from two of the samples in d-heptane, it was found to increase some leading to higher densities, however, the density still was found to change with the PI molecular weight. It was proposed that the observed variation might just be an artifact due to lack of micelle equilibration. As such, the experiment was repeated on series 3 micelles, which are in equilibrium at 25°C. **Figure 29** shows that again the density was found to depend on the MW of the PI blocks, in a similar fashion as that seen for series 2. However, when **Figures 24 and 26** are compared, it is readily seen that the scattering curves for series 3 do not exhibit the expected behavior (i.e. the intensity increases at higher q rather

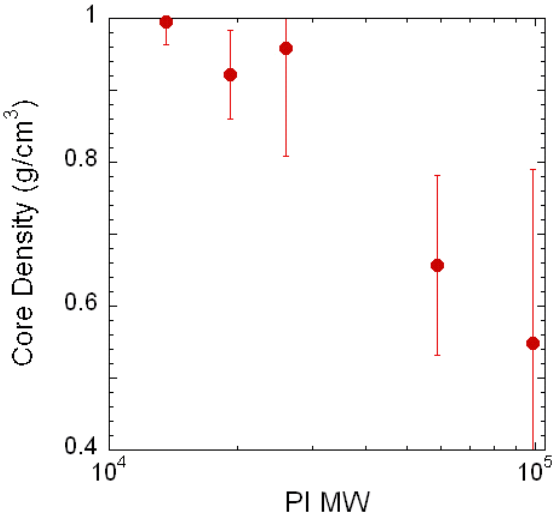

Figure 29. Plot of the variation in the micelle core density with molecular weight of the soluble block for series 3 micelles (PS block of 19kDa).

than leveling off). In addition, it is possible that the core is not spherical, and may be more disc-like. As such, further experiments are needed to accurately determine the core density.

7.2 Cylindrical Micelles

Obtaining and understanding cylindrical polymer micelles has been the subject of much work in recent years. Cylindrical micelles present many interesting possible uses such as templates, drug delivery systems, nanowires, viscosity modifiers, as a possible alternative to electrospinning, and in oil field applications.[76,77] Another area of interest in cylindrical polymer micelles is that, due to their high molecular weight, small concentrations of them can vastly change solution properties.[22]

7.2.1 Length

For cylindrical micelles it is important to study its length, which drastically changes the rheological properties. Theory predicts that the length should scale as the square root of the concentration, and while this has been verified for some SMWS systems,[78] it has not been studied for cylindrical polymer micelles. Through AFM measurements we are able to see the contour of the cylindrical micelles. With use of custom software we are able to measure the contour length of the cylindrical micelles. Initial results show the polymer micelle length to be independent of

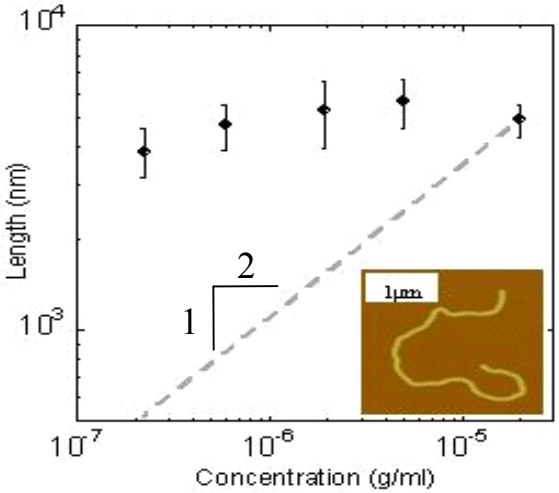

Figure 30. In contradiction to the theoretically predicted growth (dashed line), we saw practically no variations in the length of cylindrical micelles formed from sample 40-10 with concentration. Whether these results are real, or just an effect of the system being out of equilibrium needs to be further studied.

concentration **Figure 30,** however further measurements are needed in order to determine if the cylindrical micelles observed are in equilibrium.

7.2.2 Aggregation Number per Unit Length

Just like in spherical micelles, the aggregation number of cylindrical micelles is an important parameter to know. However, due to the large length differences observed in samples of wormlike micelles, the total aggregation number is less important than the aggregation per unit length. Unlike most imaging techniques that only provide 2-D images, atomic force microscopy (AFM), has the added benefit of being a 3-D technique. This not only allows for visualization of the entire micelle, yielding lengths and widths of the micelles, but also allows for the determination of the thickness of the micelles, enabling calculations of the volume the micelles occupy. To do this properly, one must take into account the well-known issue that AFM tips have a finite radius causing a broadening of the

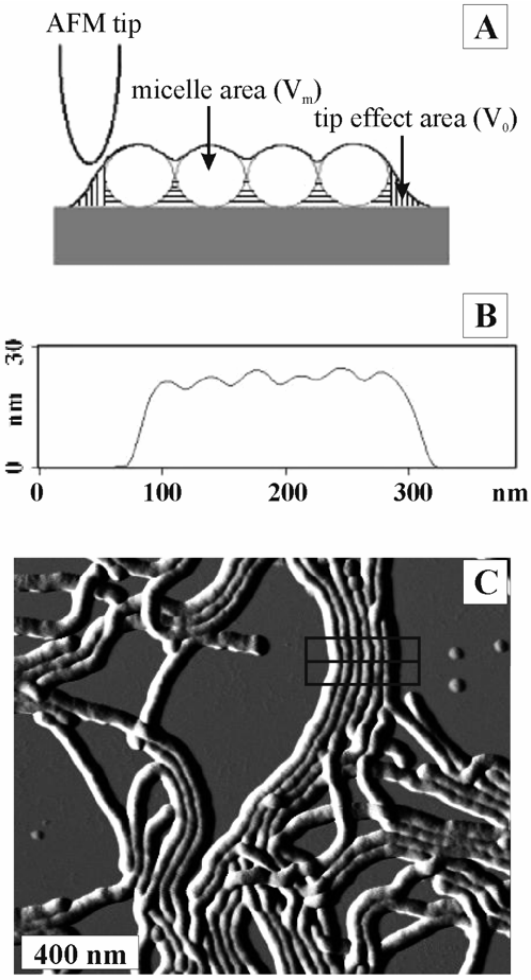

Figure 31. **Image A** is a cartoon image of tip broadening in AFM images while scanning across nanoscopic cylinders lying parallel to one another. The areas denoted with vertical stripes are areas added by the tip, which can be eliminated through our analysis. Depending on the tip shape, this area can be up to 80% of the micellar area. The areas denoted with horizontal stripes indicate where possible voids might exist. These voids are not eliminated during analysis but are less than 15% of the micellar volume. **Image B** is a cross-sectional profile along the line in **image C**, showing actual broadening of cylindrical micelles by the AFM tip. Image C is an AFM amplitude image of 40-10 micelles adsorbed from heptane at T = 60 °C. The box shows the subsection area in which the volume of six parallel micelles was calculated.

features.[79-82] This effect is shown in **Figure 31**. To correctly calculate the actual cross-sectional area, the contribution from the AFM tips needs to be evaluated. This was done by taking images of multiple micelles lying side-by-side, as seen in **Figures 31 B and C**. By plotting the cross-sectional area versus the number of parallel micelles, one can obtain the cross-sectional area for a single micelle from the slope and the cross-sectional area added by the tip from the intercept, as seen in **Figure 32**. Once the cross-sectional area had been found, multiplying by the bulk density of the diblocks $\rho = 0.98$ g/cm^3 yields the linear density of the micelle. The aggregation number per unit length was then calculated by dividing the linear density by the molecular weight of the diblock. It was found by AFM that at a temperature of 40 °C the wormlike micelles have an aggregation number of 9.6 ± 0.5 nm^{-1}. Since AFM is a surface technique it is not able to probe voids that might exist between the micelles themselves, as illustrated in **Figure 31 A.** It is possible that the polyisoprene in the micelles is able to flow slightly, filling in the voids between the micelles. This would help to explain why the heights are smaller than the diameters, as seen in **Table 6**. However, if by some chance there are voids between the micelles, the empty space would be

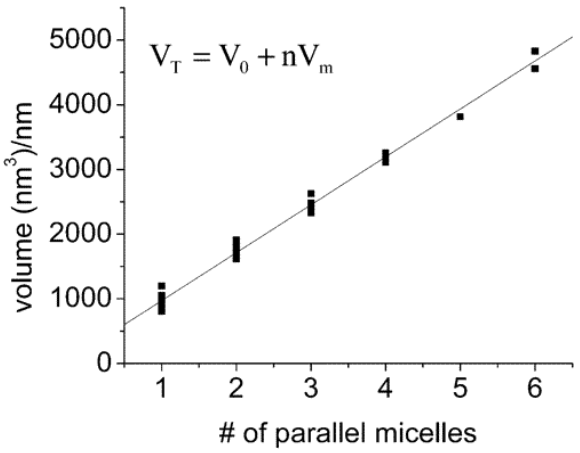

Figure 32. Plot of the total volume per nanometer (V_T) vs the number of parallel micelles (n) for 40-10 diblock adsorbed from heptane at $T = 60$ °C. The intercept gives the volume added by the tip (V_0), and the slope gives the volume per unit length for an individual micelle (V_m).

Table 6:
Cylindrical Micelle Heights and Diameters

Temperature (°C)	Height (nm)	Diameter (nm)
23	27± 2	33 ±3
40	26± 2	30 ±3
60	22 ±1	33± 3

Average heights and diameters of wormlike micelles as measured by AFM.

counted as polymer volume, resulting in a larger aggregation number, which can be estimated to be about 15% higher. A second issue to consider is that the AFM measurements were done in a dry state. In the analysis the bulk density for the polymer was used. However, if the micelles are swollen with solvent after they have been adsorbed and allowed to dry, their density could be lower than the bulk density because of vitrification of the PS core. The lower core density would also cause the calculated aggregation number per nanometer to be larger. The last issue is that AFM can actually cause sample deformation. This would cause the measured cross-sectional area to be smaller than the actual area and would result in a smaller aggregation number. Therefore, it is possible that the errors due to voids and micelle deformation might partially cancel each other.

7.2.3 Aggregation Number per unit Length by SLS

In light scattering, the scattering wavevector, q is defined as $q = \frac{4\pi n}{\lambda}\sin\left(\frac{\theta}{2}\right)$, where n is the refractive index of the solvent, λ is the wavelength of light used, and θ is the scattering angle. When qRg < 1, where Rg is the radius of gyration, the entire object can be studied by light scattering, yielding the R_g, hydrodynamic radius R_h (by dynamic light scattering), and the total weight-averaged molecular weight, MW, of the micelle, from which the aggregation number can be calculated. This is not the case for the wormlike micelles, which were found, by AFM, to be very large, causing $qR_g > 1$. Thus, only

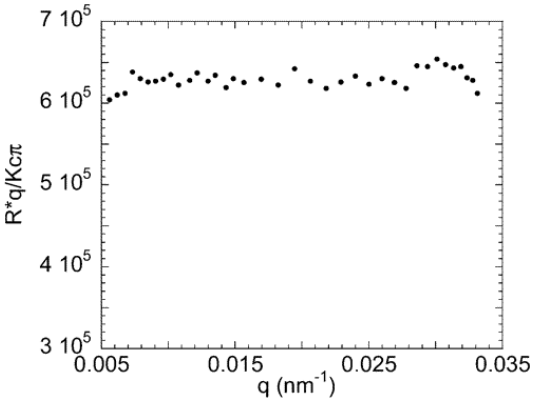

Figure 33. Representative Holtzer plot for 40-10, corresponding to a concentration of 3.5 × 10^{-5}g/mL, measured at 25 °C. The value of the plateau results in an aggregation number of 12 ± 0.2 nm^{-1}

the mass per unit length can be measured by static light scattering from the Holtzer[83] plot, in which $R_\Theta q / \pi Kc$ is plotted as a function of q, where R_Θ is the Rayleigh ratio, $K = 4\pi n^2 (dn/dc)^2 / \lambda^4 N_{AV}$ is the optical constant, N_{Av} is Avogadro's number, c is the concentration of polymer in solution, and dn/dc is the specific change in refractive index for a polymer solvent pair, which for 40-10 in heptane can be calculated[83] as 0.190. Dividing the plateau value in **Figure 33,** which is equal to the mass per unit length, by the molecular weight of the diblock gives the aggregation number per unit length. We can then compare the results from light scattering with those obtained from AFM. At a temperature of 40 °C, light scattering gives an aggregation number of 10.5 ± 0.3 nm^{-1}, which is in good agreement with the AFM value of 9.6 ± 0.5 nm^{-1}. As seen in **Figure 34,** for both the AFM and light scattering data it is clear that as the temperature is raised above 40 °C, the aggregation number per unit length decreases. This decrease is to be expected, since in this study heptane was used as the poor solvent for polystyrene: as the temperature is raised, heptane becomes a better solvent, lowering the surface energy and allowing for smaller aggregation numbers. One would expect the aggregation number per unit length to increase at temperatures below 40 °C; however, it appears to level off and not increase further. As such, samples below 40 °C might not be in true equilibrium (possibly due to freezing of the swollen polymer core). Preliminary studies indicate above 45 °C equilibration appears to take place within a couple of hours; however, at lower temperatures the equilibration time is much longer. The equilibration of micellar solutions needs to be studied in greater detail.

7.3 Vesicles

Typically, vesicles are observed in aqueous block-copolymer systems, featuring hydrophilic corona block and hydrophobic core block. Existence of vesicles in non-aqueous block-copolymer systems has not been evidenced until recently.[45,84,85] The rare observation of vesicles was attributed to weaker segregation of hydrocarbon cores in non-aqueous (organic) solvents. In other words, the lower surface energy favors higher curvature objects such as spheres; while higher surface energy in aqueous block-copolymer systems promotes formation of lower curvature objects such as vesicles.

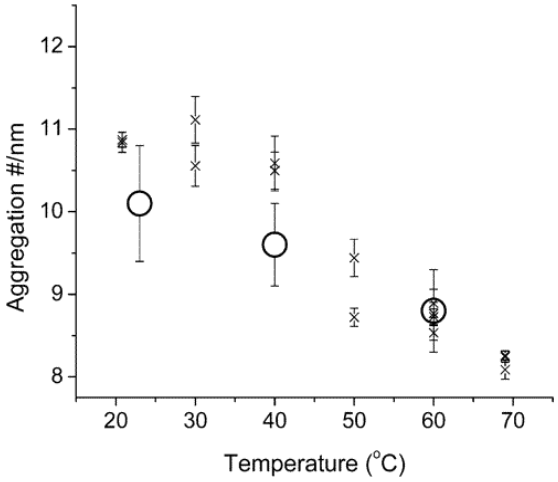

Figure 34. Variation of aggregation number per nanometer as a function of temperature. Circles and ×'s are AFM results and light scattering results, respectively.

Initially samples that were expected to have a vesicle morphology were all found to be insoluble (samples 39-8.9 and 39-9.2). When a smaller PS block was used, it was found that sample 21-4 exhibits a vesicle morphology in heptane. As seen in **Figure 35** the AFM image shows the expected morphology of vesicles that have collapsed onto a solid substrate to form a disk-like structure with the characteristic wrinkles and wedge-like cuts expected when a hollow object collapses onto a surface. When

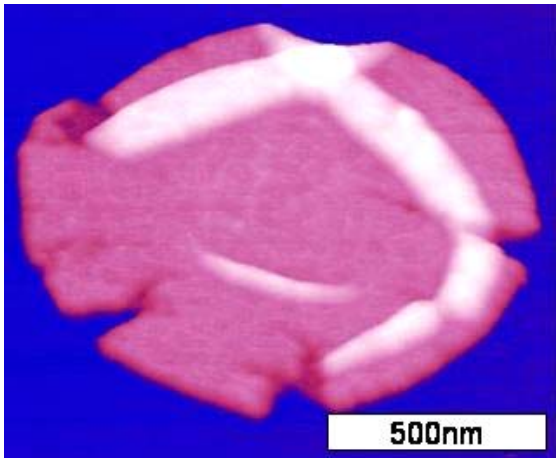

Figure 35. AFM 3-D height image of sample 21-4 after having been dissolved in heptane at 25°C. The AFM image shows the expected morphology of vesicles that have collapsed onto a solid substrate to form a disk-like structure with the characteristic wrinkles and wedge-like cuts.

left standing, most of the micelles in sample 21-4 precipitate out of solution; however a quick stirring re-suspends them.

7.4 Discrepancies Between Theoretical and Experimental Data

From the phase diagram (**Figure 19**), it is seen that the calculated boundaries hold well for the 40kD samples, where as they are off for the 20kD samples. If the experimental observed spherical-cylindrical boundary is fit by a modified version of eq 48 where all of the prefactors are treated together as one variable and the only other variable is the exponent of N_B (i.e. $N_A \approx XN_B^Y$) we find that the a value of Y of 1.02 gives the best fit. This is shown in **Figure 36.** If we look at the solvent quality independent equation for the phase boundary[43]

$$N_A^{sc} \approx \left(\frac{21\pi^2 N_B^2}{20 p_B \varphi^3}\right)^{(1+2\nu)/11\nu} \frac{\gamma^{(7\nu-2)/11\nu}}{\hat{C}_H}\left(\frac{a_B}{a_A}\right)^{1/\nu}\left(\frac{\hat{C}_F}{2\nu}\right)^{(1-9\nu)/11\nu}$$

we find that the only way to have N_A linearly depend on N_B is if the unrealistic value of $\nu = \frac{2}{7}$ is used. If we take into account that the 40kDa samples are not in equilibrium at 25°C, the problem becomes even worse. At temperatures above 45°C, sample 21-6 becomes spherical, this would mean that an even stronger dependence on N_B is needed.

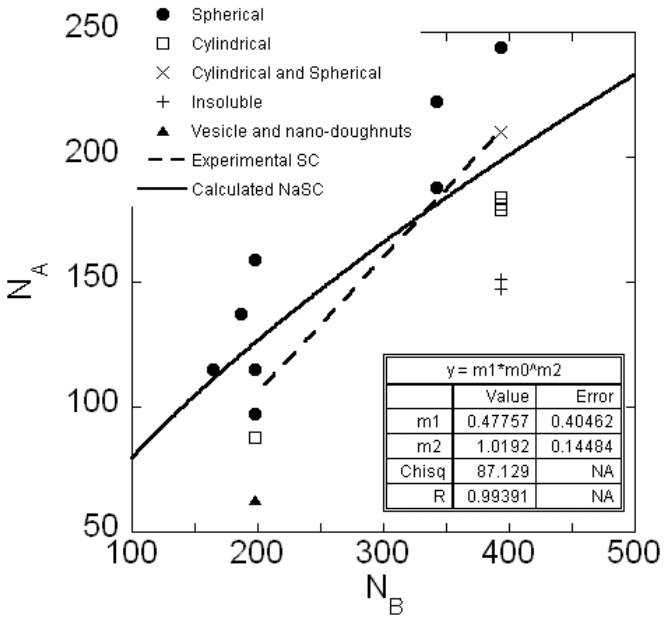

Figure 36. Phase diagram with the experimental determined spherical-cylindrical boundary fit. The best fit results in an exponent for N_B on the order of unity, i.e. $N_A = 0.5 * N_B$.

So far this comparison is based

only on three series of samples (40kDa, 39kDa, and 19kDa PS blocks), i.e. there are only three points for every boundary. In addition, two of the three points might not correspond to equilibrium. As such, more measurements need to be done to cover a large range of N_B values.

8. Morphological Transitions

Recently there has been a lot of work on changing micelle morphology. As is seen in equations 47 and 48, changes in any of the various parameters can cause the morphological boundaries to shift. As was discussed previously in section 7.1, morphological transitions can be brought about by changing the size of the soluble block while keeping the insoluble block a constant size has been experimentally verified.[22,38,60,87,88] In addition to changing the ratio of the blocks, it has been previously shown that morphological transitions take place with the addition of core-like (miscible polymer) homopolymer,[89] and changing γ and ν through the addition of co-solvent.[84,90-92] This is demonstrated experimentally by looking at the morphologies found

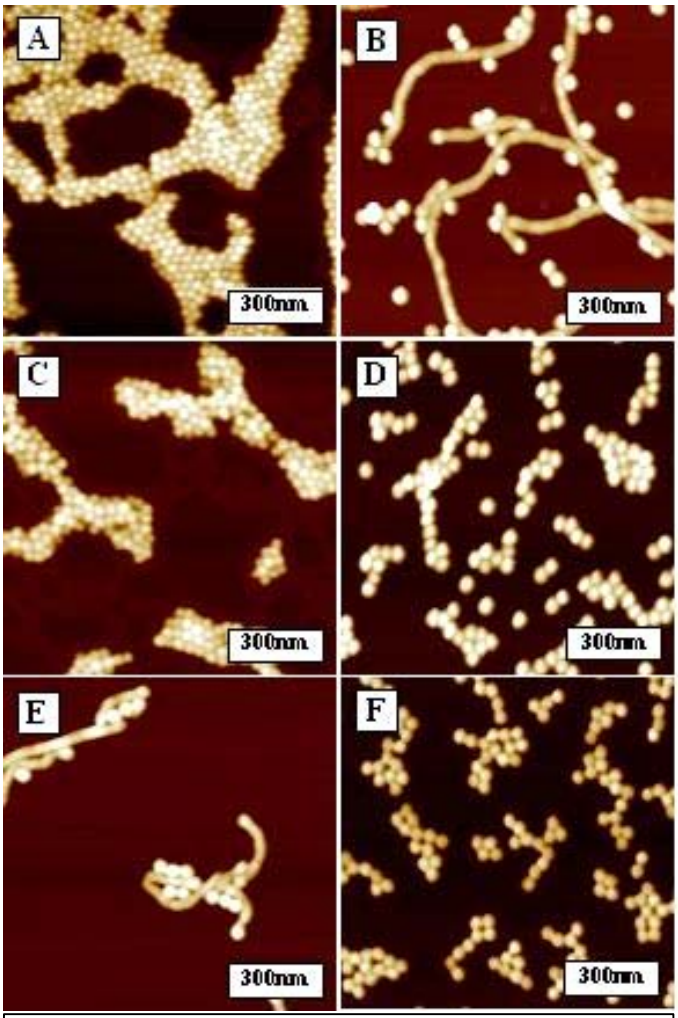

Figure 37 AFM images of **A)** Spherical micelles of 40-12 adsorbed from heptane. **B)** Coexistence of spherical and cylindrical micelles of 40-12 adsorbed from decane. **C)** Spherical micelles of 40-13 adsorbed from heptane. **D)** Spherical micelles of 40-13 adsorbed from decane. **E)** Coexistence of cylindrical and spherical micelles of 40-13 adsorbed from tetradecane. **F)** Spherical micelles of 40-17 adsorbed from tetradecane.

when diblock samples are dissolved in solvents of differing solvent quality. As the PI/PS ratio was raised, the diblocks were found to exist almost exclusively as spherical micelles in heptane, but by lowering the solvent quality for the PS block, spherical and cylindrical micelles were found to coexist once again. 40-12 was found to exist exclusively as spherical micelles when adsorbed from heptane as seen in **Figure 35 A**. When 40-12 was adsorbed from decane as seen in **Figure 35 B**, cylindrical micelles were found to coexist with spherical micelles. 40-13 also was found to exist almost exclusively as spherical micelles when adsorbed from heptane and decane, as seen in **Figures 35 C** and **D**. When 40-13 was adsorbed from tetradecane, cylindrical micelles were once again formed, as seen in **Figure 35 E**. 40-17 was found to exist only as spherical micelles in heptane, decane, and tetradecane, as seen in **Figure 35 F**.

8.1 Reversible Morphological Transitions

While the studies discussed in the previous section show that it is possible to change from one morphology to another, the only way to recover the original morphology is through the addition of more solvent or diblock. This means that when designing micelles one can know what sized blocks are needed for a given morphology; however, once the diblocks are synthesized, changing the block size is no longer possible.

Here we show that similar morphological transitions are induced by changing temperature while keeping the solvent and polymer concentration constant. AFM and light scattering data demonstrates that reversible transformations from cylindrical to spherical micelles and from vesicle to cylindrical micelles take place upon the heating and subsequent cooling of dilute solutions of polystyrene-b-polyisoprene copolymer in heptane. The

observed transitions are attributed to the temperature dependence of γ and ν. In principle this is the same as changing γ and ν through the addition of co-solvent, but it has the advantage that only external parameters are being changed.

In the studied system (PS-b-PI in heptane) changing the temperature affects the solvent quality of heptane for both the PS and PI blocks. The change in the solvent quality for PI was measured through the variation in the second virial coefficient (A_2). We carried out A_2 measurements for a PI standard with a molecular weight of 34kD. As seen in **Figure 38**, the second virial coefficient of PI in heptane increases with temperature. By fitting this data and using the relationship $\nu = 2A_2M_0^2/\left(a_A^3N_{AV}\right)$, where N_{AV} is Avogadro's number and M_0 is the molecular weight of the monomer,[43] one can calculate the variation in the excluded volume parameter with temperature as

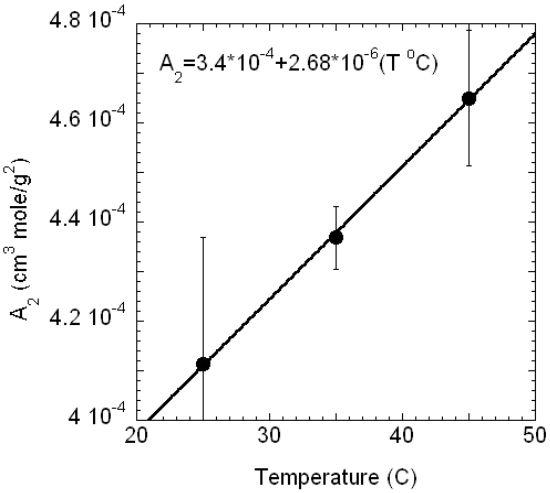

Figure 38. Temperature variation of the second virial coefficient of PI in heptane. Fitting the data results in $A_2 = 3.4 \times 10^{-4} + 2.68 \times 10^{-6}(T - 273)$ where T is the temperature in °C.

$$\nu = 2M_0^2\left(3.4\times10^{-4} + 2.68\times10^{-6}(T)\right)/\left(a_A^3N_{AV}\right) \qquad (59)$$

In addition to the change in the excluded volume, it has been previously shown that γ for polystyrene in heptane varies with temperature[50] as

$$\gamma / kT = (0.68 \pm 0.01) - (5.2 \pm 0.2) \times 10^{-3}T\,(°C) \qquad (60)$$

By using the variation in ν and γ with temperature in Equations 1 and 2, the change in the morphological boundaries with temperature can be calculated. **Figure 39** shows that as the temperature is raised from 25 to 35°C, the morphological boundaries shift to lower values

of N_A as shown by the dashed lines. This means that if a cylindrical micelle sample is near the spherical-cylindrical (S-C) boundary, it will adopt a spherical morphology when the temperature is increased. Likewise a vesicle sample near the cylindrical-vesicle (C-V) boundary will adopt a cylindrical morphology upon heating.

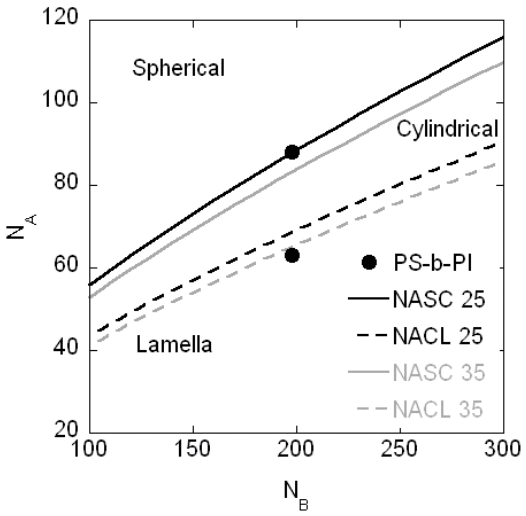

Figure 39. Phase diagram calculated for PS-b-PI in heptane showing the variation in the spherical/cylindrical (black curves) and cylindrical/lamella (gray curves) morphological boundaries with temperature. The solid lines are calculated at 25°C and the dashed lines are calculated at 35°C. The spherical points are the diblock polymer samples. The model parameters used are a_B=5.6Å, a_A=5.0 Å, p_B=1.5, p_A=1.6, =0.7, C_F=1.38, C_H=1.20 with γ and ν being calculated for each temperature.

From eqs 59 and 60 one can also calculate the relative contribution of the change in solvent quality for the corona and core blocks in the boundary shift. If temperature increases 10 deg, the excluded volume parameter of the PI corona increases by $\Delta\nu/\nu$ = 0.025, i.e., by 2.5%, while the surface energy of the PS core decreases as $\Delta\gamma/\gamma$ = -0.095, i.e., by 9.5%. Since both parameters enter eqs 1 and 2 with the same power 1/3, this causes approximately 1/3(0.025 + 0.095) × 100% ≅ 4% shift of the boundaries to lower values of N_A, wherein the surface energy of the core has a dominant contribution ~4 times larger than that of corona. It is remarkable that this shift is significantly lower than the 18% relative standard deviation (RSD) of the blocks length due to the polydispersity calculated as RSD = $\sqrt{PDI-1} \cong \sqrt{1.035-1}$ = 0.18. This strongly suggests that individual micelles include a mixture of diblocks with different molecular weights.

These predictions were confirmed for two diblocks samples. Sample 21-6 with a PS block of 21kD and a PI block of 6kD was found to be near the calculated S-C boundary and forms cylindrical micelles at 25°C (**Figure 40 A**). Since sample 21-6 is near the boundary, only a small decrease in γ and/or an increase in ν is needed to cause the cylindrical fraction of the sample to become spherical. When the sample is heated to 35°C only spherical micelles are observed (**Figure 40 B**). Upon subsequent cooling back to 25°C cylindrical micelles were once again observed (**Figure 40 C**). However the growth of cylindrical micelles appears to take a much longer time than the decay of cylindrical micelles into spherical ones. As seen in **Figure 40 C**, only a few short cylindrical micelles were observed and most of the micelles still had a spherical morphology. Keeping the sample at 25°C for a longer period of time resulted in the length and fraction of cylindrical micelles to increase as seen in **Figure 40 D and E**. By using AFM the

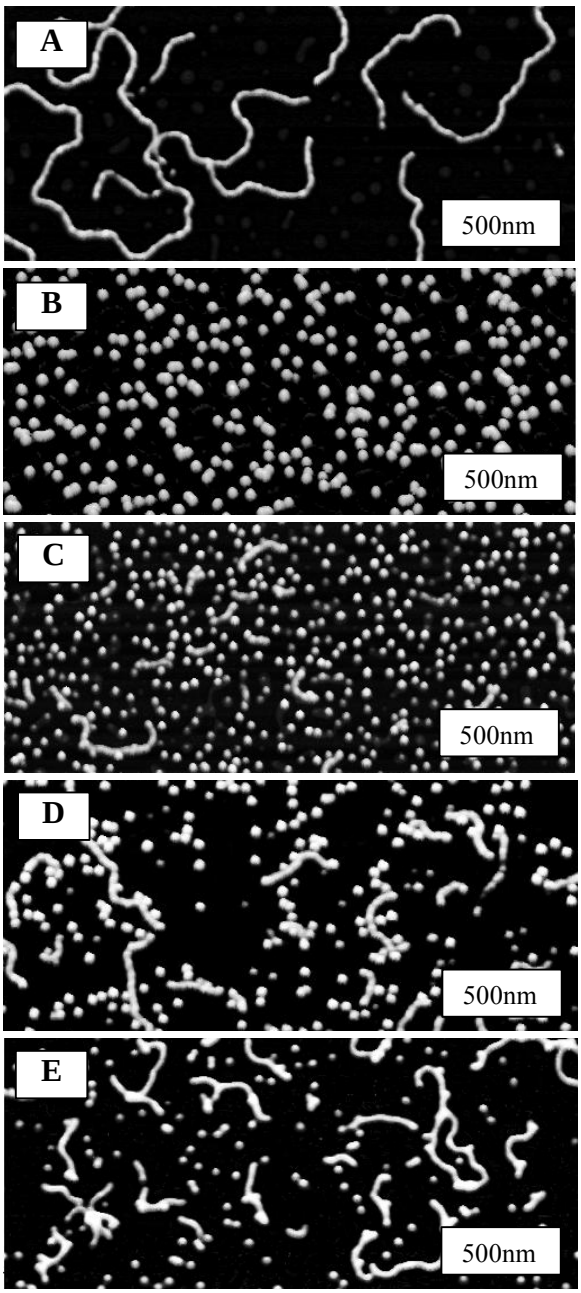

Figure 40. 2.5µm AFM scans of PS-b-PI micelles with a PS block of 21kD and a PI block of 6kD. **Image A** was taken after the sample solution had been at room temperature for 2 weeks. **Image B** was spin cast from a sample solution that had been at 35°C for 18 hours. **Images C, D, and E** were spin cast days after the sample had been cooled back to 25°C for 4, 21, and 36 days respectively.

fraction of the surface area covered by cylindrical micelles versus the total surface coverage of all micelle morphologies and the average length of cylindrical micelles can be independently measured. As seen in **Figure 41 A**, both the fraction of coverage and the length are still growing after several weeks at 25°C. It appears that the sample is slowly returning to a completely cylindrical conformation.

To make sure that the adsorption procedure and interactions with the surface are not influencing the observed morphologies, light scattering was used to confirm the morphological transition. **Figure 41 B** shows the *in-situ* decay in the average aggregation number (the number of diblocks associating to form the

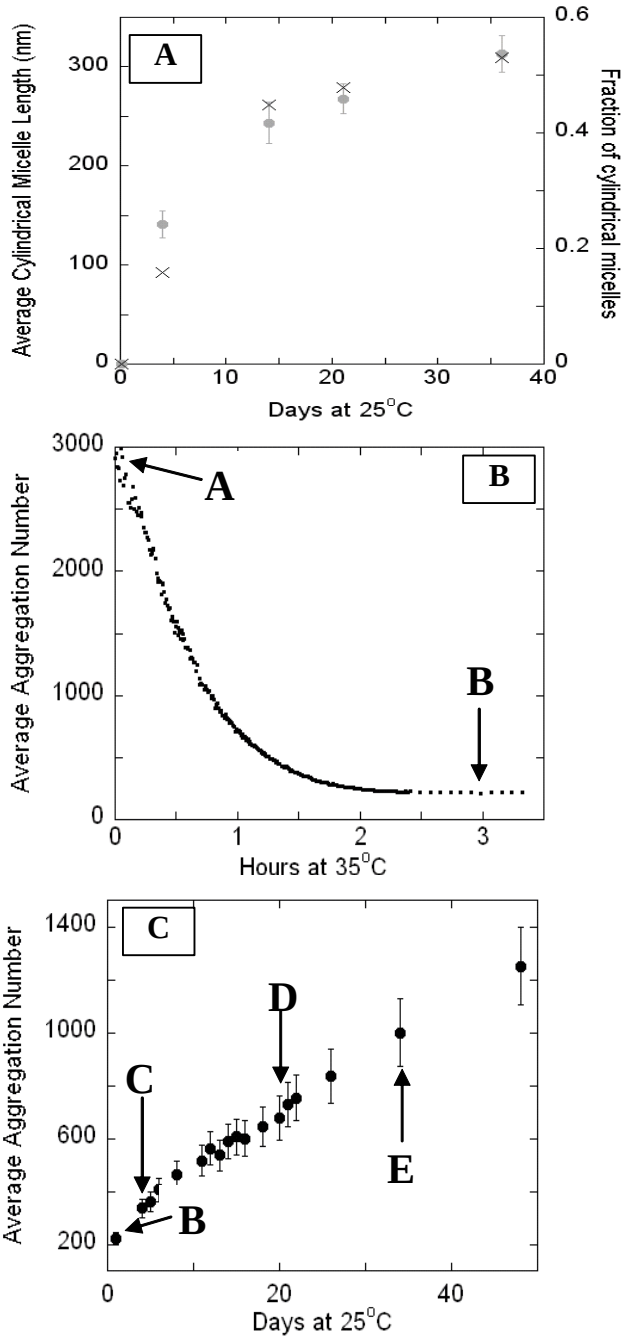

Figure 41. Plot A shows the evolution of the average cylindrical length (circles), and fraction of the micelles with a cylindrical morphology (X's) for sample 1 after cooling from 35 to 25°C. **Plots B** and **C** are evolution of the average aggregation number with time at 25 and 35°C respectively. The letter labels in **plots B** and **C** indicate the corresponding AFM images in **Figure 40.** Both plots were measured by static light scattering. For plot B the intensity was measured at a fixed angle and then converted to aggregation number. The aggregation numbers for plot C were measured using the classic Zimm Plot method.

micelle) after the solution has been heated to 35°C. As seen in the figure, the average aggregation number drops from ~3000 to 200 in a little over 2 hours. This change in the average aggregation number is consistent with the AFM images which show a change from long cylindrical micelles to small spherical ones. Light scattering was also used to follow the slow growth of cylindrical micelles. As seen in **Figure 41 C**, the average aggregation number is still increasing after the solution has been kept at 25°C for several weeks. In addition, dynamic light scattering can be used to confirm the presence of different sized species in solution after cooling back to 25°C. **Figure 42** shows that upon cooling a bimodal size distribution emerges in the CONTIN fit of dynamic light scattering data.[93] This shows that in addition to the spheres, a second species with a larger hydrodynamic diameter forms upon cooling. Based on the AFM observations, the second species is ascribed to cylindrical micelles.

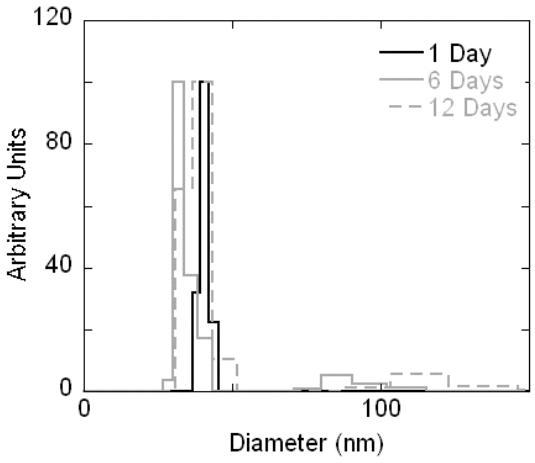

Figure 42. Plot of the Contin fit of dynamic light scattering data. The solid black data was taken after being at 25°C for ~ 1 day; the solid gray data is after ~6 days at 25°C. The dotted gray line is after ~12 days at 25°C. Upon first cooling to 25°C all micelles have a hydrodynamic diameter of ~40nm, after ~6 days at 25°C a bimodal distribution of hydrodynamic diameters is observed indicating the presence of a second larger species. After ~12 days at 25°C the peak of the second mode shifts to having a hydrodynamic diameter of ~110nm versus the ~85nm after 6 days.

Sample 21-4 with the same PS block of 21kD and a shorter PI block of 4kD was found to be near the calculated cylindrical-vesicle boundary. It was found to be comprised of mostly vesicles at room temperature, with a small fraction of toroidal micelles, small cylindrical rings having almost the same cross section as the cylindrical micelles observed in Sample 21-6 (**Figure 43 A**). The AFM image shows the expected morphology of vesicles that have

collapsed onto a solid substrate to form a disk-like structure with the characteristic wrinkles and wedge-like cuts. From the section analysis along the line in **Figure 43 B** the thin parts of the vesicle were found to be twice the thickness of the toroids which is consistent with the bilayer structure expected for vesicles. For Sample 21-4 it was necessary to heat the sample from 25 to 40°C before vesicles were no longer seen (**Figure 43 C**). It was also seen with sample 21-4 that the cylindrical micelles near the vesicle boundary appear to favor the formation of rings. This makes sense since the end caps of cylinders have a spherical geometry, as the micelles get closer to the vesicle boundary the energy cost of these spherical end-caps becomes higher. Thus it is favorable for the cylindrical micelles to either form very long cylinders or rings in order to reduce the number of end-caps.[55,94] the vesicle solution appears to be slowly returning to the original all vesicle conformation. An interesting feature of the slow growth

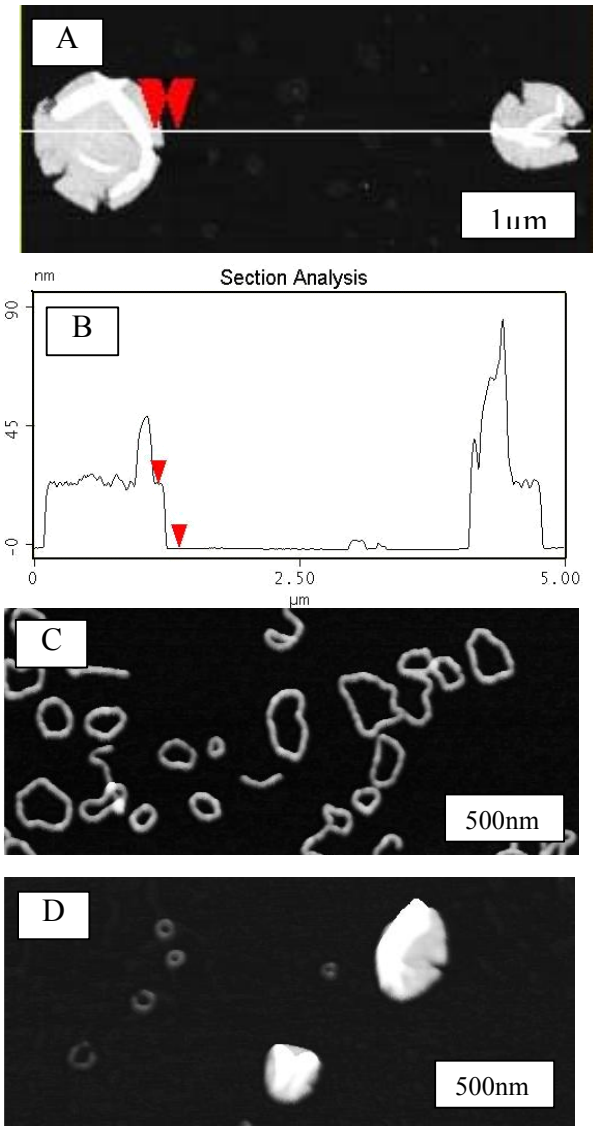

Figure 43. AFM images of sample number 2. Image A was taken after the sample had been at 25°C for 2 weeks. Figure B is the section analysis along the line in image A. The vertical distance between the two arrows is 24nm, which is approximately twice the height of the cylindrical micelles in sample 1. Image C was spin cast from a 40°C solution. Image D was taken 2 days after cooling the solution back to 25°C.

of vesicle micelles is that while vesicles are forming, larger rings and most of the vesicles appear to slowly settle out of solution at room temperature.

Similar morphological transitions were first tried with for 40-10. As discussed previously, sample 40-10 typically exists as long cylindrical micelles as seen in **Figure 44 A.** When 40-10 is heated to 85°C only spherical micelles were observed in solution **Figure 44 B.** However, upon slowly cooling back to 25°C only spherical micelles were observed. Initially it was thought that sample degradation might be taking place at such high temperatures and that was why the sample did not return to its originally morphology. To show that sample degradation was not taking place, the heptane was evaporated from the spherical micelles solution, and the dry diblock was redissolved in fresh heptane. When this was done, cylindrical micelles were once again observed **Figure 44 C**. It is believed that the reason sample 40-10 does not return to a cylindrical morphology upon cooling is that the T_g is above the morphological phase boundary. If this is the case, upon cooling the spherical micelles

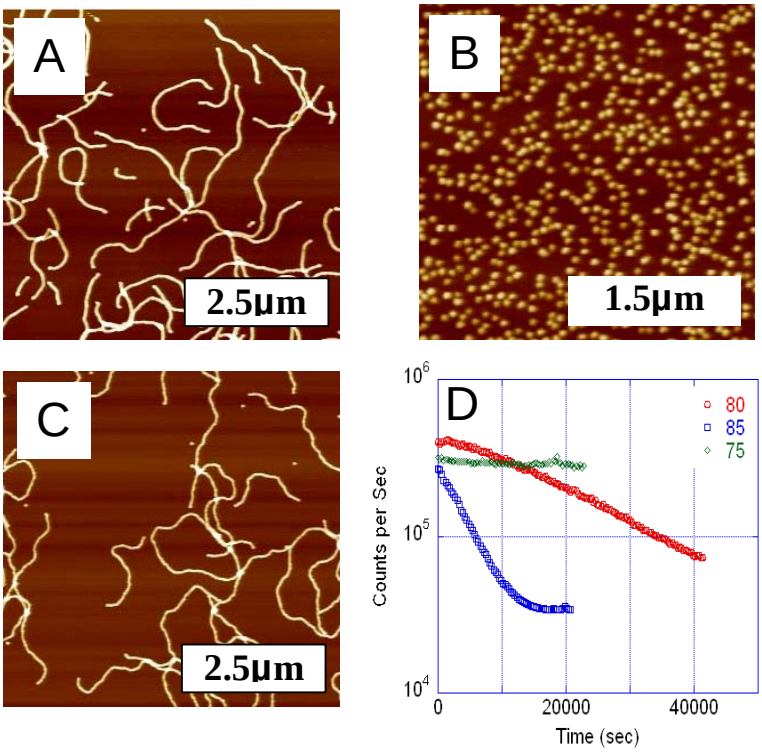

Figure 44. Sample 40-10, which forms cylindrical micelles at 25°C (A) was found to change to spherical micelles upon heating above 80°C (B). Upon cooling back to 25°C sample 40-10 retained a spherical morphology. When the heptane was evaporated and the sample was redissolved in new heptane at 60°C cylindrical micelles were once again observed (C). As seen in plot D, the morphological transition does not take place at temperatures below 75°C (green data points) and the rate of conversion from cylindrical to spherical micelles happens much faster at 85°C (blue points) than at 80°C (red points).

become trapped in a glassy state before they are cooled below the morphological boundary. Thus while a cylindrical morphology is thermodynamically favorable, the micelles are kinetically trapped in a spherical morphology. Static light scattering was used to find the temperature at which the morphological transitions start to take place. As seen in **Figure 44 D**, at temperatures below 75°C no change in the scattering intensity is observed. It is also seen that the morphological transition takes place much faster at 85°C than at 80°C.

9. Micelles as Molding Templates

Natural “self-assembled” systems have a sophisticated morphological shape control that materials synthesis and traditional fabrication technologies cannot approach. However, “self-assembly” comes at the cost of requiring highly specific materials and conditions. Unique, precise 3-dimensional molecules and self-assembled shapes abound in nature; examples include hierarchically organized organisms,[95] colloidal particles, and the viral membrane. These structures interesting shapes are largely due to noncovalent chemical interactions which can produce elegant, “evolutionarily-designed” 3-D shapes with nanometer precision. Taking a cue from nature, current researchers are using self-assembly principles to control material shape. This work has led to the development of a class of synthesis/fabrication methods that are termed “bottom-up” fabrication because the organizational framework in these materials is derived from non-covalent chemical interactions intrinsic to the materials being assembled, rather than from externally directed pattern formation. “Bottom-up” methods have found a great deal of success in controlling nanoscale shape in organic and inorganic materials.

9.1 Molding Background

“Bottom up” methods have significant limitations. Because there is little long-range organization, large-scale integration of these materials can be challenging. The chemical structures of each of the components in the assembly mixture must be carefully designed to

correctly assemble into desired morphology. Even if the chemical design of the material is sufficient for the desired assembly process to take place, factors such as temperature, solution purity, and assembly time can significantly affect the resulting morphology. These potential complications are especially pronounced for metastable structures where the desired structure may be a transient morphology.

"Top-down" lithographic technologies have made great strides toward controlling material morphology at sub-100 nm length scales. For example, using electron-beam and scanning probe lithographic methods, it is possible to fabricate structures with sub-20 nm lateral dimensions,[96-100] but these techniques are serial in nature and may have limited scalability. Other efforts have successfully demonstrated parallel fabrication of simple 3 dimensional shapes such as pyramids,[101-103] but these efforts rely on anisotropic processing conditions which are likely to limit the range of shapes to simple geometric solids which do not approach the complexity of 3-dimensional material shape afforded using self-assembled materials.

9.2 Molding Process

Here, we applied a newly developed technique to fabricate unique, nanostructured materials that closely mimic self-assembled morphological shapes with nanometer-scale fidelity using material that does not self assemble on its own. To accomplish this, we use delicate, naturally occurring self-assembled micelles as master templates for imprint lithography using specifically-designed fluoropolymers based on perfluoropolyethers (PFPEs) that can be photochemically cured at room temperature and capture the nanometer-scale shapes of these objects in a cross-linked fluoroelastomer mold.[104,105] These molds can

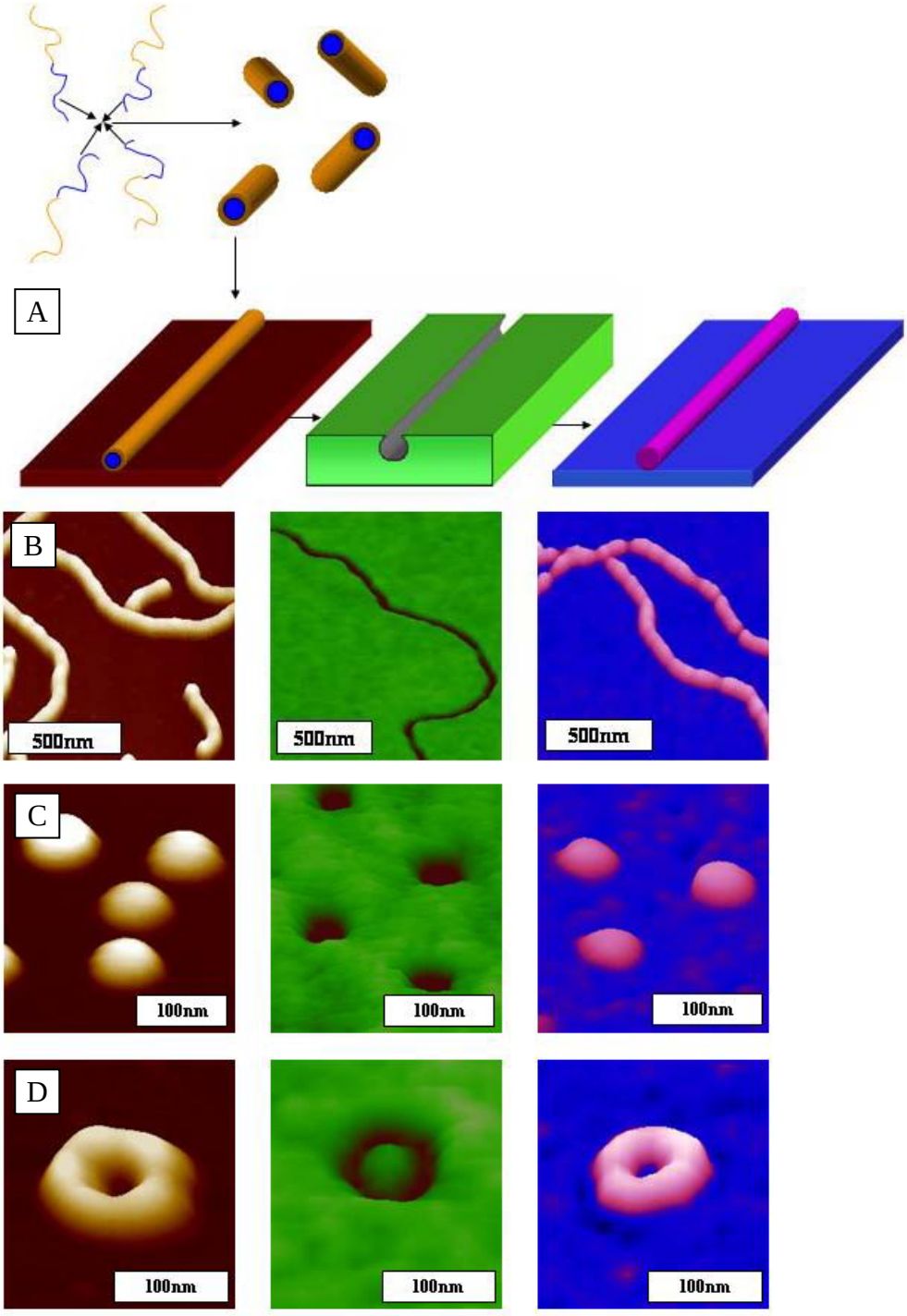

Figure 45. Row A shows a cartoon representation of the replication process. First the micelles are adsorbed onto the surface (brown/left), then a mold of the micelles is made (green/middle), followed by replicating the micellar structure (pink/right). **Rows B, C, and D** are AFM images of each step of the replication process using cylindrical, spherical, and toroidal micelles respectively. In each of these rows the left most image are PS-b-PI micelles (brown) adsorbed onto a mica surface from heptane. The middle images show the PFPE molds (green), and the right images are the replicas formed from triacrylate resin (pink)

then be used to replicate the naturally occurring shape into another material (**Figure 45**). The "self-assembled" morphologies produce patterned surfaces that are in sharp contrast to the "conventional" geometric shapes that can be obtained using traditional microlithography or soft lithography. With their excellent spreading and non-interacting characteristics with the naturally-occurring soft master templates used, we have observed excellent correspondence between the morphologies of the micelles and the corresponding embossed replicate structures. The ability to combine the fidelity and scalability of "top-down" fabrication with the sophistication of "bottom-up" assembly will allow the replication of functional self-assembled structures such as tissue surfaces and sub-cellular structures for sensing, materiel science, and medicine.

In this work, we have combined "top-down" and "bottom-up" fabrication methodologies to produce intricate, nanoscale self-assembled morphologies using the robust materials and scalable processing techniques that are typical of lithography. This requires the development of patterning techniques that are gentle enough to be compatible with non-covalently assembled structures, yet amenable to large-scale, parallel pattern formation. We have bridged this gap by performing imprint lithography with low-energy, minimally adhesive, room-temperature photocurable perfluoropolyether (PFPE) elastomers to replicate patterns found in nature ("master templates") on surfaces.[104-106] These PFPE molds can then be used to pattern replicates of a variety of materials with superior fidelity. The ability to perform "top-down" patterning of "bottom-up" self-assembled structures and other naturally-occurring materials can be demonstrated through the replication of micelles. The PFPE mold precursor is poured over the naturally-occuring master and photocured to form an impression

of the master with nanoscale fidelity. The molds are then used to replicate the self-assembled morphologies in other, more robust materials.

9.3 Molding Results

Figure 45 shows a cartoon representation as well as the actual steps of the molding and replication of self-assembled poly(styrene)-block-poly(isoprene) amphiphilic block-copolymer micelles. As was shown in section 7, these materials can exhibit a variety of interesting morphologies including spheres, cylinders, vesicles, and toroids. We created master templates from these materials by dispersing them on mica substrates from solution. PFPE molds were formed from these masters and used to replicate the self-assembled micelle morphologies into thin films of other materials. **Table 7** gives the average heights and diameters of the masters and the replicas. The small differences observed are attributed to differences in the AFM tip shape and size.

Table 7:
Average diameters and heights of micelle masters and triacrylate resin replicas

	Diameter	Height
Cylindrical master	158±8	13.9±0.5
Cylindrical replica	125±9	23.5±0.8
Spherical master	74±5	20.0±2
Spherical replica	75±4	22±1
Toroidal master	60±4	12.3±0.5
Toroidal replica	57±4	12.7±0.6

Using traditional “top-down” nanopatterning, these structures would be difficult to produce due to their nanometer size and complexity; extensive process and equipment optimization would be required.[96,97] Using “bottom-up” techniques, these shapes can only be formed by certain materials under precise experimental conditions; the polymeric block lengths, interaction parameters, and solvents would have to be carefully chosen to assemble the micelle into the correct morphology as discussed in previous sections. Through

replication, these sophisticated replicate structures are easily and directly derived from the master template and “self-assembled” morphologies can be made using a broad class of materials and in a repeatable, parallel fashion. In **Figure 45** the replicates are formed by polymerizing a triacrylate resin, but other materials could also be used. More complex structures could be formed by using these nano-embossed films as pattern-transfer elements or by incorporating other design elements into the mold.

10. Conclusion

We have systematically measured the dimensions of PS-b-PI micelles as function of length of both soluble and insoluble blocks. By using a combination of AFM, SLS, DLS, SANS, and SAXS we have independently measured the micelle morphology, CMC, aggregation number, hydrodynamic radius, core radius, shell thickness, core density, and cylindrical micelle length. The obtained results were compared with the recently developed theory of Katya Zhulina.[43] The theoretical predictions of the micelle morphology were found to be very accurate for samples with a 40kDa PS block, but the stability ranges of cylindrical and vesicle morphologies were over estimated for the 20kDa PS samples. The opposite case was seen for the CMC, i.e. the theoretical calculations of the CMC were accurate for the 20kDa PS samples, but not the 40kDa ones. The theoretical and experimental results on the aggregation number agreed well for all samples except the 20kDa PS blocks with large PI blocks (most likely a result of the limited concentration range between the CMC and the overlap concentration for these samples). Excellent agreement for all samples was seen between the theoretical hydrodynamic radii and those experimentally measured. Experimental data on the core radius and density are some what inconclusive. While the measured core radii for series 2 agree well with the theoretically predicted ones. In contradiction to theory, the core density for this series was found to change with the size of the soluble block. The core density of series 3 was also found to change with the size of the soluble block, however it had the opposite trend (i.e. the density increased with the soluble

block size instead of decreasing as was seen with series 2). In addition physically unreasonable densities were measured for series 3. A final inconsistency with theory was that the cylindrical micelle length was not seen to change with concentration as predicted by theory. This however is most likely due to poor sample equilibration.

In the above studies, we have demonstrated the micelle equilibration is an important issue. In order to verify if the samples are in equilibrium we have developed a test to monitor the change in aggregation number near the CMC. As was discussed in section 6.1 series 3 and 4 were found to be in equilibrium at temperatures above 25°C, whereas series 2 was found to be out of equilibrium at temperatures below 45°C. In addition, the temperature at which the micelles in series 2 was observed to change systematically with the soluble block size (possibly confirming the observed changes in core density).

The major achievement of this work is that for the first time reversible micelle morphological transitions have been induced solely by temperature changes. This achievement was based on the development of the quantitative phase diagram and precise chemistry. The experimental results on series 1, 2, and 3 guided the development of the theoretical model and allowed for sample in series 4 to be purposefully synthesized near the morphological boundaries. This collaboration between theory, experiment, and synthesis enabled morphological changes with small temperature variations.

In addition, during our studies of the morphological transitions, we found toroidal morphologies that are new morphology for this type of diblock systems. However at this time it is not clear if toroids are an equilibrium morphology or just a morphology only observed during morphological transitions from cylindrical micelles to vesicles.

11. Uncompleted Studies and Proposed Future Work

While the accomplished research has laid the foundation for further studies on polymer micelles, there is still much work to be done.

11.1 Smaller PS Block

While it was shown that the 20kD sample is above the T_g, reversible morphological transitions were found to take place very slowly upon cooling, as such studying PS-b-PI samples with a PS block of 10kD would be very useful. The T_g for the 10kD samples should be even lower than for the 20kD samples and thus morphological transitions at 25°C should not be slowed by being near the T_g. Studying the morphology of a 10kD series will also provide additionally points for the phase diagram and help confirm the location of the phase boundaries as a function of the MW of the PS block.

11.2 Core Density

Preliminary data indicates that the core density of the studied polymer micelles is changing with the soluble block size. While the preliminary indication is that the core density is changing, the results are inconclusive and so further studies are needed. This is an important question, as current theory is unable to account for the core density changes, and as such would need to be modified, if the results are shown to be true.

11.3 Length of Cylindrical Micelles

The length of cylindrical micelles is predicted to scale as the square root of the concentration ($L \sim \sqrt{c}$). All of the experiments done to this point to study this problem, have found the length to be independent of the concentration. However, all the experiments were done with samples having a 40kD PS block. Since it was later found that the 40kD samples are not in equilibrium at 25°C, the measured lengths were probably for frozen micelles. Since the 20kD samples are in equilibrium, studying the lengths of cylindrical micelles formed from 20kD PS blocks should correlate better with the theoretical prediction. The only problem, which might arise, is that the 20kD cylindrical samples were often found to form rings. Since the reason that the length of the cylindrical micelles should scale with concentration is due to the higher energy end caps, the formation of rings could cause significant deviation form theory.

11.4 Morphological Transition Pathways

While studying the change from one morphology to another, several unusually morphologies were observed. As seen in **Figure 46** vesicles are found to break up into smaller rings which eventually separate from one another to form cylindrical micelles. Further studies of the morphological pathway of vesicles to cylindrical micelles may lead to important insights into biological processes

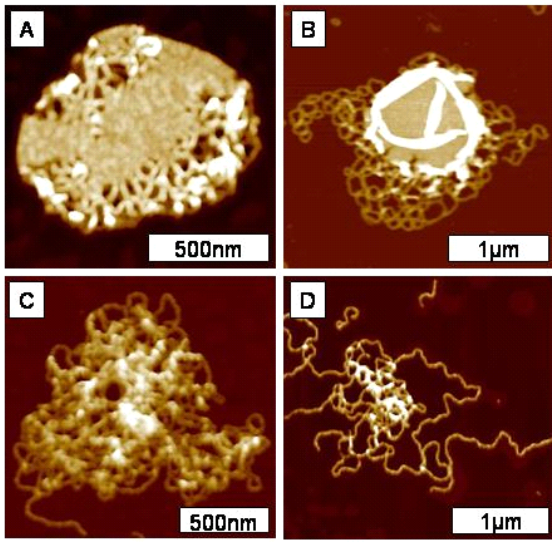

Figure 46. AFM images show vesicles at various stages of the morphological transition to cylindrical micelles. After crossing the phase boundary, the capillary instability leads to perforated vesicles (**A, B**) followed by a network (**C**) and then individual cylindrical micelles (**D**).

involving phospholipid bilayers such as cell division.

11.5 Equilibration on a Surfaces

It was found that if sample 40-10 is heated, after having been adsorbed onto a surface, instabilities develop along its contour. These instabilities cause the cylindrical micelle to break up into spherical droplets **Figure 47.**

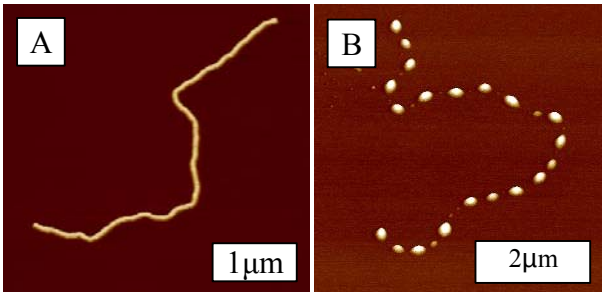

Figure 47. Sample 40-10 after being equilibrated on a mica surface for 2 hours at 60°C was found to break from long cylindrical micelles (**A**) into spherical ones (**B**). Similar to capillary instabilities, small micelles are seen between the larger ones.

11.6 Reverse Micelles

All of the work presented to this point has been done for solvents that are good or θ-solvents for polyisoprene and poor solvents for polystyrene. It is possible to use solvents such as dimethylacetamide which is a good solvent for PS and a poor solvent for PI. In such a way reverse micelles can be formed with a PI core and PS corona. When the aggregation number for samples of the 39kD with very small PI blocks is measured, it is found that the aggregation number increases with the size of the insoluble

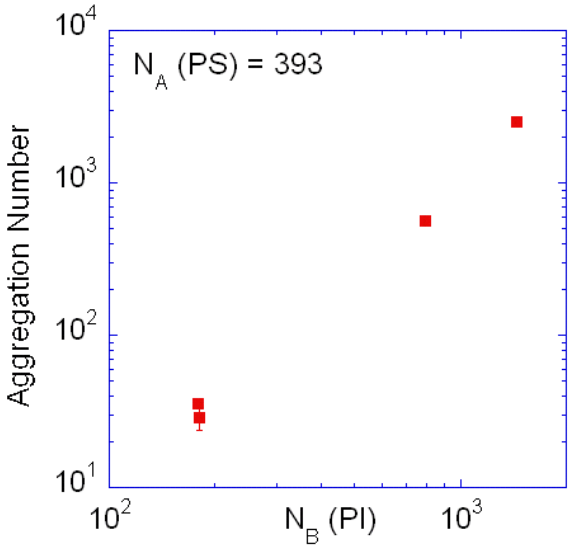

Figure 48. Variation in the aggregation number for the 39kD series in DMA. The plot shows that aggregation number increases from ~30 to ~2500 with the insoluble PI degree of polymerization is raised from ~180 to ~1500 when the soluble PS blocks degree of polymerization is kept constant at 393.

block. As seen in **Figure 48** the aggregation number grows by almost 2 orders of magnitude with the insoluble degree of polymerization is raised by an order of magnitude. Initial AFM attempts to image the micelles formed from sample 39-94 in DMA revealed an unusual structure. As seen in **Figure 49** the micelles appear to have melted on the surface. This makes sense since micelles formed in DMA would have a liquid PI core providing much less structural integrity then those formed with a glassy PS core. Micelles formed with a PI core have the advantage that one does not have to worry about the core freezing and thus equilibration is less of an issue, however as seen in **Figure 49** imaging micelles with a soft core is much more problematic. In order to get visual images of the micelles, a technique such as cryo-TEM will need to be employed.

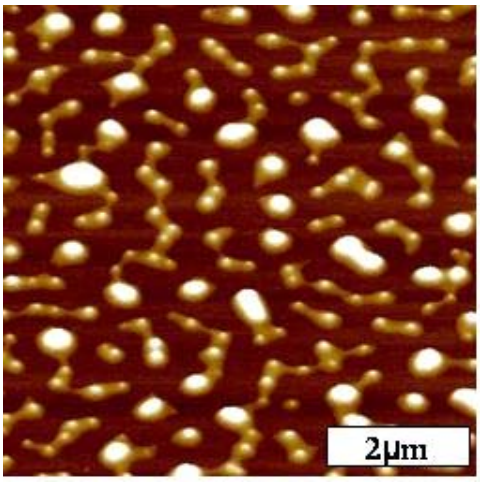

Figure 49. AFM image of sample 39-94 spin cast from a DMA solution.

11.7 Kinetics of Micelle Mixing

In section 6.2 it was shown that unimer exchange takes place during the mixing of different micelle morphologies. However no quantitative data on the kinetics of the mixing process has been obtained. Further studies would allow for the determination of the time scale and energetic cost of extracting diblock from one micelle and inserting it into another.

References

1. Zumdahl, S.S. Chemistry Fourth Edition, Houghton Mifflin: New York, (**1997**).
2. Waugh, D.F. *Milk Protein.* **1971,** *2*, 3.
3. Lodish, H.; Baltimore, D.; Berk, A.; Zipursky, S.L.; Matsudaira, P.; Darnell, J. Molecular Cell Biology Third Edition, Scientific American Books: New York, (**1995)**.
4. Chevalier, Y.; Zemb, T. *Reports on Progress in Physics* **1990**, *53*, 279.
5. Cates, M.E.; Candau, S.J. *J. Phys.: Condens. Matte.* **1990**, *2*, 6869.
6. Texter, J. *Surfactant* **1999**, 1.
7. Tuzar, Z.; Kratochvil, P. *Adv. Colloid Interface Sci*. **1976**, *6*, 201.
8. Hamley, I.W. The Physics of Block Copolymers, Oxford University Press: Oxford, England, (**1998**).
9. Tuzar, Z.; Kratochvil, P. *Surf. Colloid. Sci*. **1993**, *15*, 1.
10. Halperin, A.; Tirrell, M.; Lodge, T.P. *Adv. Polym. Sci*. **1992**, *100*, 31.
11. Choucair, A.; Eisenberg, A. *Eur. Phys. J. E*. **2003**, *10*, 37.
12. Price, C. *Pure. & Appl. Chem.* **1983**, *55*, 1563.
13. Vagberg, L.J.M. ; Cogan, K.A. ; Gast, A.P. *Macromolecules* **1991**, *24*, 1670.
14. Adam, M.; Carton, J.-P. ; Corona-Vallet, S. ; Lairez, D. *J. Phys. II France* **1996**, *6*, 1781.
15. Gao, Z.; Varshney, S.k.; Wong, S.; Eisenberg, A. *Macromolecules*, 27, 7923-7927 (**1994**).
16. Price, C.; Chan, E.K.M.; Hudd, A.L.; Stubbersfield, R.B. *Poly. Comm.* **1986**, *27*, 196.
17. Won, Y.Y.; Davis, H.T.; Bates, F.S. *Science* **1999**, *283*, 960.
18. Discher, D.E.; Eisenberg, A. *Science* **2002**, *297*, 967.
19. Jain, S.; Bates, F.S. *Science* **2003**, *300*, 460.
20. Kesselman, E.; Talmon, Y.; Bang, J.; Abbas, S.; Li, Z.B.; Lodge, T.P. *Macromolecules* **2005**, *38*, 6779.
21. Pochan, D.J.; Chen, Z.; Cui, H.; Hales, K. ; Qi, K. ; Wooley, K.L. *Science* **2004**, *306*, 94.

22. Zhu, J.; Jiang, W. *Macromolecules* **2005**, *38*, 9315.

23. Pispas, S.; Hadjichristidis, N.; Potemkin, I.; Khokhlov, A. *Macromolecules* **2000**, *33*, 1741.

24. Cheng, C.-X.; Huang, Y.; Tang, R.-P.; Chen, E.; Xi, F. *Macromolecules* **2005**, *38*, 3044.

25. Dong, L.H.; Chu, Y.; Yang, F.Y.; Liu, Y.; Liu, J.L. *Chem. Lett*. **2005**, *34*, 1254.

26. Fong, H.; Reneker, D.H. *J. Poly. Sci. Part B: Poly. Phys*. **1999**, *37*, 3488.

27. Zong, X.H.; Kim, K.; Fang, D.F.; Ran, S.F.; Hsiao, B.S.; Chu, B. *Polymer* **2002**, *43*, 4403.

28. Santore, M.M.; Discher, D.E.; Won, Y.Y.; Bates, F.S.; Hammer, D.A. *Langmuir* **2002**, *18*, 7299.

29. Allen, T.M.; Hansen, C.; Martin, F, Redemann C, Yauyoung, A. *Biochim. Biophys. Acta*. **1991**, *1066*, 29.

30. Zhang, L.; Eisenberg, A. *J. Am. Chem. Soc*. **1996**, *118*, 3168.

31. Spatz, J.P.; Moessmer, S.; Moeller, M. *Angew. Chem. Int. Ed. Engl*. **1996**, *35*, 1510.

32. Massey, J.A.; Temple, K.; Cao, L.; Rharbi, Y.; Raez, J.; Winnik, M.A.; Manners, I. *J. Am. Chem. Soc*. **2000**, *122*, 11577.

33. Liu, G.J.; Yan, X.H.; Duncan, S. *Macromolecules* **2002**, *35*, 9788.

34. Liu, G.J.; Yan, X.H.; Duncan, S. *Macromolecules* **2003**, *36*, 2049.

35. Liu, G.J.; Li, Z.; Yan, X.H. *Polymer* **2003**, *44*, 7721.

36. Washburn, N.R.; Lodge, T.P.; Bates, F.S. *J. Phys. Chem. B.* **2000**, *104*, 6987.

37. Qin, A.; Tian, C.; Ramireddy, C.; Webber, S.E.; Munk, P.; Tuzar, Z. *Macromolecules* **1994**, *27*, 120.

38. Price, C. *Pure & Appl. Chem*. **1983**, *55*, 1563.

39. Price, C.; Chan, E.K.M.; Stubbersfield, R.B. *Eur. Polym. J*. **1987**, *23*, 649.

40. Astafieva, I.; Zhong, X.F.; Eisenberg, A. *Macromolecules* **1993**, *26*, 7339.

41. Astafieva, I.; Khougaz, K.; Eisenberg, A. *Macromolecules* **1995**, *28*, 7127.

42. Khougaz, K.; Astafieva, I.; Eisenberg, A. *Macromolecules* **1995**, *28*, 7135.

43. Zhulina, E.B.; Adam, M.; LaRue, I.; Sheiko, S.S. Rubinstein, M. *Macromolecules* **2005**, *38*, 5330.

44. LaRue, I.; Adam, M.; da Silva, M.; Sheiko, S.S.; Rubinstein, M. *Macromolecules* **2004**, *37*, 5002.

45. LaRue, I.; Adam, M.; Pitsikalis, M.; Hadjichristidis, N.; Sheiko, S.S.; Rubinstein, M. *Macromolecules* **2006,** *39*, 309.

46. Zhulina, E.B.; Birshtein, T.M. *Polym. Sci. USSR* **1985**, *27*, 570. Birshtein, T.M.; Zhulina, E.B. *Polymer* **1989**, *30*, 170.

47. Semenov, A.N. *Sov. Phys. JETP* **1985**, *61*, 733.

48. de Gennes, P.G. Scaling Concepts in Polymer Physics, Cornell University Press: Ithaca, NY, (**1979**).

49. Rubinstein, M.; Colby, R.H. Polymer Physics, Oxford University Press: Oxford, UK, (**2003**).

50. Lairez, D.; Adam, M.; Carton, J.P.; Raspaud, E. *Macromolecules* **1997**, *30*, 6798.

51. Alexander, S. *J. Phys*. (Paris) **1977**, *38*, 983.

52. Daoud, M.; Cotton, J.P. *J. Phys*. (Paris) **1982**, *43*, 531.

53. Birshtein, T.M.; Zhulina, E.B. *Polymer* **1984**, *25*, 1453.

54. Wang, Z.-G.; Safran, S.A. *J. Chem. Phys*. **1988**, *89*, 5323.

55. Israelachvili, J.N. Intermolecular and Surface Forces, Academic Press: London, (**1985**).

56. Wang, Z.G. *Macromolecules* **1992**, *25*, 3702.

57. Ajdari, A.; Leibler, L. *Macromolecules* **1991**, *24*, 6803.

58. Ohta, T.; Nonomura, M. *Eur. Phys. J. B* **1998**, *2*, 57.

59. Birshtein, T.M.; Zhulina, E.B. *Macromol. Theory Simul.* **1997**, *6*, 1169.

60. Potemkin, I.I. *Eur. Phys. J. E* **2003**, *12*, 207.

61. Stevens, M.P. Polymer Chemistry an Introduction, Oxford University Press: New York, (**1999**).

62. Hadjichristidis, N.; Iatrou, H.; Pispas, S.; Pitsikalis, M. *J. Polym. Sci. Part A: Polym. Chem*. **2000**, *38*, 3211.

63. Honda, C.; Abe, Y.; Nose, T. *Macromolecules* **1996**, *29*, 6778.

64. Ferry, J.D. Viscoelastic Properties of Polymers, Wiley: New York, (**1980**).

65. Hillmyer, M.A.; Bates, F.S.; Almdal, K.; Mortensen, K.; Ryan, A.J.; Fairclough, J.P.A. *Science* **1996**, *271*, 976.

66. Zhou, Z.; Li, Z.; Ren, Y.; Hillmyer, M.A.; Lodge, T.P. *J. Am. Chem. Soc.* **2003**, *125*, 10182.

67. Winkey, K.I.; Thomas, E.L.; Fetters, L.J. Macromolecules **1992**, *25*, 2645.

68. Wanka, G.; Hoffmann, H.; Ulbricht, W. *Macromolecules* **1994**. *27*, 4145.

69. Li, Z.; Chen, Z.; Cui, H.; Hales, K.; Qi, K.; Wooley, K.L.; Pochan, D.J. *Langmuir* **2005**, *21*, 7533.

70. Zhu, J.; Yu, H.; Jiang, W. *Macromolecules* **2005**, *38*, 7492.

71. Halperin, A. *Macromolecules* **1987**, *20*, 2943.

72. Izzo, D.; Marques, C.M. *Macromolecules* **1993**, *26*, 7189.

73. Gao, Z.; Eisenberg, A. *Macromolecules* **1993**, *26*, 7353.

74. Khougaz, K.; Gao, Z.; Eisenberg, A. *Macromolecules* **1994**, *27*, 6341.

75. Khougaz, K.; Zhong, X. F.; Eisenberg, A. *Macromolecules* **1996**, *29*, 3937.

76. Termonia, Y. *J. of Poly. Sci., Part B: Polymer Physics* **2002**, *40*, 890.

77. Yang, J. *Curr. Opin. Colloid Interface Sci*. **2002**, *7*, 276.

78. Messager, R.; Ott, A.; Chatenay, D.; Urbach, W.; Langevin, D. *Phys. Rev. Let.* **1988**, *60*, 1410.

79. Edenfeld, K.M.; Jarausch, K.F.; Stark, T.J.; Griffis, D.P.; Russel, P.E. *J. Vac. Sci. Technol. B* **1994**, *12*, 3571.

80. Vesenka, J.; Miller, R.; Henderson, E. *Rev. Sci. Instrum.* **1994**, *65*, 2249.

81. Bustamante, C.; Keller, D. *Phys. Today* **1995** *Dec*, 32.

82. Sheiko, S.S. *Adv. Polym. Sci.* **2000**, *151*, 61.

83. Holtzer, A. *J. Polym. Sci.* **1955**, *17*, 432.

84. Lodge, T.P.; Bang, J.; Li, Z.; Hillmyer, M.A.; Talmon, Y. *Royal Soc. Chem., Faraday Dis.* **2005,** *128*, 1.

85. Bang, J.; Jain, S.; Li, Z.; Lodge, T.P.; Pedersen, J.S.; Kesselman, E.; Talmon, Y. *Macromolecules* **2006**, *39*, 1199.

86. Outer, P.; Carr, C.I.; Zimm, B.H. *J. Chem. Phys.* **1950**, *18*, 830.

87. Won, Y.Y.; Brannan, A.K.; Davis, H.T.; Bates, F.S. *J. Phys. Chem. B* **2002**, *106*, 3354.

88. Nakano, M.; Matsuoka, H.; Yamaoka, H.; Poppe, A.; Richter, D. *Macromolecules* **1999**, *32*, 697.

89. Ouarti, N.; Viville, P.; Lazzaroni, R.; Minatti, E.; Schappacher, M.; Deffieux, A.; Borsali, R. *Langmuir* **2005,** *21*, 1180.

90. Zhang, L.; Eisenberg, A. *Macromolecules* **1999**, *32*, 2239.

91. Ding, J. ; Liu, G. ; Yang, M. *Polymer* **1997**, *38*, 5497.

92. Hu, Z. ; Jonas, A.M. ; Varshney, S.K. ; Gohy, J.F. J. *Am. Chem. Soc*. **2005**, *127*, 6526.

93. Provencher, S.W. *Makromol. Chem*. **1979**, *180*, 201.

94. May, S.; Ben-Shaul, A. *J. Phys. Chem. B*. **2001**, *105*, 630.

95. Aizenberg, J.; Weaver, J.C.; Thanawala, M.S.; Sundar, V.C.; Morse D.E.; Fratzl P. *Science* **2005**, *309*, 275.

96. Brands, M., Carl, A.; Dumpich, G. *Superlattices and Microstructures* **2005**, *37*, 388.

97. Landis, S.; Pauliac, S.; Hanawa, R.; Suetsugu, M.; Akita, M. *Microelectronic Engineering* **2004**, *73-74*, 271.

98. Tang, Q.; Shi, S.Q.; Zhou, L.M. *Journal of Nanoscience and Nanotechnology* **2004**, *4*, 948.

99. Kramer, S.; Fuierer, R.R.; Gorman, C.B. *Chem. Revs.* **2003**, *103*, 4367.

100. Avouris, P. *Accounts of Chemical Research* **1995**, *28*, 95.

101. Jackman, R.J.; Brittain, S.T.; Adams, A.; Wu, H.; Prentiss, M.G.; Whitesides, S.; Whitesides, G.M. *Langmuir* **1999**, *15*, 826.

102. Henzie, J.; Kwak, E.S.; Odom, T.W. *Nano Letters* **2005**, *5*, 1199.

103. Xu, Q.B.; Tonks, I.; Fuerstman, M.J.; Love, J.C.; Whitesides, G.M. *Nano Letters* **2004**, *4*, 2509.

104. Rolland, J.P.; Hagberg, E.C.; Denison, G.M.; Carter, K.R.; DeSimone, J.M. *Angewandte Chemie-International Edition* **2004**, *43*, 5796.

105. Rolland, J.P.; Maynor, B.W.; Euliss, L.E.; Exner, A.E.; Denison, G.M.; DeSimone, J.M. *Journal of the American Chemical Society* **2005**, *127*, 10096.

106. Rolland, J.P.; Van Dam, R.M.; Schorzman, D.A.; Quake, S.R.; DeSimone, J.M. *Journal of the American Chemical Society* **2004**, *126*, 2322.